Operational Aspect of Missions to the Triangular Sun-Earth Libration Points

Auteur : Boudart, Vincent
Promoteur(s) : Rauw, Gregor; 7889
Faculté : Faculté des Sciences
Diplôme : Master en sciences spatiales, à finalité approfondie
Année académique : 2018-2019
URI/URL : http://hdl.handle.net/2268.2/6982

Operational Aspect of Missions to the Triangular Sun-Earth Libration Points

by

Vincent Boudart

Bachelor in Engineering, University of Liege, 2017

Thesis Submitted in Partial Fulfillment of the
Requirements for the Degree of
Master in Space Sciences

Research Focus

in the
Department of Astrophysics, Geophysics and Oceanography
Faculty of Sciences

UNIVERSITY OF LIEGE
Summer 2019

"We are stardust brought to life, then empowered by the universe to figure itself out - and we have only just begun."

— Neil deGrasse Tyson, Astrophysics for People in a Hurry

Acknowledgement

First of all, I would like to thank my parents for giving me the opportunity of studying for the last 5 years. I also acknowledge my family for their unconditional support and for the enthusiasm they showed in following my curriculum. I would like to express my whole gratitude to Prof. Gregor Rauw for his advised comments and reviews when reading the present work. He also greatly contribute to establish some mathematical developments in Chapter 2 and to interpret diverse results throughout my whole thesis. Special thanks are addressed to Prof. Yael Nazé without whom I would certainly not have obtained a trainee position at the European Space Agency. I am very grateful to Dr. Florian Renk, my ESA advisor, who introduced me to the concept of non-linear optimization and influenced the implementation made in Chapter 4. I would like to show gratitude to Amedeo Rocchi, mission analyst contractor at ESOC, and Francesca Laetizia, space debris engineer, for the fruitful discussions that led me to the results of Chapter 5. Great thanks are given to Max Rödelsperger, mission analyst at ESOC, and Lorenzo Bucci, phD candidate from the Politecnico di Milano, for both their help with the MASW software and their constructive comments on the results obtained. I would like to acknowledge my bachelor partners and friends Arnaud Delcourt, Corentin Deserranno and Nicolas Leclercq that contribute to the achievement of my studies. I am finally indebted to Benjamin Finociety, a friend met two years ago, with whom I shared my strong interest in Space Sciences.

Contents

1 Introduction **14**

2 Preliminary computations **17**

2.1 Evaluating the Newtonian force at L5 . . . 17

2.2 Long-term impact of other planets . . . 19

2.3 Search for new stable points . . . 23

3 Early trajectory implementation **26**

3.1 Libration trajectory . . . 26

3.1.1 Libration in the circular Sun-Earth system . . . 26

3.1.2 Propagation in the circular Sun-Earth system . . . 30

3.1.3 Propagation in the Solar system . . . 34

3.2 Trojan-like trajectory . . . 39

3.2.1 Modelling of asteroid orbits . . . 39

3.2.2 Use as disposal orbits . . . 41

4 Operational orbit determination **46**

4.1 Propagation with MASW . . . 46

4.2 Closed orbit optimization . . . 54

4.2.1 Theoretical background . . . 54

4.2.2 First implementation and algorithm selection . . . 55

4.2.3 Long-term behaviour . . . 65

4.2.4 Largest achievable orbit . . . 67

5 Space debris distribution in case of a fragmentation event **68**

5.1 The SNAPPshot software and its breakup model . . . 69

5.2 Software settings and explosion scenarios . . . 70

5.3 Debris dispersion study . . . 71

5.3.1 Break-up at L4 or L5 . . . 71

5.3.2 Break-up on the operational orbit . . . 82

6 Disposal orbit opportunities **87**
6.1 Applying a delta-V manoeuvre 87
6.1.1 Verification of earlier results 87
6.1.2 Characterization of tadpole and horseshoe orbits 90
6.1.3 Interference with future missions 91
6.2 Using the solar radiation pressure 93

7 Conclusion **95**

List of Figures

1.1 Lagrangian points location for the Sun-Earth system as seen from the solar North pole. Note that the Sun rotates anticlockwise. 15

2.1 Comparison of the norm of the gradient of the potential in the plane of the ecliptic in the case of the pure Roche potential (left) and the modified potential (right). Contours of equal values of log $|\vec{\nabla}\Phi'|$ are shown for values of -3.0 (indigo), -2.0 (dark blue), -1.0 (light blue), 0.0 (cyan), 1.0 (light green), 2.0 (orange) and 3.0 (yellow). The top, middle and lower panels correspond to the whole orbital plane, the neighbourhood of the L1 and L2 points, and the vicinity of L5, respectively. 23

2.2 Norm of the gradient of the potential in the plane of the ecliptic in the vicinity of L5 (left) and a zoomed view of that gradient (right). Contours of equal values of log $|\vec{\nabla}\Phi'|$ are shown for values of -6.0 (dark blue), -5.0 (light blue), -4.0 (cyan), -3.0 (green), -2.0 (khaki colour), -1.0 (orange) and 0 (yellow). 24

2.3 Determinant of the Hessian matrix (left) and second derivative $\frac{\partial^2 \Phi'}{\partial x^2}$ (right) in the plane of the ecliptic in the vicinity of L5. Contours of equal values are shown with steps of 0.5 (left) and 0.25 (right). 25

3.1 Co-rotating frame attached to L5 (magenta) and inertial frame centred on the Sun (red). The inertial X axis initially points towards the Earth. 27

3.2 Representations of the long-period (left) and short-period (right) libration trajectories in the entire Solar system (top) and in the vicinity of L5 (bottom). The amplitude along the X' axis has been set to 0.1 AU for the sake of clarity. 29

3.3 Representations of the long-period (left) and short-period (right) libration trajectories in the heliocentric frame. Orbits are drawn for a mission duration of 20 years and with an X' axis amplitude set to 0.1 AU. 30

3.4 Representation of the precession experienced for short-period libration trajectories. A timescale of 10000 years has been considered to highlight the effect. The amplitude along the X' axis has been set to 0.1 AU for the sake of clarity. 30

3.5 Effect of the amplitude of short-period libration orbits on a 20-year propagation in the Sun-Earth system. The initial amplitude (in km) is 10^7 (top left), $5\,10^6$ (top right), 10^6 (bottom left) and $5\,10^5$ (bottom right) respectively. The initial phase is zero for all cases. The magenta line denotes the expected short-period trajectory. The dark blue vector shows the initial velocity direction. 33
3.6 Drifting effect of the short-period libration orbits on a 111-year (left) and 222-year (right) propagation in the Sun-Earth system. The initial amplitude is $5\,10^5$ km and the phase is zero. The magenta line denotes the expected short-period trajectory. The dark blue vector shows the initial velocity direction. 33
3.7 Effect of the phase component of short-period libration orbits on a 20-year propagation in the Sun-Earth system. The initial phase is 0° (top left), 90° (top right), 180° (bottom left) and 270° (bottom right) respectively. The amplitude is set to $5\,10^5$ km for all cases. The magenta line denotes the expected short-period trajectory. The dark blue vector shows the initial velocity direction. 34
3.8 Short-period libration orbit propagation in the Sun-Earth system (left) and in the Solar system (right) taking into account the perturbations from Venus, Mars, Jupiter and Saturn. The propagation starts on 22 January 2030 at 12:00 and ends on 22 January 2050 at 12:00. The initial phase is 0° (top) or 90° (bottom) and the amplitude is set to $5\,10^5$ km for both cases. The magenta line denotes the expected short-period trajectory. The dark blue vector shows the initial velocity direction. 36
3.9 Short-period libration orbit propagation in the Solar system taking into account the perturbations from Venus (blue), Mars (red), Jupiter (magenta) and Saturn (green). The propagation time has been set to 20 years and starts on 22 January 2029 (top), 27 April 2029 (second row), 26 July 2029 (third row) and 24 October 2029 (bottom). The corresponding planet positions are shown to the right of each trajectory for the first 100 days of propagation. The initial phase is 65.64° and the amplitude is set to $5\,10^5$ km for all cases. The magenta line denotes the expected short-period trajectory. The dark blue vector shows the initial velocity direction. 37
3.10 Planetary configuration in the Earth's rotating frame for 28 November 2028 (left), 2 May 2028 (middle) and 26 June 2029 (right). The planet positions are shown for the first 100 days of propagation. 38
3.11 2D Tadpole and horseshoe orbits in the Earth's rotating frame. The propagation starts on 22 January 2020 in the vicinity of L5 and ends on 22 January 2420. The initial orbital phase has been set to 0°. The amplitude of the initial orbit is $5\,10^6$ (top left), $6\,10^6$ (top middle), $7\,10^6$ (top right), $8\,10^6$ (bottom left) and $9\,10^6$ (bottom right) km. 40

3.12 Close view of a tadpole orbit (cyan) in the Earth's rotating frame. The propagation starts on 22 January 2020 in the vicinity of L5 and ends on 22 January 2420. The initial orbital phase has been set to 0° and the amplitude is $5\,10^6$ km. The black line is the simulated circular orbit of the Earth around the Sun. 40
3.13 Example of tadpole orbit around the L5 point for a three-body system with a mass ratio of 0.1. **(Left)** The dynamics around that point is driven by two components: a long-period motion (elongated ellipse) about the equilibrium point combined with a short-period motion (small ellipse). **(Right)** The resulting global path about L5. Adapted from *Marzari et al. (2002)* and *Murray and Dermott (1999)*. 41
3.14 Trajectories obtained after a delta-V kick of 100 (top left), 133 (top right), 166 (bottom left) and 200 (bottom right) meters per second. The initial amplitude of the orbit is 10^6 km and the manoeuvre takes place at 90° orbital phase. The propagation starts on 22 January 2020 and ends on 22 January 2270. 45

4.1 New co-rotating frame attached to L5 (magenta) and Earth's rotating frame (red). The black line represents a circle of 1 AU radius centered on the Sun. . . 48
4.2 Obtained trajectories (magenta) after a propagation with the ESA MASW software. The orbit is shown in the Earth's rotating frame centered either on the Sun (top) or on L5 (bottom). The Sun centered representation is presented both in the global Solar system (top left) and around L5 (top right) and projected in the ecliptic plane. The L5 centered orbits are shown in the ecliptic plane (bottom left) and a x-z view is also proposed (bottom right). The initial amplitude of the orbit is 10^6 km and the orbital phase is set to 90°. The propagation starts on 22 January 2020 and ends on 22 January 2040. The blue (black) dot and the blue (black) path in the upper left panel represent respectively the Earth (L5) initial position and whole path. The red and blue dots near L5 show the final and initial position of the spacecraft. 49
4.3 Comparison of the trajectories (magenta) acquired with (left) and without (right) solar radiation pressure. The orbit is shown in the Earth's rotating frame centered on L5 and projected in the ecliptic plane. The initial amplitude of the orbit is 10^6 km and the orbital phase is set to 90°. The propagation starts on 22 January 2020 and ends on 22 January 2040. The black dot represents L5 while the blue and red dots stand for the initial and final positions of the spacecraft. 50

4.4 Comparison of the trajectories (magenta) obtained with an initial orbital phase of 0° (top left), 90° (top right), 180° (bottom left) and 270° (bottom right). Solar radiation pressure is taken into account with $C_r = 1.5$. The orbit is shown in the Earth's rotating frame centered on L5 and projected onto the ecliptic plane. The initial amplitude of the orbit is 10^6 km. The propagation starts on 22 January 2020 and ends on 22 January 2040. The black dot represents L5 while the blue and red dots stand for the initial and final positions of the spacecraft. 51
4.5 Comparison of the trajectories (magenta) collected for four different starting dates through the year 2020. The propagation is initiated on 22 January (top left), 22 April (top right), 22 July (bottom left) and 22 October (bottom right) and ends on 22 January 2040. Solar radiation pressure is taken into account with $C_r = 1.5$. The orbit is shown in the Earth's rotating frame centered on L5 and projected onto the ecliptic plane. The initial amplitude of the orbit is 10^6 km and the orbital phase is set to 90°. The black dot represents L5 while the blue and red dots stand for the initial and final positions of the spacecraft. 52
4.6 Trajectory of the spacecraft (magenta) over a 20 year propagation starting on 31 March 2020 and ending on 22 January 2040. Solar radiation pressure is taken into account with $C_r = 1.5$. The orbit is shown in the Earth's rotating frame centered on L5 and projected in the ecliptic plane. The initial amplitude of the orbit is 10^6 km and the orbital phase is set to 90°. The black dot represents L5 while the blue and red dots stand for the initial and final positions of the spacecraft. 53
4.7 Definition of the Sun-Spacecraft-Earth (SSE) and Earth-Sun-Spacecraft (ESS) angles. 56
4.8 Comparison of the trajectories (magenta) optimized with different algorithms in the Earth's rotating frame and centered on L5. The COBYLA (top left), MMA (top right), Compass search (bottom left) and CCSA (bottom right) are used. Solar radiation pressure is taken into account with $C_r = 1.0$. The amplitude of the orbit is 10^6 km and the initial orbital phase is 90°. The propagation starts on 21 June 2024 and ends on 21 June 2034. The black dot represents L5 while the blue and green dots stand for the initial and final positions of the spacecraft. 59
4.9 Results obtained via the optimization of a 10^6 km amplitude orbit with the COBYLA algorithm. The trajectory is shown in the Earth's rotating frame and centered on L5. Both x-y (top left) and x-z (top right) views are proposed. The evolution of the SSE (bottom left) and ESS (bottom right) angles is also drawn together with their corresponding constraints (red lines) and mean (black line). Solar radiation pressure is taken into account with $C_r = 1.0$. The propagation starts on 21 June 2024 and ends on 21 June 2034. The black dot represents L5 while the blue and green dots stand for the initial and final positions of the spacecraft. 62

4.10 Results obtained via the optimization of a 10^6 km amplitude orbit with the COBYLA algorithm. The orbit is inclined by 150° with respect to the ecliptic plane. The trajectory is shown in the Earth's rotating frame and centered on L5. Both x-y (top left) and x-z (top right) views are proposed. The evolution of the SSE (bottom left) and ESS (bottom right) angles is also drawn together with their corresponding constraints (red lines) and mean (black line). Solar radiation pressure is taken into account with $C_r = 1.0$. The propagation starts on 21 June 2024 and ends on 21 June 2034. The black dot represents L5 while the blue and green dots stand for the initial and final positions of the spacecraft. 63
4.11 Comparison of two orbits obtained via the optimization of a 10^6 km amplitude orbit with the COBYLA algorithm starting at a 0° (left) and 90° (right) orbital phase. The trajectory is shown in the Earth's rotating frame and centered on L5. Solar radiation pressure is taken into account with $C_r = 1.0$. The propagation starts on 21 June 2024 and ends on 21 June 2034. The black dot represents L5 while the blue and green dots stand for the initial and final positions of the spacecraft. 64
4.12 Comparison of two orbits obtained via the optimization with the COBYLA algorithm starting at a zero orbital phase. The amplitude is either 10^6 (left) or 10^5 (right) km. The trajectory is shown in the Earth's rotating frame and centered on L5. Solar radiation pressure is taken into account with $C_r = 1.0$. The propagation starts on 21 June 2024 and ends on 21 June 2034. The black dot represents L5 while the blue and green dots stand for the initial and final positions of the spacecraft. 64
4.13 50 year (left) and 222 year (right) propagation of a 10^5 km amplitude orbit obtained via the optimization with the COBYLA algorithm starting at a zero orbital phase. The trajectory is shown in the Earth's rotating frame and centered on L5. Solar radiation pressure is taken into account with $C_r = 1.0$. The propagation starts on 21 June 2024. The black dot represents L5 while the blue and green dots stand for the initial and final positions of the spacecraft. 65
4.14 50 year (left) and 222 year (right) propagation of a 10^6 km amplitude orbit obtained via the optimization with the COBYLA algorithm starting at a zero orbital phase. The trajectory is shown in the Earth's rotating frame and centered on L5. Solar radiation pressure is taken into account with $C_r = 1.0$. The propagation starts on 21 June 2024. The black dot represents L5 while the blue and green dots stand for the initial and final positions of the spacecraft. 66

4.15 50 year propagation of a $4\,10^5$ (left) and a $6\,10^5$ (right) km amplitude orbit obtained via the optimization with the COBYLA algorithm. The spacecraft starts at a zero orbital phase. The trajectory is shown in the Earth's rotating frame and centered on L5. Solar radiation pressure is taken into account with $C_r = 1.0$. The propagation starts on 21 June 2024 and ends on 21 June 2074. The black dot represents L5 while the blue and green dots stand for the initial and final positions of the spacecraft. 66
4.16 10 year (left) and 222 year (right) propagation of a $1.6\,10^6$ km amplitude orbit obtained via the optimization with the COBYLA algorithm starting at a zero orbital phase. The trajectory is shown in the Earth's rotating frame and centered on L5. Solar radiation pressure is taken into account with $C_r = 1.0$. The propagation starts on 21 June 2024. The black dot represents L5 while the blue and green dots stand for the initial and final positions of the spacecraft. 67

5.1 Debris distribution after a spacecraft explosion occurring exactly at L5. The debris positions (cyan) are shown in the Earth's rotating frame. The maximum velocity increment after the explosion has been set to 10 m/s. The yellow, blue and red dots respectively stand for the initial position of the Sun, the Earth and L5. 72
5.2 Debris distribution after a spacecraft explosion occurring exactly at L5. The debris positions (cyan) are shown in the Earth's rotating frame. The maximum velocity increment after the explosion has been set to 100 m/s. The yellow, blue and red dots respectively stand for the initial position of the Sun, the Earth and L5. 73
5.3 Debris distribution after a spacecraft explosion occurring exactly at L5. The debris positions (cyan) are shown in the Earth's rotating frame. The maximum velocity increment after the explosion has been set to 1000 m/s. The yellow, blue and red dots respectively stand for the initial position of the Sun, the Earth and L5. 74
5.4 Debris distribution after a spacecraft explosion occurring exactly at L4. The debris positions (cyan) are shown in the Earth's rotating frame. The maximum velocity increment after the explosion has been set to 10 m/s. The yellow, blue and red dots respectively stand for the initial position of the Sun, the Earth and L5. 75
5.5 Debris distribution 50 years after a spacecraft explosion occurring exactly at L5. The explosion either takes place 90 (top left), 180 (top right), 270 (bottom left) or 360 (bottom right) days after the 1st January 1900. The debris positions (cyan) are shown in the Earth's rotating frame. The maximum velocity increment after the explosion has been set to 10 m/s. The yellow, blue and red dots respectively stand for the initial position of the Sun, the Earth and L5. 76

5.6 Debris distribution after a spacecraft explosion occurring exactly at L5. Note that the propagation does not take the SRP into account. The debris positions (cyan) are shown in the Earth's rotating frame. The maximum velocity increment after the explosion has been set to 10 m/s. The yellow, blue and red dots respectively stand for the initial position of the Sun, the Earth and L5. 77
5.7 Debris spatial extent as a function of the A/M ratio (in m^2/kg). The debris positions are shown in the Earth's rotating frame. The maximum velocity increment after the explosion has been set to 10 m/s. The yellow, blue and red dots respectively stand for the initial position of the Sun, the Earth and L5. . . 78
5.8 Debris spatial extent as a function of the delta-V boost (in m/s) received after the explosion. The debris positions are shown in the Earth's rotating frame. The maximum velocity increment after the explosion has been set to 1000 m/s. The yellow, blue and red dots respectively stand for the initial position of the Sun, the Earth and L5. 79
5.9 Maximum orbital phase as a function of the A/M ratio (left) and the delta-V boost obtained after the explosion (right) for different explosion magnitudes. The maximum velocity increment after the explosion has been set to 10 (top), 30 (second row), 70 (third row) and 200 (bottom) m/s. 80
5.10 Slope of the linear fit as a function of the SRP coefficient for an explosion with a maximum ejection velocity of 10 m/s. 81
5.11 Debris distribution 50 years after a spacecraft explosion occurring exactly on a 10^6 km amplitude orbit. The explosion takes place either at a 0° (top left), 90° (top right), 180° (bottom left) or 270° (bottom right) orbital phase. The debris positions (cyan) are shown in the Earth's rotating frame. The maximum velocity increment after the explosion has been set to 10 m/s. The yellow, blue and red dots respectively stand for the initial position of the Sun, the Earth and L5. . . 84
5.12 Debris distribution 50 years after a spacecraft explosion occurring exactly on a 10^6 km amplitude orbit. The explosion takes place either at a 0° (top left), 90° (top right), 180° (bottom left) or 270° (bottom right) orbital phase. The debris positions (cyan) are shown in the Earth's rotating frame. The maximum velocity increment after the explosion has been set to 100 m/s. The yellow, blue and red dots respectively stand for the initial position of the Sun, the Earth and L5. . . 85
5.13 Debris distribution 50 years after a spacecraft explosion occurring exactly on a 10^6 km amplitude orbit. The explosion takes place either at a 0° (top left), 90° (top right), 180° (bottom left) or 270° (bottom right) orbital phase. The debris positions (cyan) are shown in the Earth's rotating frame. The maximum velocity increment after the explosion has been set to 1000 m/s. The yellow, blue and red dots respectively stand for the initial position of the Sun, the Earth and L5. . . 86

6.1 Disposal orbits acquired after a 42 m/s (left) or a 43 m/s (right) delta-V boost taking place at a 270° orbital phase. The propagation starts on 21 March 2035 and ends on 21 June 3034. The trajectories are shown in the Earth's rotating frame centred on the Sun. The yellow, blue and red dots respectively stand for the position of the Sun, the Earth and L5 at the epoch the manoeuvre is applied. 89
6.2 Disposal orbits acquired after a 154 m/s (left) or a 155 m/s (right) delta-V boost taking place at a 270° orbital phase. The propagation starts on 21 March 2035 and ends on 21 June 3034. The trajectories are shown in the Earth's rotating frame centred on the Sun. The yellow, blue and red dots respectively stand for the position of the Sun, the Earth and L5 at the epoch the manoeuvre is applied. 89
6.3 Extreme positive and negative angular extents of tadpole orbits (measured from L5) as a function of the delta-V magnitude needed to reach them. 90
6.4 Extreme positive and negative angular extents of horseshoe orbits (measured from L5) as a function of the delta-V magnitude needed to reach them. The horizontal magenta line shows the angular position of L3 as seen from L5. 91
6.5 Total angular extent of tadpole (left) and horseshoe (right) orbits as a function of the delta-V magnitude needed to reach them. 92
6.6 Fraction of the time spent in the operational region around L5 for different tadpole (left) and horseshoe (right) orbits. The propagation time has been set to 5000 years. 93
6.7 Extreme positive and negative angular extents of horseshoe orbits (measured from L5) as a function of the area-to-mass ratio. 93

List of Tables

2.1 Maximum and minimum gravitational force produced at the location of the triangular Sun-Earth libration points for the eight planets of the Solar System. The amplitude is defined as the ratio between maximum and minimum force. . . 18

2.2 Mass, semi-major axis and mass ratio of the eight planets of the Solar system. In the last column, m_0 stands for the mass of the Sun. 18

2.3 Coordinates of the 5 Lagrangian points of the Sun-Earth system. $q_3 = 3.0045\,10^{-6}$ is the mass ratio of the Earth. Expressions for the collinear points are correct up to the order $\frac{1}{3}$ in q_3 for L1 and L2 and to order 1 for L3. Values taken from [8]. . 21

3.1 Critical amplitude of the short-period orbit for 10 different planetary configurations. The initial phase has been set to 65.64°. 38

3.2 Angular distance for both operational orbits of $5\,10^5$ and 10^6 km amplitude in the case of a tangential delta-V manoeuvre of either 5, 10, 20, 30, 40 or 50 m/s. The delta-V kick takes place either at 0, 30, 60 or 90 degree orbital phase. The propagation starts on 22 January 2020 and ends on 22 January 2270. 42

3.3 Disposal delta-V cost for some typical satellite missions. 43

4.1 Comparison of the 4 algorithms used to optimize a closed trajectory around L5. 58

5.1 Slope and intercept coefficients obtained through a linear fit of the scatter plot showing the debris maximum orbital phase as a function of their A/M ratio. Note that the SRP coefficient has been set to 1.5. 74

5.2 Slope and intercept coefficients obtained through a linear fit of the scatter plot showing the debris maximum orbital phase as a function of their A/M ratio. The SRP coefficient is either set to 0.5, 1.0 or 2.0. 81

5.3 Comparison of the positive angular extent of the debris cloud for on-orbit and L5 breakups with a maximum velocity increment of 10 m/s. The explosion occurs either at a 0°, 90°, 180° or 270° or at the corresponding dates for L5. 83

6.1 Maximum L5-Sun-Spacecraft angle encountered over one full disposal orbit oscillation around L5. The magnitude of the delta-V manoeuvre has been set to 20 m/s. 88

Chapter 1

Introduction

Gravitation, originally stated by Sir Isaac Newton, is the force that brings any massive objects towards one another. His famous inverse-square law was considered to be the state of the art in celestial mechanics and remained unaltered for more than two centuries. Although it has been superseded by Einstein's theory of general relativity in the beginning of the twentieth century, most modern applications still use Newton's theory as it gives sufficiently accurate results for situations involving sufficiently small masses, speeds and energies. This is particularly the case for most satellites orbiting the Earth or travelling in the Solar System.

The interaction of two point-like bodies through gravitation, known as the two-body problem, is the starting point in the study of satellite dynamics. The problem is well-known and has extensively been described for about three hundred years. The result is a planar conical-type orbit for both masses, i.e. either a circle, an ellipse, a parabola or a hyperbola, depending on the eccentricity of the orbit. The motion of each body is perfectly predictable and coherent. However, when a third body is added, the system may undergo chaotic motions, as established first by Poincaré in the late nineteenth century (*Poincaré H., 1890*), and there is no closed-form solution for all sets of initial conditions. Under some hypotheses yet, Euler and Lagrange found particular solutions for the three-body problem, that was then called the circular restricted three-body problem. Assuming one body with a negligible mass with respect to the other two, the latter moving in circular orbits around their common center of mass, Lagrange was able to demonstrate that, in the rotating frame attached to the two massive bodies, there exist 5 points where the third one experiences zero net gravitational force (*Lagrange J. L., 1772*). These points were called Lagrangian points or libration points. Three of them, namely L1, L2 and L3, are located along the line joining the center of masses of the two dominant bodies and were then called collinear points. Each of the last two points, called L4 and L5, makes an equilateral triangle with the centres of the two main bodies and these points were hence called triangular points.

The L4 and L5 points are linearly stable[1] in opposition to the collinear points and are therefore the ideal locations to trap smaller bodies like asteroids or dust particles. The best-known example is the group of Trojan asteroids that are found to be in orbit around the triangular points of the Sun-Jupiter system. An asteroid, named 2010 TK7, has also been detected around the L4 point of the Sun-Earth system (*Connors et al., 2011*). It is the first and unique Earth Trojan asteroid discovered up to now. A further example is materialised by the dust clouds located at the L5 point of the Earth-Moon system. These clouds were first observed in 1961 by the Polish astronomer Kazimierz Kordylewski and recently confirmed by an Hungarian team in October 2018 (*Slíz-Balogh et al., 2018*).

Figure 1.1 shows the layout of the Lagrangian points for the Sun-Earth system. As it can be seen L4 and L5 settle on the approximated circular orbit of the Earth around the Sun, while L1 and L2 lie 1.5 million kilometres away on either side of the Earth.

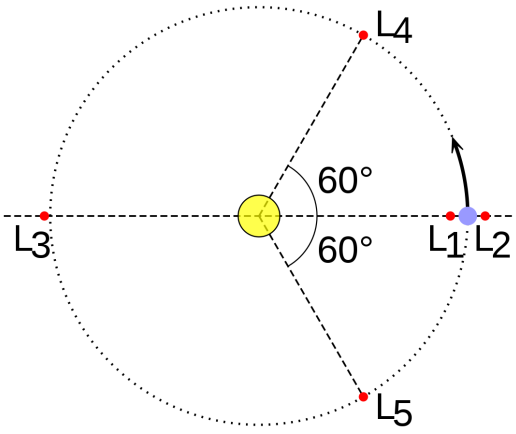

Figure 1.1: Lagrangian points location for the Sun-Earth system as seen from the solar North pole. Note that the Sun rotates anticlockwise.

As the system rotates with the Earth, L1 is permanently looking at the Sun while L2 is partially shadowed from the latter by the Earth. L1 therefore constitutes ideal satellite location for space-weather missions as it provides a continuous view of the Sun without interferences from the Earth and the Moon. The SoHO mission (Solar and Heliospheric Observatory) is an example of a satellite currently orbiting L1. On the other hand, L2 is well suited for deep-space observation because of its stable thermal and gravitational environment. The Planck, Gaia and Herschel satellites were launched towards that point, as will be the James Webb Space Telescope in the coming years.

Interestingly, no satellite has yet been launched around L3, L4 and L5. However, L3 would allow monitoring the evolution of sunspots before they rotate towards the Earth, providing an

[1] Under a certain condition that will be discussed later.

early alert. This is of particular interest to predict space weather forecast in the medium term and take relevant measures to protect orbiting satellites as well as Earth-based installations[2]. In the same way, a satellite located in L5 would observe the side of the Sun which will face the Earth within several days and give a good pre-warning time in case of significant solar events. On the other hand, placing a satellite in L4 would not contribute to space weather monitoring but rather to study the evolution of sunspots together with the rotation of the Sun.

In the framework of the Space Situational Awareness (SSA) Program, the European Space Agency (ESA) is currently developing a space weather mission whose purpose is to place a satellite in orbit around L5. The mission is currently called Lagrange and will be dedicated to the observation of our Sun (*ESA website, Lagrange mission*). Located 60° behind the Earth, the spacecraft will deliver an early warning of possibly harmful space weather resulting for example from coronal mass ejection (CME) events. Predicting space weather is of primary importance regarding the numerous applications that rely on it. If a CME reaches the Earth, it will probably affect and perturb satellites in orbit (and thus GPS navigation), data and communication networks, terrestrial power grids as well as being a huge threat for astronaut health.

The primary objective of the current thesis is to study different options of orbit that would also be useful for other missions or scientific purposes. In Chapter 2, analytical developments are derived in order to assess the effect of the Solar system planets on the stability of L5. Chapter 3 will then give a brief overview of the dynamics at the triangular Lagrangian points and the two big families of achievable orbits near that points will be examined. Operational trajectories for L5 missions are then derived rigorously in Chapter 4 and limitations on their amplitude are also discussed. Particularly, the long-term behavior of such orbits will be addressed and the inherent station-keeping requirements will be derived, if needed. Chapter 5 will investigate the distribution of debris in the Earth's rotating frame in case of a fragmentation event occurring either exactly at L5 or on the operational orbit. In the context of space debris mitigation, long-term graveyard orbits about L5 will finally be discussed in Chapter 6.

[2]Transmitting data collected by a spacecraft around L3 would eventually require a relai satellite (e.g. in L4 or L5) as the L3 point is constantly hidden by the Sun as seen from Earth.

Chapter 2

Preliminary computations

This chapter is devoted to the analysis of the effects of other Solar System planets on the gravitational potential experienced in the vicinity of the L5 triangular point. A first crude computation of the Newtonian potential exerted by each planet at L5 is accomplished to discriminate irrelevant planets for the following of the study. Then, for the remaining planets, the Gauss model is used to assess their long-term impact on the elementary Roche potential. This will lead to a modified potential accounting for the perturbations coming from pre-selected planets. Finally, a search for stable points, distinct from L5, is carried out for the modified potential.

The MATLAB software (2018a version) has been used to carry out the computations in the present chapter.

2.1 Evaluating the Newtonian force at L5

To evaluate which planets of the Solar system will have a perturbing effect on the trajectory of a satellite orbiting about L5, we compute the classical Newtonian force of each planet at the two extreme points of their orbit corresponding to the minimum and maximum distance to L5. At this stage, all the planets are considered to be in circular orbit around the Sun with a radius equal to their semi-major axis. As a reminder, the Newtonian force per unit mass (in N/kg) exerted by a body of mass M at the distance r from that body is given by:

$$|F| = \frac{GM}{r^2} \tag{2.1}$$

where $G = 6.67408\,10^{-11}\ m^3 kg^{-1} s^{-2}$ is the gravitational constant.

Table 2.1 summarizes the results obtained. All the data such as the mass and the semi-major axes of the planetary orbits, the astronomical unit (AU) and the gravitational constant are taken from *Tholen et al. (2000)*. Table 2.2 gathers the data collected. The amplitude is the

ratio of the maximum and minimum Newtonian forces and is useful to have an idea of the rate of change of the latter. Note that the Earth gravitational force is constant since L5 is always 1 AU away from Earth. From these results, we immediately conclude that Mercury as well as Uranus and Neptune are not pertinent for the following of our study since their effects are most of the time an order of magnitude lower than those of the other planets. In the following, we will only consider the perturbations resulting from Venus, the Earth, Mars, Jupiter and Saturn.

Planet	**Max. force (N/kg)**	**Min. force (N/kg)**	**Amplitude**
Mercury	$2.6216\,10^{-9}$	$5.1183\,10^{-10}$	5.1219
Venus	$1.8970\,10^{-7}$	$4.8893\,10^{-9}$	38.7990
Earth	$1.7816\,10^{-8}$	$1.7816\,10^{-8}$	1
Mars	$6.9809\,10^{-9}$	$3.0057\,10^{-10}$	23.2252
Jupiter	$3.2048\,10^{-7}$	$1.4714\,10^{-7}$	2.1780
Saturn	$2.3263\,10^{-8}$	$1.5270\,10^{-8}$	1.5234
Uranus	$7.8267\,10^{-10}$	$6.3530\,10^{-10}$	1.2320
Neptune	$3.6154\,10^{-10}$	$3.1649\,10^{-10}$	1.1423

Table 2.1: Maximum and minimum gravitational force produced at the location of the triangular Sun-Earth libration points for the eight planets of the Solar System. The amplitude is defined as the ratio between maximum and minimum force.

Planet	**Mass (10^{24} kg)**	a_k **(AU)**	$q_k = m_k/m_0$
Mercury	0.33022	0.38709893	$1.6607\,10^{-7}$
Venus	4.869	0.72333199	$2.4487\,10^{-6}$
Earth	5.9742	1.0	$3.0045\,10^{-6}$
Mars	0.64191	1.52366231	$3.2283\,10^{-7}$
Jupiter	1898.7	5.20336301	$9.5489\,10^{-4}$
Saturn	568.51	9.53707032	$2.8591\,10^{-4}$
Uranus	86.849	19.19126393	$4.3678\,10^{-5}$
Neptune	102.44	30.06896348	$5.1519\,10^{-5}$

Table 2.2: Mass, semi-major axis and mass ratio of the eight planets of the Solar system. In the last column, m_0 stands for the mass of the Sun.

2.2 Long-term impact of other planets

Let us consider the restricted circular three-body problem applied to the case of the Sun-Earth system. The total gravitational potential sensed in this system is called the Roche potential. Let m_0 be the mass of the Sun while the planets of the Solar System are identified by a number increasing with their distance to the Sun (e.g. $j = 1 \equiv$ Mercury, $j = 2 \equiv$ Venus, $j = 3 \equiv$ Earth,...). The semi-major axis of the orbit of planet j is therefore named a_j. Let us also consider a co-rotating coordinate system attached to the center of mass of the Sun-Earth system, that we will consider to be the center of the Sun. Then, the X axis permanently points in the direction of the Earth while the Y axis is parallel to the velocity of the latter on its orbit around the Sun. The Z axis is chosen in such a way to have a dextrogyrate frame. The Roche potential in such a system is expressed as

$$\Phi_{\text{Roche}} = \frac{G\,m_0}{\sqrt{X^2+Y^2+Z^2}} + \frac{G\,m_3}{\sqrt{(a_3-X)^2+Y^2+Z^2}} + \frac{n_3^2}{2}\left(X^2+Y^2\right) - \frac{n_3^2\,m_3}{m_0+m_3}\,a_3\,X \quad (2.2)$$

with $n_3^2 = \frac{G\,(m_0+m_3)}{a_3^3}$.

In order to have an idea of the long-term effect of other planets on this potential, we adopt the Gauss model, acquired from *Fitzpatrick R., 2012*. The idea behind that model is to average planets interaction over their orbital period. As the triangular points rotate together with the Earth around the Sun, the temporal validity of that model is driven by the synodic period of the other planets. Indeed, the higher is the synodic period of a planet, the more time will be required for its gravitational influence to be averaged on a circle. In the Solar System, the largest synodic period is slightly greater than 2 years and attributed to Mars. At least, 2 years are needed to average the effect of the red planet. However, it is safer to consider the Gauss model to be valid after a period of time 5 to 10 times longer than the largest synodic period. This further allows to average the effect of the orbital eccentricity of the other planets. All in all, the Gauss model therefore describes the gravitational impact of the Solar system planets on the Lagrangian points on timescales greater than 10 to 20 years. Let us then assume that the orbits of the perturbing planets are tied to the ecliptic such that they are moving in the same plane. Each planet is represented by a ring of radius a_k centred on the Sun. The potential due to such a uniform ring of mass m_k at some point $\vec{r_j}$ inside the ecliptic is given by

$$U_{j,k} = \frac{G\,m_k}{2\,\pi}\int_0^{2\,\pi}\frac{1}{|\vec{r_j}-\vec{r_k}|}d\phi \quad (2.3)$$

For $a_j > a_k$, we have

$$\frac{1}{|\vec{r_j}-\vec{r_k}|} = \frac{1}{a_j}\sum_{n=0}^{\infty}\left(\frac{a_k}{a_j}\right)^n P_n(\cos\phi) \quad (2.4)$$

whilst for $a_j < a_k$, we have

$$\frac{1}{|\vec{r_j} - \vec{r_k}|} = \frac{1}{a_k} \sum_{n=0}^{\infty} \left(\frac{a_j}{a_k}\right)^n P_n(\cos\phi) \tag{2.5}$$

where $P_n(x)$ are the Legendre polynomials of degree n, expressed as

$$P_n(x) = \frac{1}{2^n n!} \frac{d^n}{dx^n}(x^2 - 1)^n \tag{2.6}$$

This leads to a total perturbing potential

$$U_j = \sum_{n=0}^{\infty} s_n \left[\sum_{k<j} \frac{G\,m_k}{r} \left(\frac{a_k}{r}\right)^n + \sum_{j<k} \frac{G\,m_k}{a_k} \left(\frac{r}{a_k}\right)^n \right] \tag{2.7}$$

where the coefficients

$$s_n = \frac{1}{2\,\pi} \int_0^{2\,\pi} P_n(\cos\phi)\, d\phi \tag{2.8}$$

are zero for odd values of n and amount to $P_n(0)^2$ for even values of n. Thus $s_0 = 1$, $s_2 = \frac{1}{4}$, $s_4 = \frac{9}{64}$, $s_6 = \frac{25}{256}$,...

The perturbed Roche potential for j=3 hence becomes:

$$\begin{aligned} \Phi &= \frac{G\,m_0}{\sqrt{X^2+Y^2+Z^2}} + \frac{G\,m_3}{\sqrt{(a_3-X)^2+Y^2+Z^2}} + \frac{n_3^2}{2}\left(X^2+Y^2\right) - \frac{n_3^2\,m_3}{m_0+m_3}\,a_3\,X \\ &+ \sum_{n=0}^{\infty} s_n \left[\sum_{k<3} \frac{G\,m_k}{r} \left(\frac{a_k}{r}\right)^n + \sum_{3<k} \frac{G\,m_k}{a_k} \left(\frac{r}{a_k}\right)^n \right] \end{aligned} \tag{2.9}$$

We can normalize this potential dividing by $\frac{G\,m_0}{a_3}$ and introducing $x = X/a_3$, $y = Y/a_3$, $z = Z/a_3$:

$$\begin{aligned} \Phi' &= \frac{1}{\sqrt{x^2+y^2+z^2}} + \frac{q_3}{\sqrt{(1-x)^2+y^2+z^2}} + \frac{1+q_3}{2}\left(x^2+y^2\right) - q_3\,x \\ &+ \sum_{n=0}^{\infty} s_n \left[\sum_{k<3} \frac{q_k}{\sqrt{x^2+y^2+z^2}} \left(\frac{a_k}{\sqrt{x^2+y^2+z^2}}\right)^n + \sum_{3<k} \frac{q_k}{a_k} \left(\frac{\sqrt{x^2+y^2+z^2}}{a_k}\right)^n \right] \end{aligned} \tag{2.10}$$

where q_k is the ratio of masses m_k and m_0, the latter being the mass of the Sun.

The coordinates of the Lagrangian points of the classical Roche potential are solution of

$$\vec{\nabla}\,\Phi'_{\rm Roche} = \vec{0} \Rightarrow \left\{ \begin{array}{rcll} \frac{\partial\,\Phi'_{\rm Roche}}{\partial x} &=& -\frac{x}{[x^2+y^2+z^2]^{3/2}} - \frac{q_3\,(x-1)}{[(1-x)^2+y^2+z^2]^{3/2}} + (1+q_3)\,x - q_3 &= 0 \\ \frac{\partial\,\Phi'_{\rm Roche}}{\partial y} &=& -\frac{y}{[x^2+y^2+z^2]^{3/2}} - \frac{q_3\,y}{[(1-x)^2+y^2+z^2]^{3/2}} + (1+q_3)\,y &= 0 \\ \frac{\partial\,\Phi'_{\rm Roche}}{\partial z} &=& -\frac{z}{[x^2+y^2+z^2]^{3/2}} - \frac{q_3\,z}{[(1-x)^2+y^2+z^2]^{3/2}} &= 0 \end{array} \right. \tag{2.11}$$

The last equation gives $z = 0$ and all five Lagrangian points lie thus in the ecliptic plane. The collinear points are found when we set $y = 0$ and the first expression gives their x coordinates. We obtain the coordinates of L4 and L5 by imposing $y \neq 0$ in the second expression. Solving both systems of equation yields the approximate (in the case of L1, L2 and L3) coordinates outlined in Table 2.3.

	x (AU)	**y (AU)**
L1	$1 - \left(\frac{q_3}{3}\right)^{\frac{1}{3}}$	0
L2	$1 + \left(\frac{q_3}{3}\right)^{\frac{1}{3}}$	0
L3	$-\left(1 + \frac{5q_3}{12}\right)$	0
L4	$1/2$	$\sqrt{3}/2$
L5	$1/2$	$-\sqrt{3}/2$

Table 2.3: Coordinates of the 5 Lagrangian points of the Sun-Earth system. $q_3 = 3.0045\,10^{-6}$ is the mass ratio of the Earth. Expressions for the collinear points are correct up to the order $\frac{1}{3}$ in q_3 for L1 and L2 and to order 1 for L3. Values taken from [8].

As we want to study the vicinity of L5 and according to our previous selection of perturbing planets, there is only 1 planet lying inside 1 AU (Venus) and 3 outside (Mars, Jupiter and Saturn). For the modified potential, the gradient therefore becomes

$$\begin{aligned}
\frac{\partial\,\Phi'}{\partial x} &= -\frac{x}{[x^2+y^2+z^2]^{3/2}} - \frac{q_3\,(x-1)}{[(1-x)^2+y^2+z^2]^{3/2}} + (1+q_3)\,x - q_3 \\
&+ \sum_{n=0}^{\infty} s_n \left[-\sum_{k<3} \frac{q_k\,(n+1)\,a_k^n\,x}{[x^2+y^2+z^2]^{\frac{n+3}{2}}} + \sum_{3<k} \frac{q_k\,n}{a_k^{n+1}}\,[x^2+y^2+z^2]^{n/2-1}\,x \right] \qquad (2.12) \\
\frac{\partial\,\Phi'}{\partial y} &= -\frac{y}{[x^2+y^2+z^2]^{3/2}} - \frac{q_3\,y}{[(1-x)^2+y^2+z^2]^{3/2}} + (1+q_3)\,y \\
&+ \sum_{n=0}^{\infty} s_n \left[-\sum_{k<3} \frac{q_k\,(n+1)\,a_k^n\,y}{[x^2+y^2+z^2]^{\frac{n+3}{2}}} + \sum_{3<k} \frac{q_k\,n}{a_k^{n+1}}\,[x^2+y^2+z^2]^{n/2-1}\,y \right] \qquad (2.13) \\
\frac{\partial\,\Phi'}{\partial z} &= -\frac{z}{[x^2+y^2+z^2]^{3/2}} - \frac{q_3\,z}{[(1-x)^2+y^2+z^2]^{3/2}} \\
&+ \sum_{n=0}^{\infty} s_n \left[-\sum_{k<3} \frac{q_k\,(n+1)\,a_k^n\,z}{[x^2+y^2+z^2]^{\frac{n+3}{2}}} + \sum_{3<k} \frac{q_k\,n}{a_k^{n+1}}\,[x^2+y^2+z^2]^{n/2-1}\,z \right] \qquad (2.14)
\end{aligned}$$

with $k = 2$, 4, 5 and 6.

The z component of the gradient is clearly zero everywhere in the plane of the ecliptic. We can go further by calculating the second derivatives of the perturbed potential in the ecliptic (which

are the only non-zero derivatives). This gives the following expressions

$$\begin{aligned}
\frac{\partial^2 \Phi'}{\partial x^2} &= -\frac{1}{[x^2+y^2+z^2]^{3/2}} + \frac{3x^2}{[x^2+y^2+z^2]^{5/2}} - \frac{q_3}{[(1-x)^2+y^2+z^2]^{3/2}} + \frac{3q_3\,(x-1)^2}{[(1-x)^2+y^2+z^2]^{5/2}} \\
&+ 1 + q_3 + \sum_{n=0}^{\infty} s_n \left[-\sum_{k<3} \frac{q_k\,(n+1)\,a_k^n}{[x^2+y^2+z^2]^{\frac{n+3}{2}}} - \sum_{k<3} \frac{q_k\,(n+1)\,(n+3)\,a_k^n\,x^2}{[x^2+y^2+z^2]^{\frac{n+5}{2}}} \right. \\
&+ \left. \sum_{3<k} \frac{q_k\,n}{a_k^{n+1}}\,[x^2+y^2+z^2]^{n/2-1} + \sum_{3<k} \frac{q_k\,n\,(n-2)}{a_k^{n+1}}\,[x^2+y^2+z^2]^{n/2-2}\,x^2 \right] \qquad (2.15) \\
\frac{\partial^2 \Phi'}{\partial y^2} &= -\frac{1}{[x^2+y^2+z^2]^{3/2}} + \frac{3y^2}{[x^2+y^2+z^2]^{5/2}} - \frac{q_3}{[(1-x)^2+y^2+z^2]^{3/2}} + \frac{3q_3\,y^2}{[(1-x)^2+y^2+z^2]^{5/2}} \\
&+ 1 + q_3 + \sum_{n=0}^{\infty} s_n \left[-\sum_{k<3} \frac{q_k\,(n+1)\,a_k^n}{[x^2+y^2+z^2]^{\frac{n+3}{2}}} - \sum_{k<3} \frac{q_k\,(n+1)\,(n+3)\,a_k^n\,y^2}{[x^2+y^2+z^2]^{\frac{n+5}{2}}} \right. \\
&+ \left. \sum_{3<k} \frac{q_k\,n}{a_k^{n+1}}\,[x^2+y^2+z^2]^{n/2-1} + \sum_{3<k} \frac{q_k\,n\,(n-2)}{a_k^{n+1}}\,[x^2+y^2+z^2]^{n/2-2}\,y^2 \right] \qquad (2.16) \\
\frac{\partial^2 \Phi'}{\partial x \partial y} &= \frac{3xy}{[x^2+y^2+z^2]^{5/2}} + \frac{3q_3\,(x-1)y}{[(1-x)^2+y^2+z^2]^{5/2}} \\
&+ \sum_{n=0}^{\infty} s_n \left[-\sum_{k<3} \frac{q_k\,(n+1)\,(n+3)\,a_k^n\,x\,y}{[x^2+y^2+z^2]^{\frac{n+5}{2}}} + \sum_{3<k} \frac{q_k\,n\,(n-2)}{a_k^{n+1}}\,[x^2+y^2+z^2]^{n/2-2}\,x\,y \right] \qquad (2.17)
\end{aligned}$$

with $k = 2$, 4, 5 and 6.

We can then evaluate the norm of the gradient of the potential and compare it to the gradient of the standard Roche potential. For this, we truncate the sum over n to the order 6 and evaluate the gradients at some points (x,y,0) of the ecliptic plane. Figure 2.1 illustrates both gradients in the entire orbital plane, in the vicinity of L1 and L2 and close to L5. Overall, the impact of the modification on the potential is modest. If we specifically compute the values of the potential and of its gradient in L5, we obtain $\Phi'_{\text{Roche}} = 1.5000030$, $|\nabla \vec{\Phi'_{\text{Roche}}}| = 5.0867\,10^{-16}$ for the pure Roche potential, and $\Phi' = 1.50022145$, $|\nabla \vec{\Phi}'| = 3.4091\,10^{-7}$ for the modified potential. The modifications are rather small for $\vec{\Phi}'$, but $\nabla \vec{\Phi}' \neq \vec{0}$ which strictly implies that L5 is not an equilibrium point anymore.

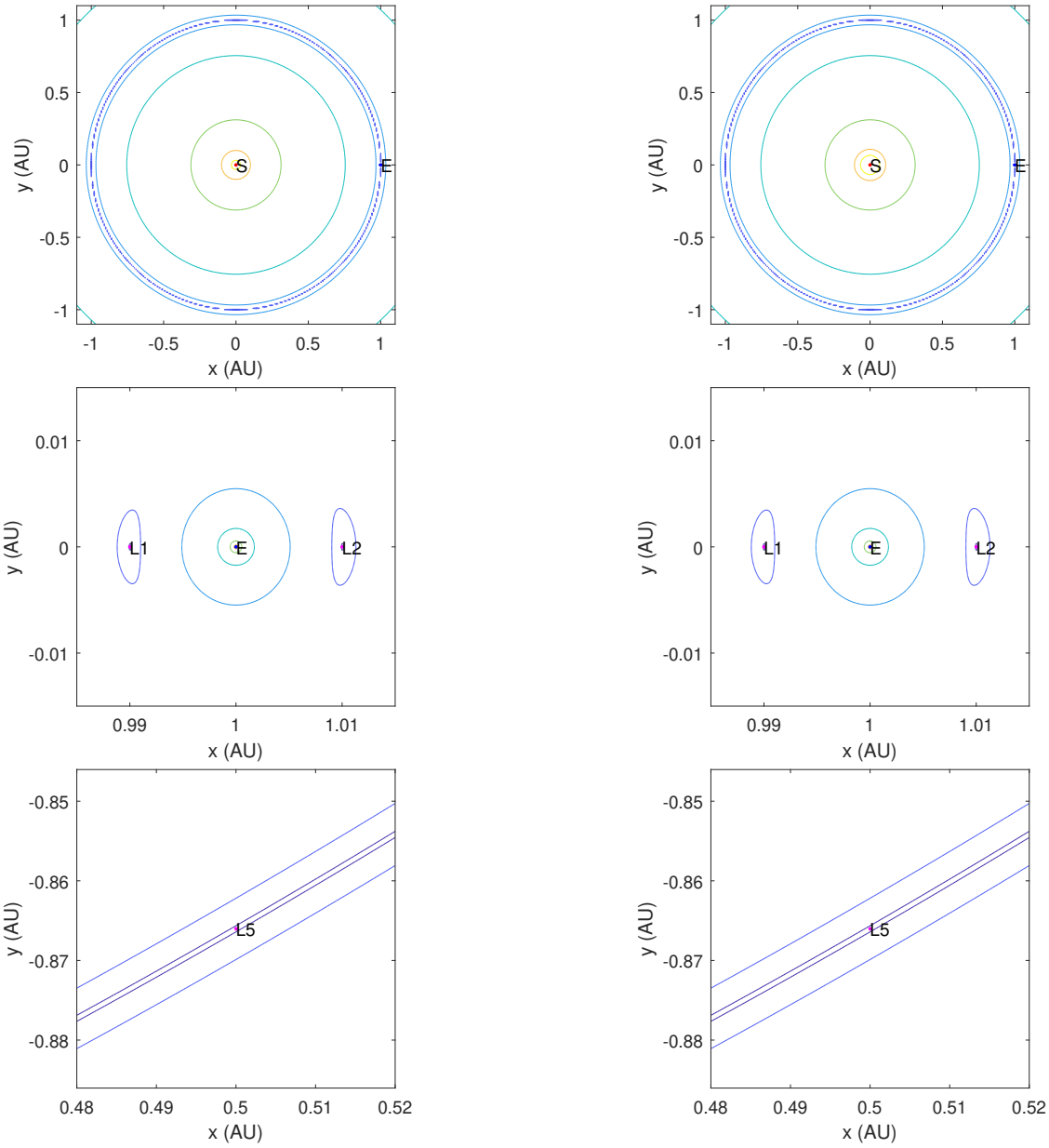

Figure 2.1: Comparison of the norm of the gradient of the potential in the plane of the ecliptic in the case of the pure Roche potential (left) and the modified potential (right). Contours of equal values of log $|\vec{\nabla}\Phi'|$ are shown for values of -3.0 (indigo), -2.0 (dark blue), -1.0 (light blue), 0.0 (cyan), 1.0 (light green), 2.0 (orange) and 3.0 (yellow). The top, middle and lower panels correspond to the whole orbital plane, the neighbourhood of the L1 and L2 points, and the vicinity of L5, respectively.

2.3 Search for new stable points

From the preceding section, we have concluded that L5 is not a point where the gradient of the modified potential is rigorously zero. An interesting verification could be performed in the vicinity of L5 to search for new stable points, i.e. a point different from L5 where the gradient is closer to zero than in L5. This could be useful to place a satellite in orbit around that hypothetical point instead of L5. For this, we evaluate the gradient of the perturbed potential

$|\vec{\nabla}\Phi'|$ in a squared box of width 0.2 AU around L5 and draw the latter in a contour plot shown in Figure 2.2. In order to assess the stability of a point of a multi-variable function, we introduce the Hessian matrix:

$$H(x,y) = \begin{pmatrix} \frac{\partial^2 \Phi'}{\partial x^2} & \frac{\partial^2 \Phi'}{\partial x \partial y} \\ \frac{\partial^2 \Phi'}{\partial x \partial y} & \frac{\partial^2 \Phi'}{\partial y^2} \end{pmatrix} \tag{2.18}$$

From this definition, a point (x, y) in a plane is stable if $det|H(x,y)| > 0$ and $\frac{\partial^2 \Phi'}{\partial x^2} > 0$. Figure 2.3 shows the determinant of the Hessian matrix and its $(1,1)$ component for the same squared box as for the gradient $|\vec{\nabla}\Phi'|$. At first sight there is no point distinct from L5 where all the above mentioned conditions are met. This is expected as regards to the Gauss model. In fact, over relatively small distances around L5, the averaging of planets interaction throughout their orbits has the only effect of raising the zero level of the Roche potential gradient. For this reason there is no chance to find another stable point in the vicinity of L5 in the plane of the ecliptic.

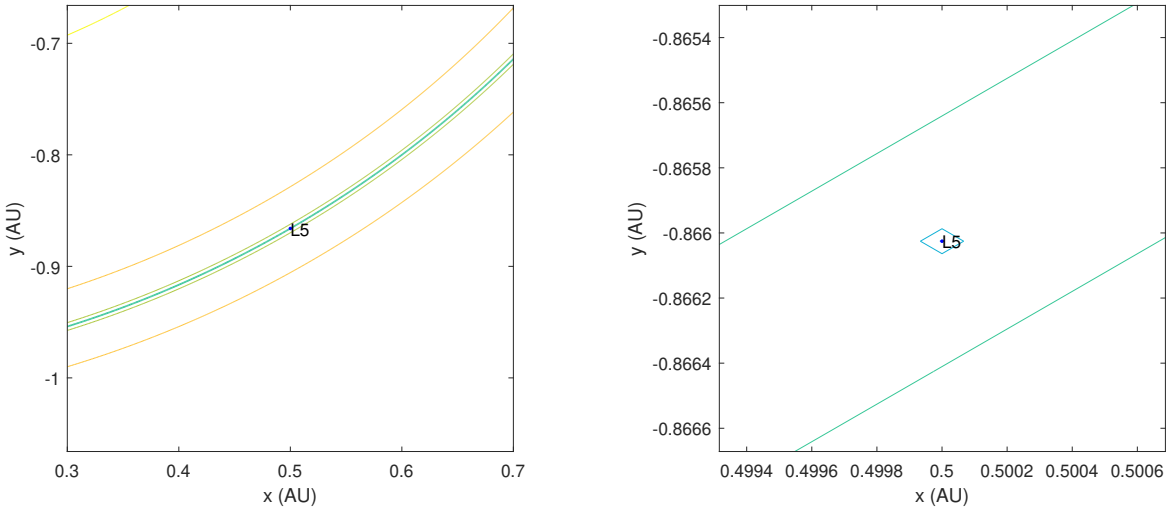

Figure 2.2: Norm of the gradient of the potential in the plane of the ecliptic in the vicinity of L5 (left) and a zoomed view of that gradient (right). Contours of equal values of log $|\vec{\nabla}\Phi'|$ are shown for values of -6.0 (dark blue), -5.0 (light blue), -4.0 (cyan), -3.0 (green), -2.0 (khaki colour), -1.0 (orange) and 0 (yellow).

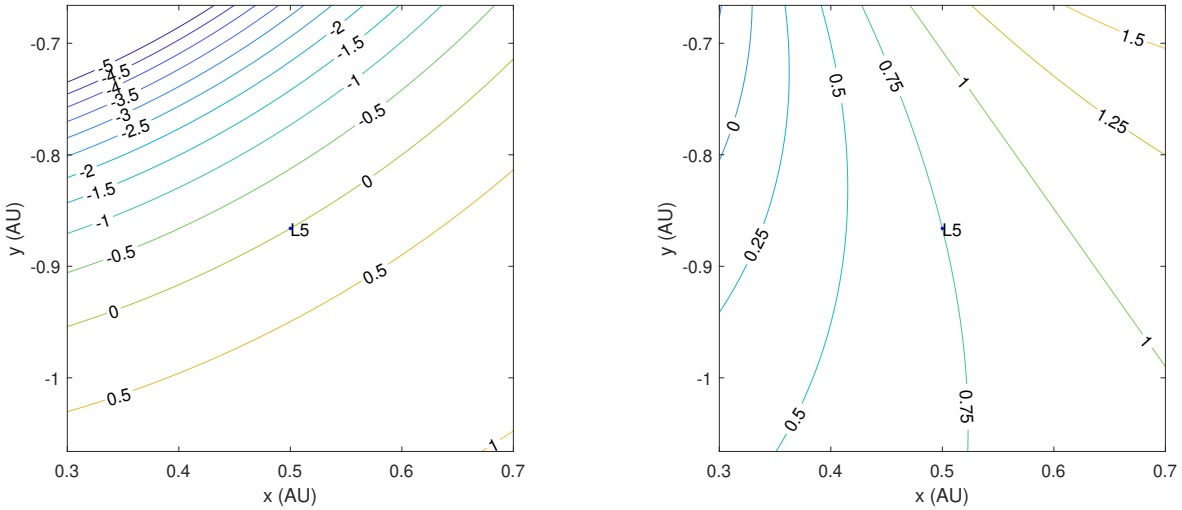

Figure 2.3: Determinant of the Hessian matrix (left) and second derivative $\frac{\partial^2 \Phi'}{\partial x^2}$ (right) in the plane of the ecliptic in the vicinity of L5. Contours of equal values are shown with steps of 0.5 (left) and 0.25 (right).

Chapter 3

Early trajectory implementation

The purpose of the present chapter is to describe the dynamics around the triangular Lagrangian points and to derive confined orbits around them, first in the circular Sun-Earth system and then in the whole Solar system. The effect of the perturbing planets is this time directly assessed in terms of orbit instabilities. We also consider the case of Jupiter's Trojans for which we have mimicked their trajectories and studied the relevance of these orbits as end-of-life disposal orbits. In this context, a delta-V analysis is also presented. Once again, the whole computations as well as the numerical propagation have been carried out with the MATLAB software (2018a version).

This chapter is not dedicated to a rigorous in-depth study of the dynamics in the vicinity of the triangular Lagrangian points. In our current model, we neither account for the ellipticity of the Earth's orbit around the Sun nor the solar radiation pressure (SRP). These two relevant aspects are put aside and left to forthcoming chapters. Rather, the goal of this part is to give a qualitative insight of the dynamics around L5 and highlight some of the major results that will drive the rest of this work.

3.1 Libration trajectory

3.1.1 Libration in the circular Sun-Earth system

In the frame of the circular restricted three-body problem, one can assess the stability of the Lagrangian points. As widely established for two hundred years, the triangular points are stable if the mass ratio of the two main bodies is larger than 24.96[1], while it is never the case for the collinear points. This means that if a satellite is introduced at a position slightly away from L5, it will start orbiting around the latter. There exist two such types of orbits, called libration modes. For such modes, the out-of-plane motion is perfectly decoupled from the in-plane dynamics

[1]Note that some values of the mass ratio lower than 24.96 lead to unstable triangular points (*Deprit A., 1965*). This is however not the case for the Sun-Earth system.

(*Rauw G., 2019*). That is to say, if the satellite starts with a zero out-of-plane velocity, its trajectory will be confined in a region around the ecliptic. For this reason and for the sake of simplicity, we will only focus on the planar motion in the following of this chapter. Let us thus consider a (x', y') coordinate system attached to the L5 point of the Sun-Earth system. The Y' axis is aligned with the line connecting the Sun to L5 and directed outwards. The X' axis makes a 90° angle with the Y' axis and is oriented clockwise. The resulting rotating frame is shown in Figure 3.1 together with an inertial frame centred on the Sun, and with the X axis initially pointing towards the Earth.

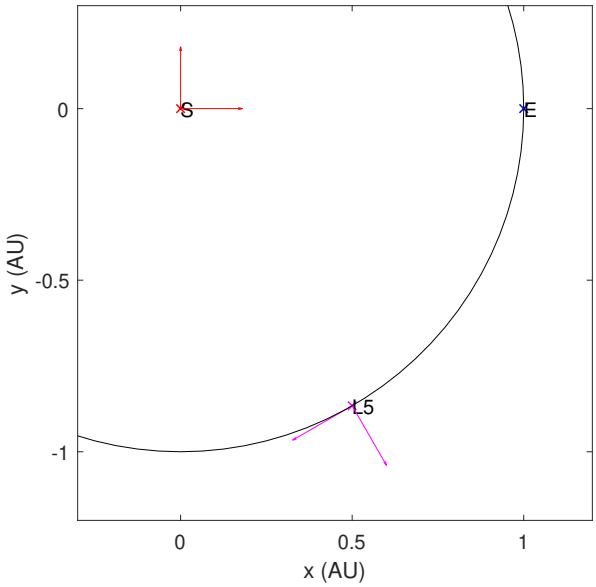

Figure 3.1: Co-rotating frame attached to L5 (magenta) and inertial frame centred on the Sun (red). The inertial X axis initially points towards the Earth.

In such a frame, the linearized long-period oscillation modes are described by the motions (*Rauw G., 2019*):

$$\delta x' = X_{lp}\, cos\left[\frac{3\sqrt{3\epsilon}}{2}\, n_3\, t + \phi_{lp}\right] \tag{3.1}$$

$$\delta y' = -\sqrt{3\epsilon}\, X_{lp}\, sin\left[\frac{3\sqrt{3\epsilon}}{2}\, n_3\, t + \phi_{lp}\right] \tag{3.2}$$

where $n_3 = \sqrt{\frac{G(m_0+m_3)}{a_3^3}}$ and $\epsilon = \left(1 + \frac{m_0}{m_3}\right)^{-1}$ with m_0 and m_3 the mass of the Sun and the mass of the Earth respectively. Taking the values from Tholen et al. (2000), we obtain $n_3 = 1.9909\,10^{-7}\,s^{-1}$ and $\epsilon = 3.0045\,10^{-6}$.

The linearized short-period oscillations modes are given by:

$$\delta x' = X_{sp}\, cos\left[\left(1 - \frac{27\epsilon}{8}\right) n_3\, t + \phi_{sp}\right] \tag{3.3}$$

$$\delta y' = -\frac{X_{sp}}{2}\, sin\left[\left(1 - \frac{27\epsilon}{8}\right) n_3\, t + \phi_{sp}\right] \tag{3.4}$$

The minus sign denotes a clockwise motion around L5. The amplitudes X_{lp} and X_{sp} and the phases ϕ_{lp} and ϕ_{sp} are determined by the initial conditions (e.g. the coordinates and the velocity of the orbiting mass at the initial time). The long-period libration trajectories are characterized by a period of about 222 years while the short-period ones orbit around L5 in 1 year. Regarding the small value of ϵ, we immediately conclude that the long-period libration modes will have a much larger amplitude along the X' axis. Figure 3.2 shows peculiar long and short-period trajectories in a frame co-rotating with the Earth around the Sun.

As the objective of future L5 missions would be to observe and monitor the solar activity, it is highly interesting to draw these trajectories in an inertial frame centred on the Sun. For this purpose, let us consider an inertial frame attached to the Sun, whose X axis initially points towards the Earth and the Y axis forms a right-handed system with the latter. The transformation from the (X',Y') system to the (X,Y) frame can be done with three successive steps: a rotation of 150°, a translation from L5 to the Sun and a last rotation that depends on time. The first rotation is given by:

$$\begin{pmatrix} x_{bis} \\ y_{bis} \end{pmatrix} = \begin{pmatrix} cos(150°) & sin(150°) \\ -sin(150°) & cos(150°) \end{pmatrix} \begin{pmatrix} x' \\ y' \end{pmatrix} \tag{3.5}$$

Then we apply the following translation:

$$x_{ter} = x_{bis} + 0.5\, AU \tag{3.6}$$

$$y_{ter} = y_{bis} - \frac{\sqrt{3}}{2}\, AU \tag{3.7}$$

The final rotation consists in a transformation from rotating axes to fixed inertial axes:

$$\begin{pmatrix} x \\ y \end{pmatrix} = \begin{pmatrix} cos(n_3\, t) & -sin(n_3\, t) \\ sin(n_3\, t) & cos(n_3\, t) \end{pmatrix} \begin{pmatrix} x_{ter} \\ y_{ter} \end{pmatrix} \tag{3.8}$$

Applying this three-step transformation to the libration trajectories and considering a particular mission lifetime, we can draw the resulting orbits. Figure 3.3 displays the obtained trajectories for a 20 years mission duration. Apparently, the short-period libration mode seems less adequate than the long-period mode since the spacecraft will be periodically closer and further from the

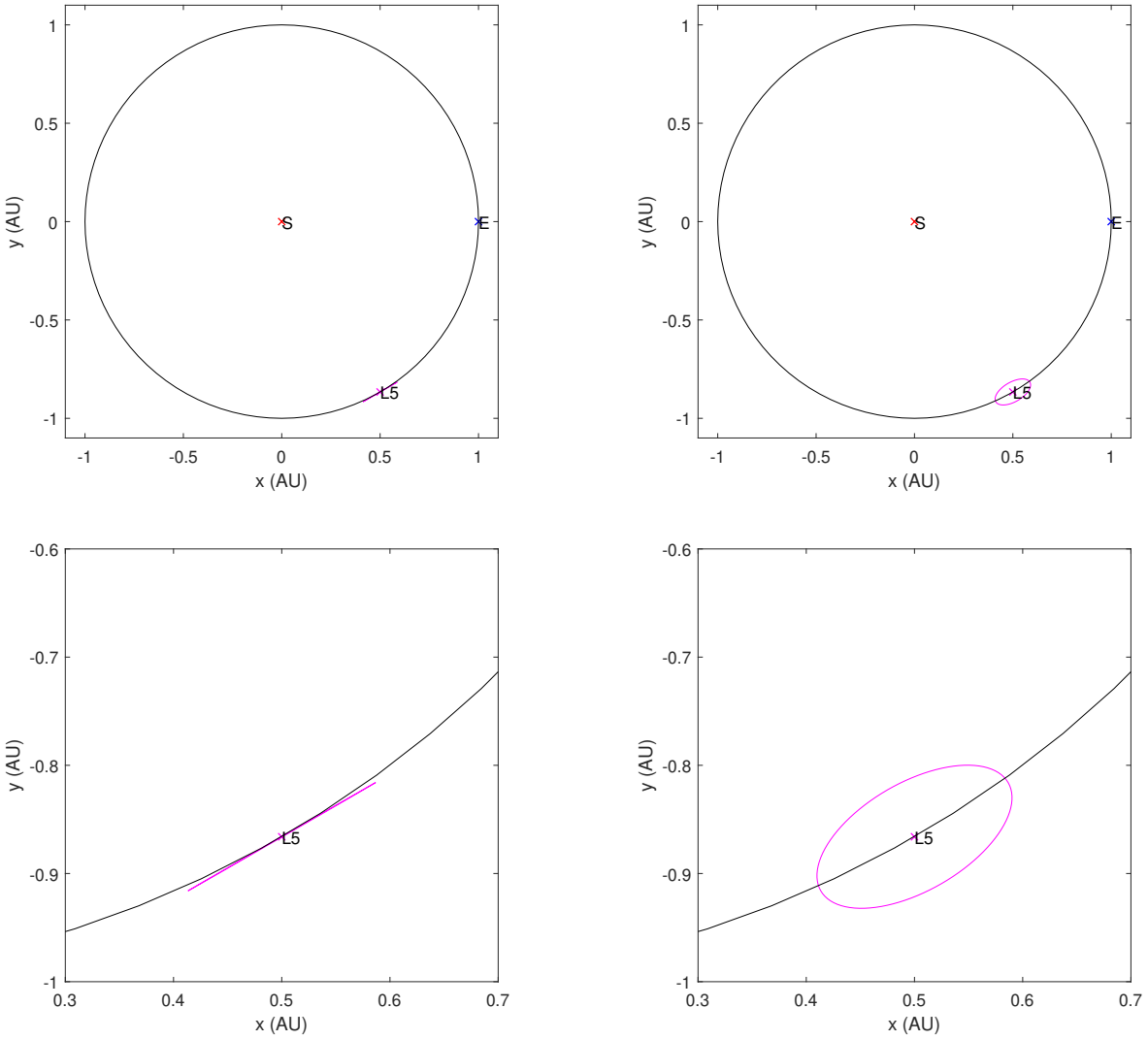

Figure 3.2: Representations of the long-period (left) and short-period (right) libration trajectories in the entire Solar system (top) and in the vicinity of L5 (bottom). The amplitude along the X' axis has been set to 0.1 AU for the sake of clarity.

Sun. This results in variable thermal and solar illumination conditions that will in turn have an impact on the lifetime of the mission. However, these effects can be mitigated by reducing the size of the orbit around L5.

An outcome that has been put aside so far is the slow precession encountered for short-period libration orbits. The term depending on ϵ in expressions (3.3) and (3.4) induces a 98619 year clockwise precession of the orbit. Obviously, the impact of such a slow precession on timescales of several decades is not perceptible and can be ignored in future mission analyses. Figure 3.4 exposes the effects of that slow precession on much larger timescales.

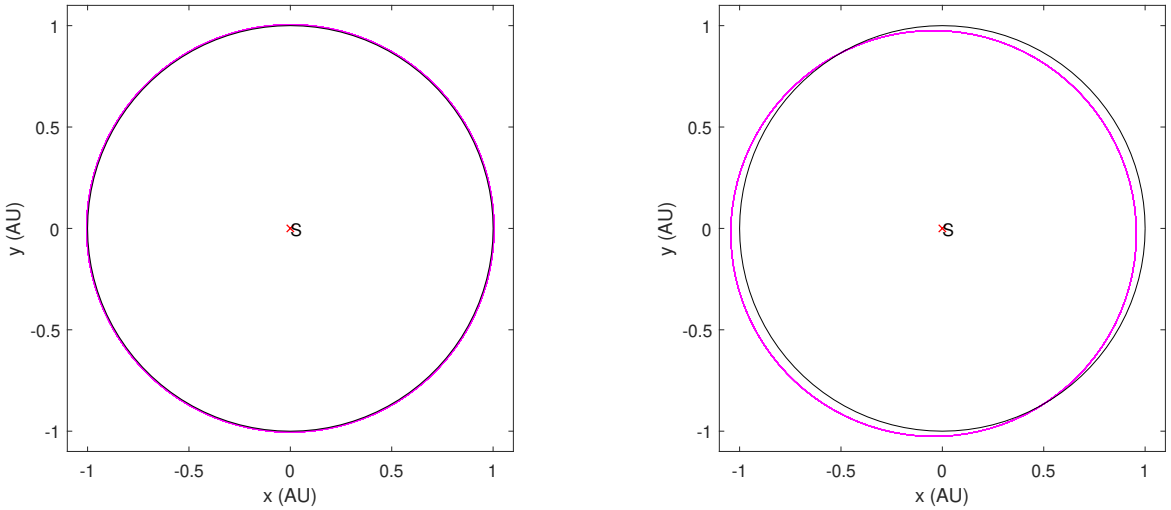

Figure 3.3: Representations of the long-period (left) and short-period (right) libration trajectories in the heliocentric frame. Orbits are drawn for a mission duration of 20 years and with an X' axis amplitude set to 0.1 AU.

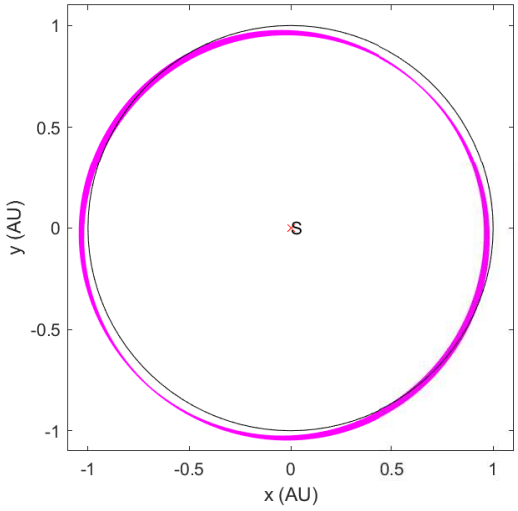

Figure 3.4: Representation of the precession experienced for short-period libration trajectories. A timescale of 10000 years has been considered to highlight the effect. The amplitude along the X' axis has been set to 0.1 AU for the sake of clarity.

3.1.2 Propagation in the circular Sun-Earth system

In order to verify that the libration orbits are indeed solution of the circular restricted three-body problem, it is necessary to propagate the obtained trajectories in the Sun-Earth system. For this, we first generate fake circular ephemeris for the Earth by imposing a constant 1 AU distance from the Sun, the latter being located at the center of the system. The satellite is placed at a position slightly away from L5 and we give it the velocity corresponding to the nominal libration trajectory. In other words, the initial positions and velocities of the short-period mode in the rotating frame are related by:

$$\delta x' = X_{sp}\, cos(\phi_{sp}) \tag{3.9}$$

$$\delta y' = -\frac{X_{sp}}{2}\, sin(\phi_{sp}) \tag{3.10}$$

$$\frac{\delta x'}{\delta t} = -X_{sp}\left(1 - \frac{27\epsilon}{8}\right) n_3\, sin(\phi_{sp}) \tag{3.11}$$

$$\frac{\delta y'}{\delta t} = -\frac{X_{sp}}{2}\left(1 - \frac{27\epsilon}{8}\right) n_3\, cos(\phi_{sp}) \tag{3.12}$$

Therefore, the amplitude X_{sp} and the phase ϕ_{sp} fully describe both the nominal orbit and the initial state. We then apply to expressions (3.9) to (3.12) the transformation sequence defined in subsection 3.1.1 to obtain the initial conditions in the inertial frame. At this stage, the purpose is to solve the Newtonian equations of motion for the satellite, considered as the third body of the system. In the inertial (X,Y) system previously defined, these two-dimensional equations take the form:

$$\ddot{x} = -G\left(m_0 \frac{x}{[x^2+y^2]^{3/2}} + m_3 \frac{x - x_3}{\left[(x-x_3)^2 + (y-y_3)^2\right]^{3/2}} + m_3 \frac{x_3}{[x_3^2+y_3^2]^{3/2}}\right) \tag{3.13}$$

$$\ddot{y} = -G\left(m_0 \frac{y}{[x^2+y^2]^{3/2}} + m_3 \frac{y - y_3}{\left[(x-x_3)^2 + (y-y_3)^2\right]^{3/2}} + m_3 \frac{y_3}{[x_3^2+y_3^2]^{3/2}}\right) \tag{3.14}$$

where (x, y) and (x_3, y_3) are respectively the coordinates of the satellite and the Earth.

In this part, we will only focus on the short-period orbit since we will propagate the initial state for 20 years, the typical lifetime of a space mission. The long-period mode having a period of about 222 years, the obtained trajectory would not really be an orbit around L5 and can be put aside. To carry out the propagation, we use the *ode45* solver available in Matlab. It implements a Runge-Kutta pair of order 4 and 5 with a variable step-size depending on the desired relative and absolute tolerances. The latter have both been set to 10^{-9}. At the end of the propagation, the results are presented in the rotating frame attached to L5.

The first parameter that will have an incidence on the propagation is the amplitude X_{sp} of the motion around L5. The short and long-period libration components are linearized solutions of the circular restricted three-body problem if the magnitude of the perturbation is negligible compared to the size of the system (i.e. the astronomical unit). Therefore, there exists a maximum allowed extent for the motion around L5. Figure 3.5 shows the effect of the initial amplitude on the propagation. In each case, the orbit drifts in the direction opposed to the Earth and its extent is proportional to the size of the initial orbit. This is due to the long-period

libration mode. In fact, whatever the initial linear conditions, both short and long-period modes are inherent to the circular Sun-Earth system. Any object in orbit around L4 or L5 will be driven by these two modes. The exact solution of the motion around the triangular libration points consists in an infinite sum of harmonic terms. The linear solution that we have considered above only accounts for the dominant term of this sum. Restricting ourselves to the linear term thus yields only an approximation the accuracy of which will depend on the amplitude. This is the consequence of the non-linear coupling between the amplitude and the frequency that cannot be predicted by linear theory. Without entering into details, this coupling is again specific to non-linear systems and is the manifestation of the chaotic behaviour of such systems (*Rand R. H., 2012*). Expressing the initial conditions needed for a stable short-period orbit in the context of the linear approximation, hence implies that the solution will be contaminated by higher-order long-period terms. To suppress any long-term drift and express only the short-period component, we would need the exact non-linear solution or a relatively accurate truncation of the latter. Also, numerical techniques have been developed to cancel out the non-desired mode (*Gomez G. et al., 2001*). Figure 3.6 highlights this oscillation motion and confirms that it is due to the long-period component since the period is indeed 222 years. Another point is the confinement of the orbit around the Earth path. This is simply the result of the conservation of energy. The satellite lies in-between the zero-velocity curves corresponding to its initial total energy. As it is far away from any body, it cannot exchange energy and therefore stays in-between these bounds. All in all, similar drifting orbits have been numerically obtained by Bobrov (*Bobrov O. A., 2014*) for the Sun-Jupiter system.

Both libration modes are linearized solutions of the circular restricted three-body problem, which one is far from linear as seen in equations (3.13) and (3.14). It is thus impossible to reproduce exactly the linear solutions but we can still approach them. As linear theory is increasingly valid when the scale of the perturbations is reduced, the smaller the orbit around L5, the longer the satellite will stay in the vicinity of L5 and the less correction manoeuvres will be required.

We can also vary the starting point on a peculiar orbit to evaluate the magnitude of the drift. This is shown in Figure 3.7 for the four extreme points of a short-period orbit with a $5\,10^5$ km amplitude. It appears that the extent and the direction of the drift depend also on the starting point. The latter can therefore be mitigated by properly choosing the phase ϕ_{sp}. Regarding Figure 3.7, there must exist four points[2] where the drift direction reverses and the corresponding amplitude is then minimum. These four points will lead to a quasi-zero drift and will be economically interesting as they allow a low-cost stabilisation of orbits. A simple program iterating through the phase component allows to find the four optimum ones. These are 65.64°, 114.01°, 245.76° and 293.79°. The last two are found to be approximately the anti-supplementary angles of the first ones, i.e. they are separated by a quasi-flat angle.

[2]One in each quadrant of the trigonometric circle, i.e. $(0, 90°)$, $(90°, 180°)$, $(180°, 270°)$ and $(270°, 360°)$.

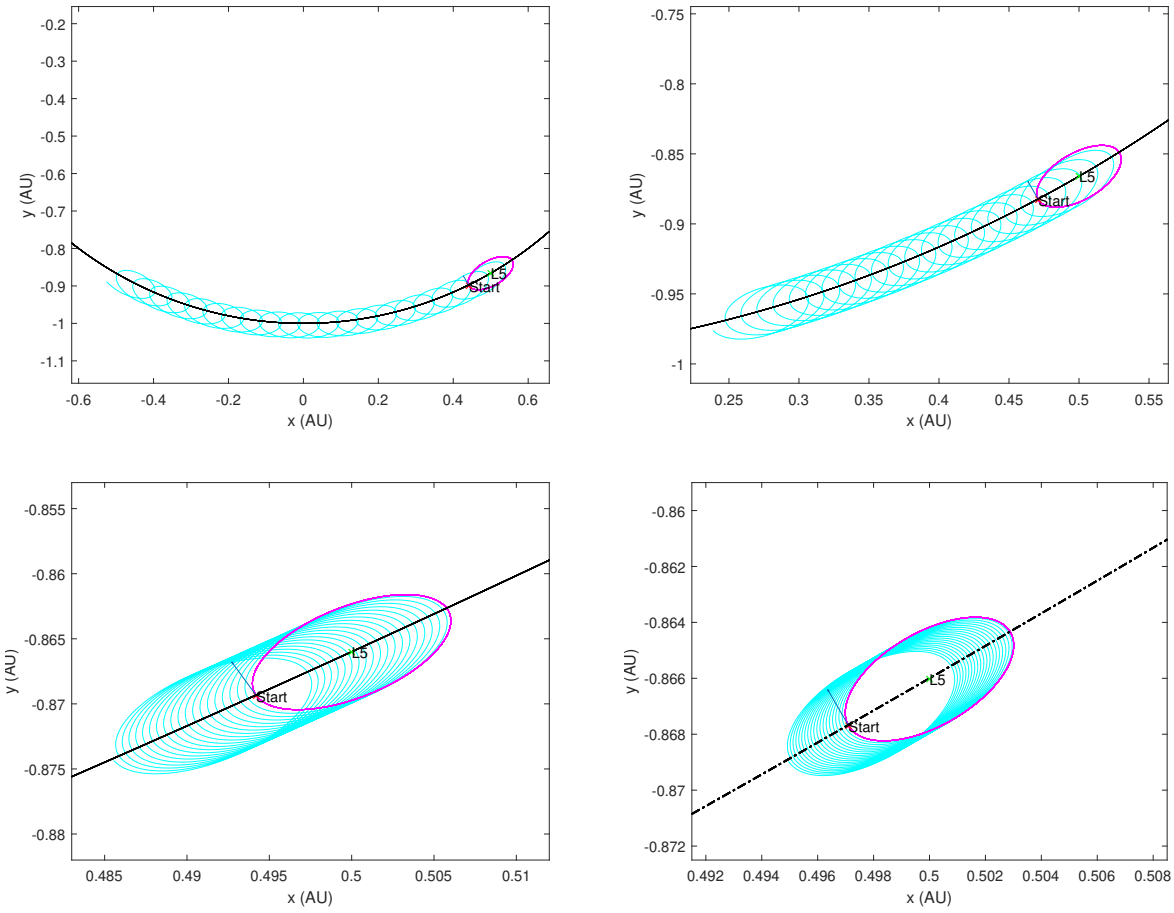

Figure 3.5: Effect of the amplitude of short-period libration orbits on a 20-year propagation in the Sun-Earth system. The initial amplitude (in km) is 10^7 (top left), $5\,10^6$ (top right), 10^6 (bottom left) and $5\,10^5$ (bottom right) respectively. The initial phase is zero for all cases. The magenta line denotes the expected short-period trajectory. The dark blue vector shows the initial velocity direction.

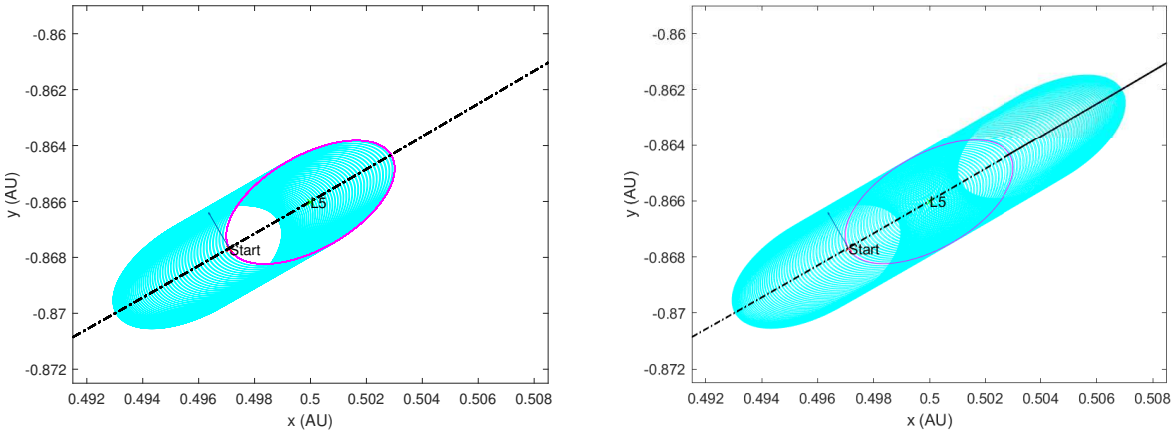

Figure 3.6: Drifting effect of the short-period libration orbits on a 111-year (left) and 222-year (right) propagation in the Sun-Earth system. The initial amplitude is $5\,10^5$ km and the phase is zero. The magenta line denotes the expected short-period trajectory. The dark blue vector shows the initial velocity direction.

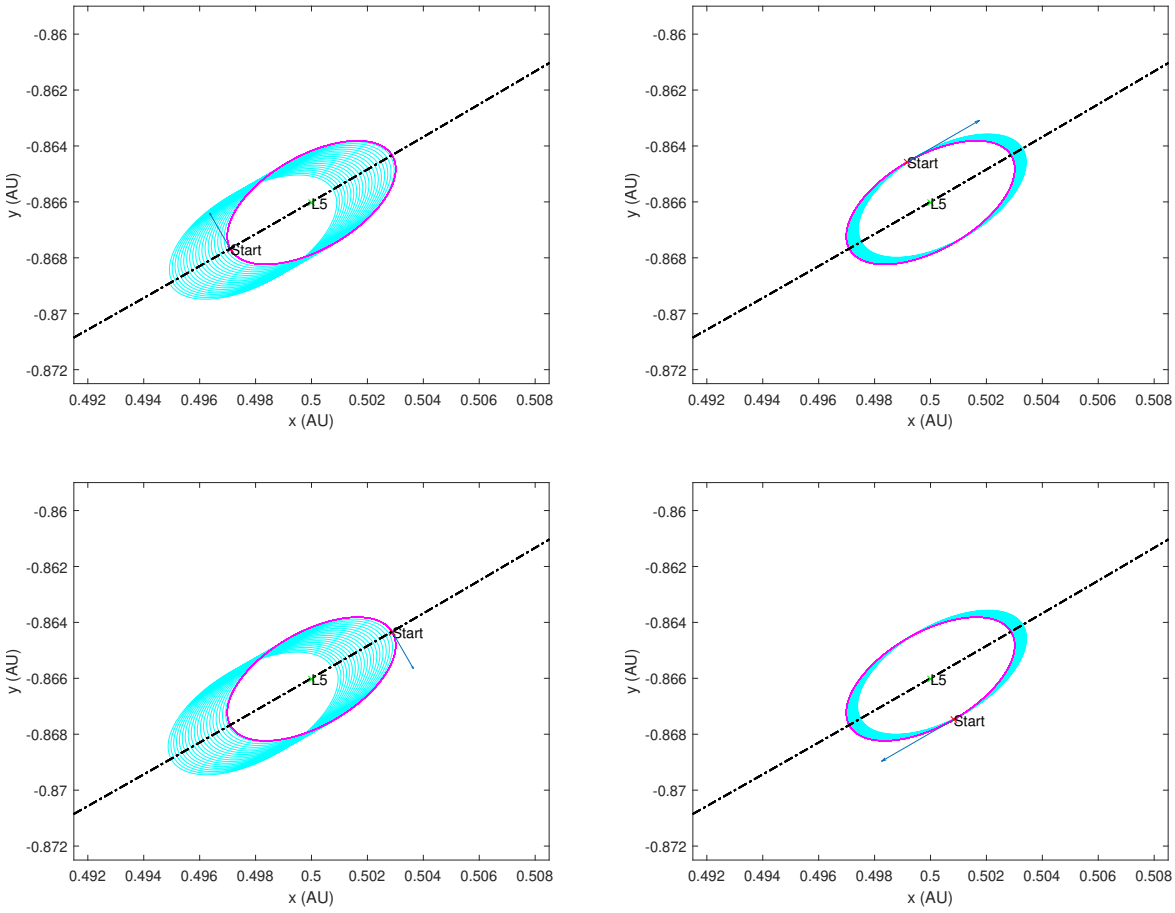

Figure 3.7: Effect of the phase component of short-period libration orbits on a 20-year propagation in the Sun-Earth system. The initial phase is 0° (top left), 90° (top right), 180° (bottom left) and 270° (bottom right) respectively. The amplitude is set to $5\,10^5$ km for all cases. The magenta line denotes the expected short-period trajectory. The dark blue vector shows the initial velocity direction.

It is not possible to derive the exact value of these angles from linear theory. Indeed, we would need to account for higher-order long-period and short-period terms to find the adequate initial conditions that minimize the long-period drift. This is beyond the scope of the present subsection and will be useless as we need to add the perturbations of the other planets to evaluate their importance. This is done in the next sub-section.

3.1.3 Propagation in the Solar system

The objective of this section is to evaluate the global impact of the other planets on the previously obtained short-period trajectories. For that purpose, we gather the planetary ephemeris (Venus, the Earth, Mars, Jupiter and Saturn) from the Miriade Ephemeris Generator developed by the *Observatoire de Paris* available on the website: `http://vo.imcce.fr/webservices/miriade/?forms`. We choose a time-step of 1 day starting on 22 January 2030 at 12:00 and ending on 22 January 2050 at 12:00. The rectangular coordinates are computed with the INPOP planetary model and given in the Astrometric J2000 reference frame. At this stage, we keep a fake circular

orbit for the Earth but starting at the initial true anomaly given in the Earth ephemeris file. The eccentricity of the Earth will be introduced later.

The equations of motion in the full Solar system are written:

$$\ddot{x} = -G\left(m_0 \frac{x}{[x^2+y^2]^{3/2}} + \sum_{i=2,3,4,5,6}\left[m_i \frac{x-x_i}{\left[(x-x_i)^2+(y-y_i)^2\right]^{3/2}} + m_i \frac{x_i}{[x_i^2+y_i^2]^{3/2}}\right]\right) \quad (3.15)$$

$$\ddot{y} = -G\left(m_0 \frac{y}{[x^2+y^2]^{3/2}} + \sum_{i=2,3,4,5,6}\left[m_i \frac{y-y_i}{\left[(x-x_i)^2+(y-y_i)^2\right]^{3/2}} + m_i \frac{y_i}{[x_i^2+y_i^2]^{3/2}}\right]\right) \quad (3.16)$$

where the indices still refer to the notations of Chapter 3. The integration parameters are identical to the previous sub-section and the results are again presented in the rotating frame. Figure 3.8 shows the effect of the perturbing planets on the satellite trajectory for a particular starting date. In this case, the overall behaviour is a shift towards the Earth whatever the initial long-period drift direction. Figure 3.9 illustrates the varying impact of the 5 perturbing planets for some departure dates and their initial configuration in the Solar system. We could try to evaluate which planet will act as the main perturbing body but this is hopeless. Since all the planets have a synodic period less than 2.5 years[3], they all complete several rotations as seen from L5. Therefore, it is highly compromised to disentangle the effects of the different planets. Indeed, no clear correlation between the direction of the shift and the initial position of the planets in Figure 3.9 is noticeable, even when choosing one of the four optimal phase component so that the long-period drift is cancelled. In order to evaluate their impact on the orbit, it would be more convenient to carry the propagation in the vicinity of the projected launch window to properly choose both the insertion point and the final departure date.

The last effect that needs to be investigated is the critical amplitude of the orbit. Indeed, the velocity on the trajectory being proportional to the size of the orbit (see expressions (3.11) and (3.12) as examples), there will be some critical amplitude for which the velocity is of the same order of magnitude as the velocity perturbations coming from the other planets. Below that amplitude, any orbit around L5 is unstable in the sense that it would be destabilized by any sufficiently "close" approach of planetary bodies. We also need to define what is meant by "destabilized". In the following, we will consider that the orbit is destabilized if, starting at one of the 4 optimal orbital phases found in the previous subsection, the magnitude of the drift is greater than the amplitude of the orbit. This means that the spacecraft is no more in orbit around L5 at the end of the 20 year propagation. Also, because the perturbations depend on the planet configuration at the beginning of the propagation, we will estimate the critical amplitude for 11 different dates, covering about 2 years. As Mars has a synodic period of 2.13 years, we

[3]Mars has a synodic period of about 779 days, i.e. 2.13 years, which is the highest in the Solar system.

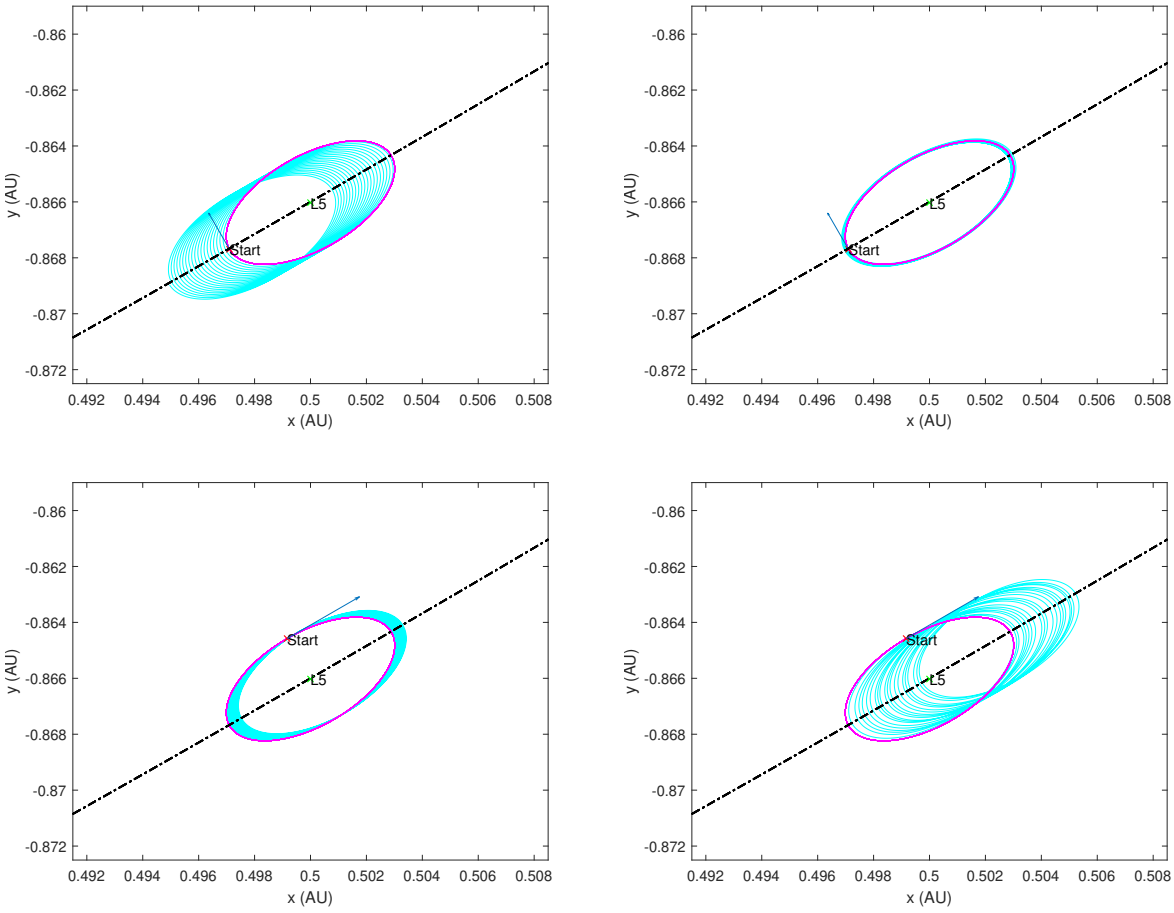

Figure 3.8: Short-period libration orbit propagation in the Sun-Earth system (left) and in the Solar system (right) taking into account the perturbations from Venus, Mars, Jupiter and Saturn. The propagation starts on 22 January 2030 at 12:00 and ends on 22 January 2050 at 12:00. The initial phase is 0° (top) or 90° (bottom) and the amplitude is set to $5\,10^5$ km for both cases. The magenta line denotes the expected short-period trajectory. The dark blue vector shows the initial velocity direction.

cover a wide range of possible configurations. Table 3.1 reports the minimum amplitude that is allowed in these 11 different configurations. As it can be seen, the critical amplitude varies by a factor of 10, from 5-6 10^4 to 5-6 10^5 km. There seems to be some configurations for which the orbit is super-stable (like the one starting on 28 November 2028), while some others lead to an easily destabilized motion (such as those of 2 May 2028 and 26 June 2029). Drawing the corresponding planetary configuration for these 3 dates (see Figure 3.10) allows to highlight the effect of Venus and Jupiter. Indeed, the two planets are initially located at their closest point to L5 in the two unstable cases while they are found 180 degrees away when considering the most stable orbit. This observation is in accordance with Table 2.1 which states that Jupiter and Venus could be the major perturbing bodies.

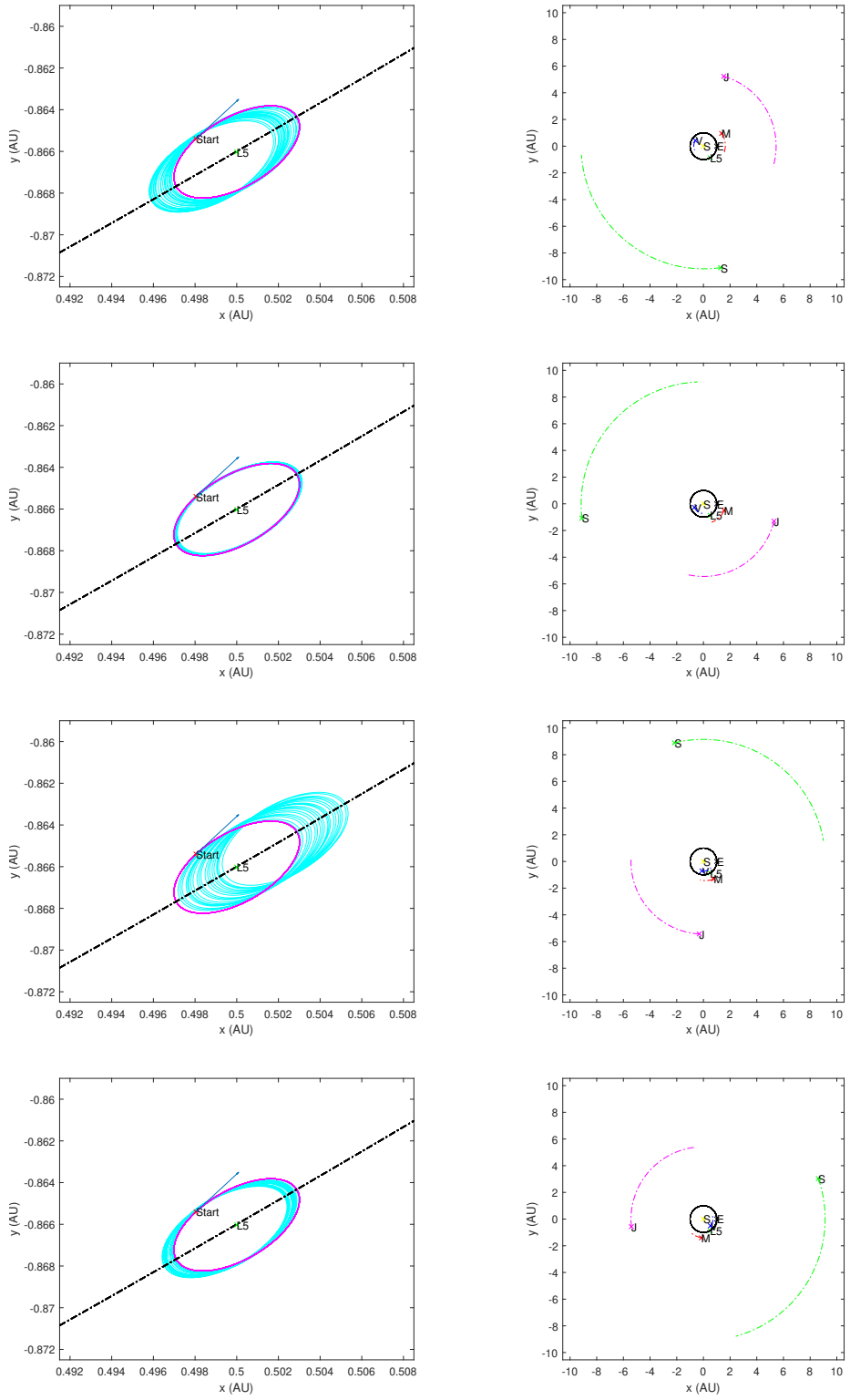

Figure 3.9: Short-period libration orbit propagation in the Solar system taking into account the perturbations from Venus (blue), Mars (red), Jupiter (magenta) and Saturn (green). The propagation time has been set to 20 years and starts on 22 January 2029 (top), 27 April 2029 (second row), 26 July 2029 (third row) and 24 October 2029 (bottom). The corresponding planet positions are shown to the right of each trajectory for the first 100 days of propagation. The initial phase is 65.64° and the amplitude is set to $5\,10^5$ km for all cases. The magenta line denotes the expected short-period trajectory. The dark blue vector shows the initial velocity direction.

Start date	**Critical amplitude (10^5 km)**
22/02/2028	3.2 - 3.4
02/05/2028	5.4 - 5.6
11/07/2028	1.0 - 1.2
19/09/2028	3.2 - 3.4
28/11/2028	0.5 - 0.6
06/02/2029	3.0 - 3.2
17/04/2029	1.0 - 1.2
26/06/2029	6.0 - 6.2
04/09/2029	1.6 - 1.8
13/11/2029	1.6 - 1.8
22/01/2030	3.8 - 4.0

Table 3.1: Critical amplitude of the short-period orbit for 10 different planetary configurations. The initial phase has been set to 65.64°.

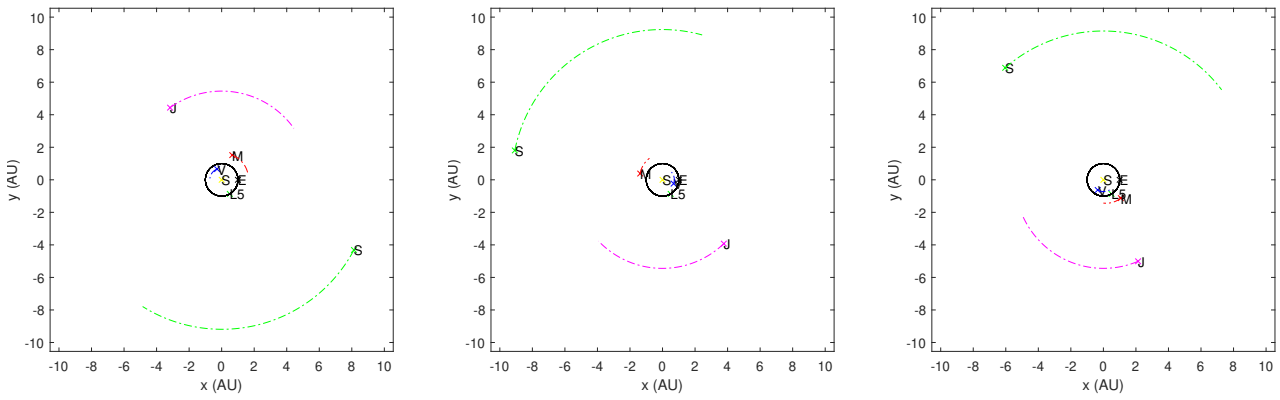

Figure 3.10: Planetary configuration in the Earth's rotating frame for 28 November 2028 (left), 2 May 2028 (middle) and 26 June 2029 (right). The planet positions are shown for the first 100 days of propagation.

3.2 Trojan-like trajectory

3.2.1 Modelling of asteroid orbits

In subsection 3.1.2, we have seen that the magnitude of the long-period drift depends on the amplitude of the motion around L5. In the previous section, we limited ourselves to close confined orbits around L5 in the interest of observing the Sun from a fixed position. This will be useful in terms of communication but also mandatory to continuously monitor the surface of the Sun. If we increase the initial velocity and thus the energy of the spacecraft, we can explore regions further away from L5. The magnitude of the long-period drift then becomes larger than the amplitude of the orbit. There exist two types of orbits that could be reached: tadpole orbits, which stay around L5 and horseshoe orbits that go through L3 and approach the Earth from L4. Both can be visualized in the Earth's rotating frame in Figure 3.11 and a closer view in Figure 3.12. These orbits are similar to those of Jupiter's Trojan asteroids, located at the triangular points of the Sun-Jupiter system. Tadpole and horseshoe orbits are of particular interest when considering the end of life of the spacecraft. Indeed, these orbits are suitable to preserve L5 from any contamination, the latter being an important issue regarding the linear stability of the triangular Lagrangian points. Furthermore, if another spacecraft is dedicated to orbit around L5, the probability of collision in the zone around that point will be very low and even null during the operational period of the second satellite.

If we take a look at the close view of the tadpole orbit drawn in Figure 3.12, we distinguish the short-period motion that oscillates around L5 due to the long-period component. In fact, the latter is a degenerated case of the more general behaviour sketched in Figure 3.13 (*Marzari et al, 2002*). When the long-period component has a width extent close to the amplitude of the short-period component, both combine to produce a complicated path as the one shown on the right side of Figure 3.13. However, this happens when the mass ratio of the two central masses is high enough. Indeed, from expressions (3.1) to (3.4), the ratio of the semi-major and semi-minor axes for the elongated long-period ellipse is $\sqrt{3\,\epsilon}$ ($\epsilon \approx \frac{m_2}{m_1}$ for small mass ratios) while that for the epicyclic short-period ellipse is 1/2. Therefore, in the case of the Sun-Earth system, ϵ is very small ($\epsilon = 3.0045\,10^{-6}$) and the long-period motion is in a quasi-rectilinear trajectory. The global motion then results in a periodic shift of the short-period orbit along the Earth's orbital path.

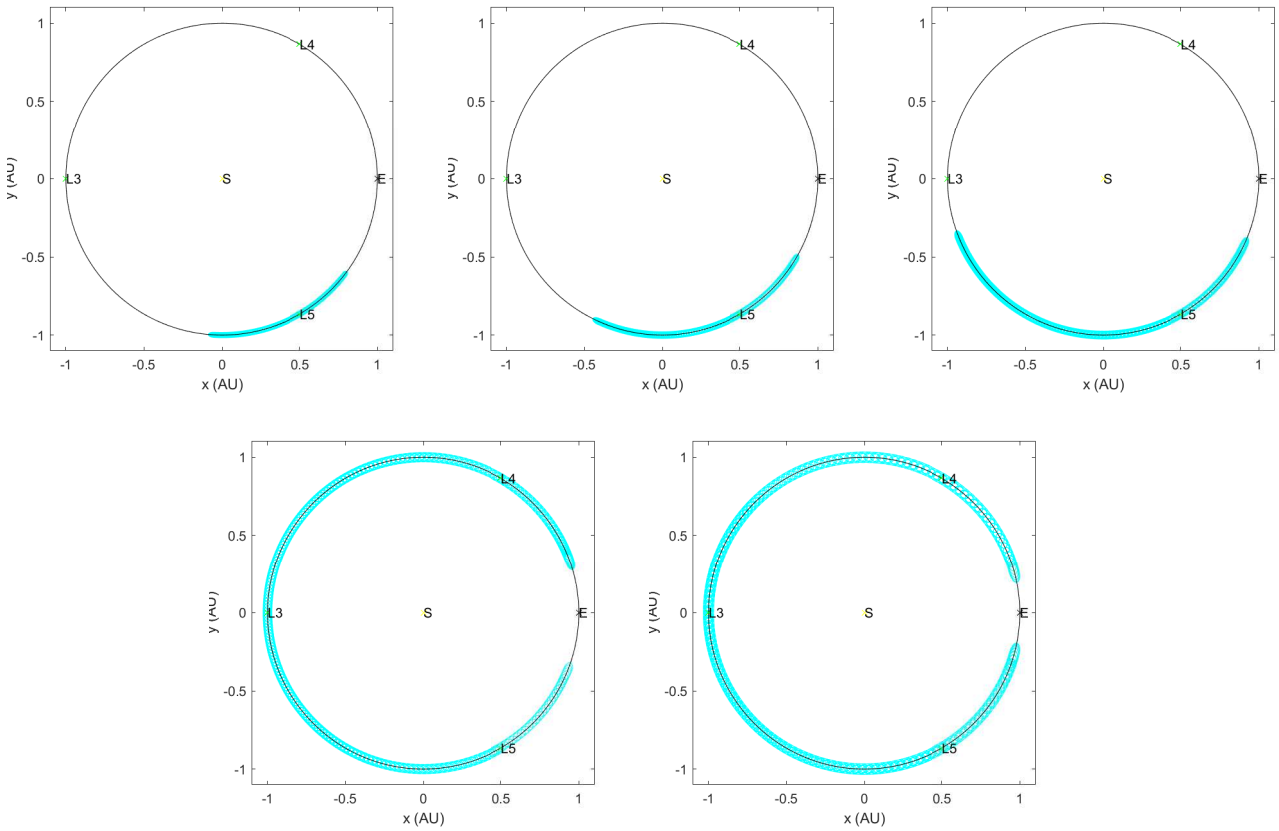

Figure 3.11: 2D Tadpole and horseshoe orbits in the Earth's rotating frame. The propagation starts on 22 January 2020 in the vicinity of L5 and ends on 22 January 2420. The initial orbital phase has been set to 0°. The amplitude of the initial orbit is $5\,10^6$ (top left), $6\,10^6$ (top middle), $7\,10^6$ (top right), $8\,10^6$ (bottom left) and $9\,10^6$ (bottom right) km.

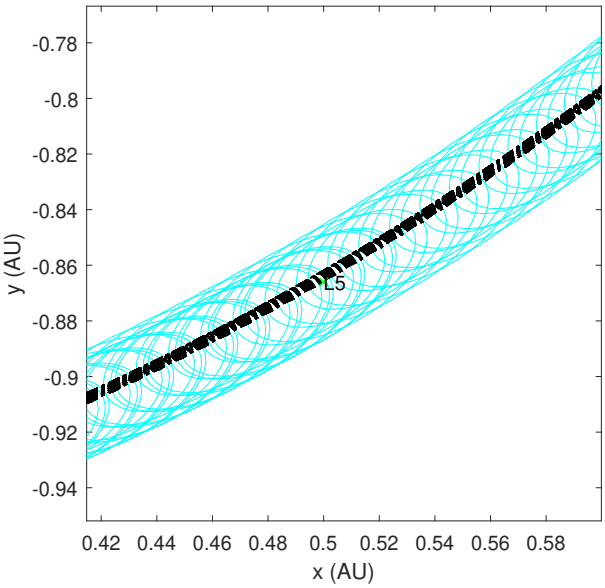

Figure 3.12: Close view of a tadpole orbit (cyan) in the Earth's rotating frame. The propagation starts on 22 January 2020 in the vicinity of L5 and ends on 22 January 2420. The initial orbital phase has been set to 0° and the amplitude is $5\,10^6$ km. The black line is the simulated circular orbit of the Earth around the Sun.

Figure 3.13: Example of tadpole orbit around the L5 point for a three-body system with a mass ratio of 0.1. **(Left)** The dynamics around that point is driven by two components: a long-period motion (elongated ellipse) about the equilibrium point combined with a short-period motion (small ellipse). **(Right)** The resulting global path about L5. Adapted from *Marzari et al. (2002)* and *Murray and Dermott (1999)*.

3.2.2 Use as disposal orbits

As tadpole and horseshoe orbits would be advantageous as graveyard orbits, we can evaluate if these Trojan-like trajectories are reachable assuming a reasonable delta-V manoeuvre. For this, we take the initial state referring to expressions (3.3) and (3.4), add a variable delta-V boost[4] in the tangential direction and propagate the obtained state for 250 years. The location of the manoeuvre takes place at an orbital phase of either 0, 30, 60 or 90 degrees while the delta-V magnitude is set to 50, 40, 30, 20, 10 or $5\,m/s$. We consider both operational orbits of $5\,10^5$ and 10^6 km amplitude. The propagation step is set to 10 days for all the above cases, taking into account a circular orbit for the Earth and the ephemeris of the 4 perturbing planets. To establish what kind of orbit is reached for each case, we define the angular distance as the maximum angle made by the spacecraft with the Sun and the initial L5 position during the 250 years propagation. Horseshoe orbits are then defined as those for which the angular distance is greater than 120°, or equivalently those that go beyond L3. Table 3.2 gathers the results obtained for both initial amplitudes.

Note the discrepancy in term of angular distance for a zero orbital phase. The latter is probably due to the extent of the initial orbit in itself, the results being nearly identical in the other cases. The first conclusion that can be drawn is that a horseshoe orbit is reachable with a minimum delta-V boost within $40 - 50$ m/s. The second point concerns the location of the manoeuvre, which is crucial to leave the L5 region. Carrying the propagation for an orbital phase of 180 and 270 degrees reveals that the most efficient delta-V kick takes place at the edges of the semi-minor

[4]We assume here that the full delta-V is provided by an instantaneous thrust impulse rather than via continuous thrust produced by an ionic engine.

Orbital phase (°)	**Delta-V (m/s)**	**Ang. Dist. (°)**	**Ang. Dist. (°)**
		$5\,10^5$ **km**	10^6 **km**
0	5	0.47	1.46
	10	0.48	1.46
	20	0.51	1.46
	30	0.56	1.47
	40	0.61	1.48
	50	0.67	1.51
30	5	3.69	4.47
	10	7.17	7.97
	20	14.66	15.52
	30	22.97	23.89
	40	32.27	33.26
	50	42.85	43.94
60	5	6.05	6.34
	10	12.40	12.70
	20	26.94	27.28
	30	44.86	45.26
	40	69.16	69.69
	50	145.25	147.82
90	5	6.91	6.94
	10	14.39	14.41
	20	31.94	31.95
	30	54.84	54.83
	40	93.45	93.26
	50	280.32	280.49

Table 3.2: Angular distance for both operational orbits of $5\,10^5$ and 10^6 km amplitude in the case of a tangential delta-V manoeuvre of either 5, 10, 20, 30, 40 or 50 m/s. The delta-V kick takes place either at 0, 30, 60 or 90 degree orbital phase. The propagation starts on 22 January 2020 and ends on 22 January 2270.

axis of the initial elliptic orbit (i.e. at an orbital phase of 90 and 270 degrees). In other words, a velocity change will be less costly closer to L5. Finally, we can adapt the magnitude of the delta-V boost in order to reach the desired disposal tadpole orbit or even a horseshoe path.

These values can be compared to delta-V needs for a typical spacecraft in different scenarios.

Table 3.3 gathers the disposal requirements for a series of common cases. The delta-V manoeuvre necessary to enter into a horseshoe orbit seems acceptable in view of these results.

Operational orbit	**Disposal scenario**	**Delta-V (m/s)**
Circular low-Earth orbit at 500 km altitude	Re-entry with a confined impact region of few hundred km^2	≥ 110 [17]
Circular medium-Earth orbit at 2000 km altitude	Re-entry with a confined impact region of few hundred km^2	≥ 450 [17]
High-Earth orbit (639 x 153000 km) of INTEGRAL	Re-entry with a perigee below 50 km	$27 - 73$ [18]
Lissajous orbit around L2 (Herschel)	Heliocentric graveyard orbit	≈ 120 [19]
Halo orbit around L1 (SOHO)	Re-entry in Earth's atmosphere	≤ 80 [20]
Halo orbit around L1 (SOHO)	Heliocentric graveyard orbit	≥ 47 [20]
Lissajous orbit around L2 (GAIA)	Re-entry in Earth's atmosphere	≈ 49 [20]

Table 3.3: Disposal delta-V cost for some typical satellite missions.

One could also try to evaluate the delta-V burst that would be needed to escape from a horseshoe orbit and in fine to re-enter the Earth's atmosphere. For this, we increase the delta-V magnitude until the two ends of the horseshoe join each other in the vicinity of the Earth. As Table 3.2 indicates, the delta-V applied will give the same results for both selected orbits and we are free to choose only one of them. Figure 3.14 shows the trajectories obtained for a boost of 100, 133, 166 and 200 meters per second. The delta-V required to leave the horseshoe orbit is found between 166 and 200 meters per second. This represents a costly manoeuvre compared to the existing plans for de-orbiting a spacecraft listed in Table 3.3. Furthermore, the latter does not take into account the final approach towards the Earth and a somehow controlled re-entry, which once again increase the total delta-V cost. Another option would be to crash the spacecraft on the far-side of the Moon, where no region is currently protected, to annul the cost of a controlled re-entry. However, we have also to keep in mind the timescale needed to reach the Earth. If the tangential delta-V manoeuvre takes place at a 90° orbital phase, the spacecraft will approach the Earth from L4, travelling a 300° true anomaly around the Sun. For a boost of 200 m/s, this will take about 43 years. After this period, during which the spacecraft was turned off, the operation team still has to re-activate it to perform the final disposal manoeuvre. The latter phase would be hard to achieve because of this prolonged period of inactivity. A similar attempt to switch on a space mission has already been tested for the ISEE-3 probe. Launched in 1978, the mission is injected into a heliocentric orbit similar to those drawn in Figure 3.14 in 1982 and flew over the Giacobini-Zinner comet in 1985 and the Halley comet

in 1986 (*Balint S, 2014*). In 2014, the spacecraft came in the vicinity of the Earth 28 years after its last measurements. Communicating with ISEE-3 was challenging since the hardware no longer existed and the command codes were lost (*NASA website, ISEE-3 Reboot Project*). When the control team succeeded to contact ISEE-3, attempts to put it into a high-Earth orbit failed because of a loss of nitrogen pressurant needed to fire its rocket engines. The timescale between the last operation and the final manoeuvre is therefore crucial in terms of reliability. Performing the 200 m/s delta-V boost at a 270° orbital phase allows to reach the Earth directly from L5 in less than 9 years. Even if this amount of time is much less than the previous 43 years, this solution seems to be highly compromised in view of the potential technical problems. We can obviously play with the magnitude of the manoeuvre to shorten the return phase (6 years with 300 m/s, 4 years with 500 m/s, etc.), but this increases the amount of fuel needed for disposal and in turn the cost of the mission. In the end, tadpole or horseshoe trajectories would still be the best fuel-saving options and most reliable solutions as graveyard orbits.

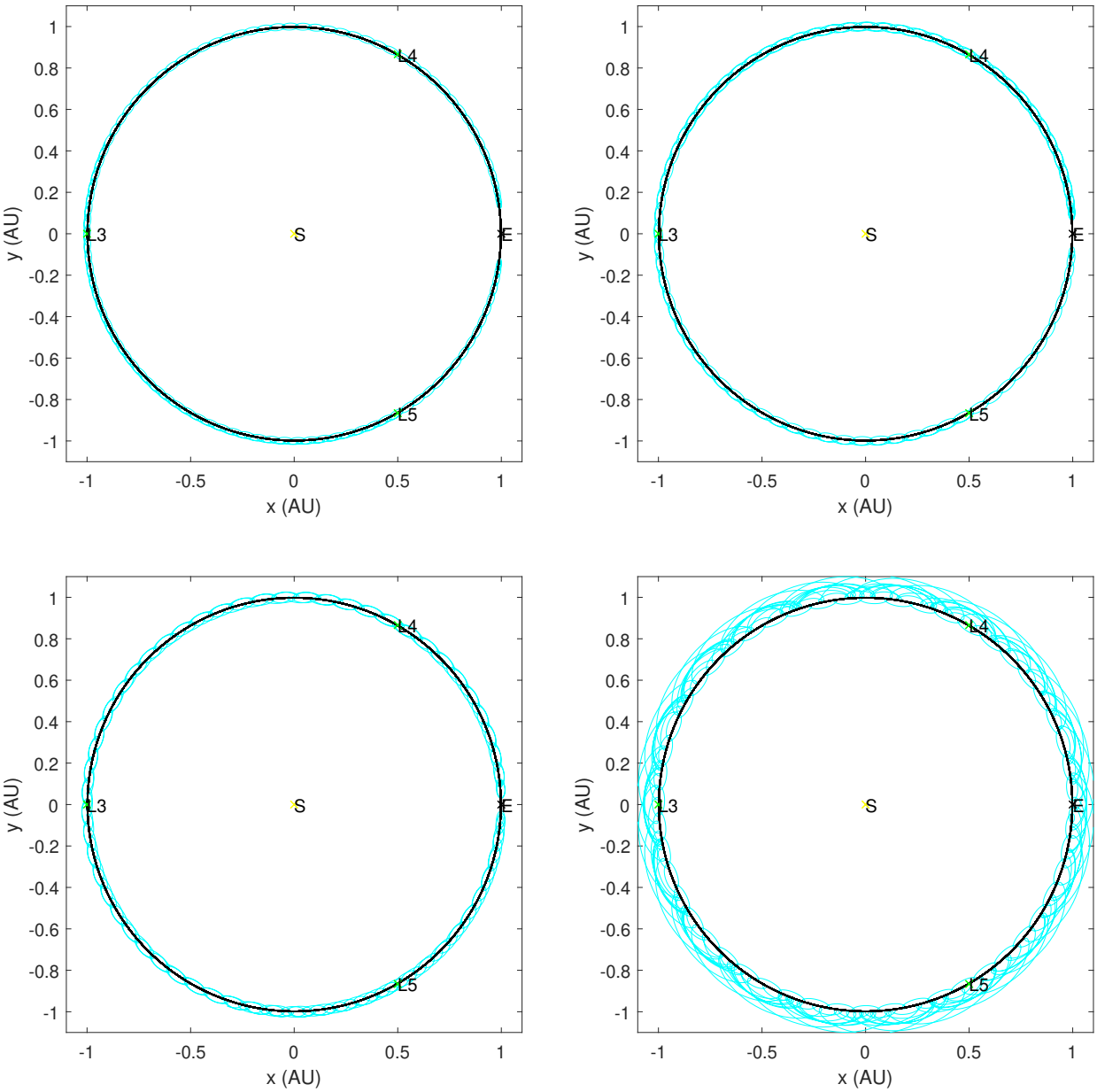

Figure 3.14: Trajectories obtained after a delta-V kick of 100 (top left), 133 (top right), 166 (bottom left) and 200 (bottom right) meters per second. The initial amplitude of the orbit is 10^6 km and the manoeuvre takes place at 90° orbital phase. The propagation starts on 22 January 2020 and ends on 22 January 2270.

Chapter 4

Operational orbit determination

This chapter and the following ones have been addressed as part of an internship that took place in the Mission Analysis Department of the European Space Operations Centre (ESOC), the ESA facility responsible for all operational aspects of a space mission. This was a unique opportunity to use high precision tools and state-of-the-art softwares. In the forthcoming parts, I used ORBSW (ORBit SoftWare) and its extension MASW (Mission Analysis SoftWare). ORBSW is a $C++11$ software developed for performing orbit related computations and manoeuvre optimisation. It includes libraries for numerical integration, ephemeris handling, reference frame manipulation, observation modelling, optimisation, et cetera. As $C++11$ is a complex language, ESA has developed a Python interface to ORBSW using *pybind11*, a library that exposes $C++$ types in Python and vice-versa. In turn, MASW is an extension of ORBSW that makes use of its libraries to build tools and applications which are of specific use for mission analysis. The user is then free to use these libraries to compose their own scripts and programs to solve a specific problem. Python is thus the programming language for the rest of the work and Visual Studio Code is the code editor used to handle it.

The present chapter is devoted to the determination of stable closed orbits around L5. Many effects and constraints have been taken into account to achieve the most rigorous and faithful results. The end-up product is a tool that finds a closed orbit around L5, starting in the vicinity of the latter.

4.1 Propagation with MASW

To introduce the concepts and libraries used in the following of the work, let us start with a simple propagation in the Solar system. The planetary ephemeris are taken from the *de435.bsp* file, available for downloading on the NASA's Navigation and Ancillary Information Facility (NAIF) website managed by the Jet Propulsion Laboratory. The ephemeris are available from 31 December 1549 to 25 January 2650. I also used the *gm_de*431.*tpc* constant file that gathered

the GM (gravitational constant times mass) values for the Sun, planets, planetary system barycenters, and selected satellites, like the Moon. The latter file will be useful when carrying out the propagation. Note that we compute the position of L5 from the ephemeris of the Earth only, applying a simple 60° clockwise rotation. The other planets have a rather low impact on the position of the triangular points and a careful verification (completed by Gabor Varga, a mission analyst at ESOC) shows that their positions differ by less than 1 km from the more complete NASA SPICE ephemeris files.

Then, once we have included all planets (from Mercury to Pluto included) in our propagator, we add the solar radiation pressure (SRP) effect. The model implemented inside MASW is called the flat plate model. Without entering into details, the perturbing acceleration due to SRP (for a satellite with large solar panels) can be summarized as (*Montenbruck & Gill, 2000*):

$$\ddot{\mathbf{r}} = -P_{Sun}\, C_r\, \frac{A}{m}\, \frac{\mathbf{r}_{Sun}}{r_{Sun}^3}\, AU^2 \tag{4.1}$$

where $P_{Sun} = 4.56\,10^{-6}\ N/m^2$ is the solar radiation pressure experienced at 1 AU from the Sun, C_r is the radiation pressure coefficient (given by $C_r = 1+\epsilon$ with ϵ being the reflectivity coefficient of the exposed surface), A is the area subjected to SRP, m is the mass of the spacecraft, $\mathbf{r}_{Sun}$ is the position vector of the Sun measured from the spacecraft to the Sun (r_{Sun} being its norm) and AU is the astronomical unit. The C_r coefficient can take values from 0 (transparent medium) to 2 (perfect specular reflector). Note that C_r is equal to 1 for perfectly absorbing surfaces (*Delgado M. R., 2008*).

To carry out a propagation, we therefore need to set the relevant parameters associated to SRP (namely A, m and C_r) and give the initial state as well as the starting and ending epoch. One point that has to be raised is the slight difference in the definition of the rotating frame attached to L5. In opposition to Figure 3.1, the X axis is directed along the line joining L5 to the Sun and the Y axis is defined as making a 90° anti-clockwise angle with the latter. The Z axis completes the right-handed coordinate system. All in all, the present system is turned by a 90° anti-clockwise rotation compared to the one described in Chapter 3. A planar view of the new rotating frame is seen in Figure 4.1.

In such a frame, expressions (3.3) and (3.4) are rewritten as:

$$\delta x' = \frac{X_{sp}}{2}\, sin\left[\left(1 - \frac{27\epsilon}{8}\right) n_3\, t + \phi_{sp}\right] \tag{4.2}$$

$$\delta y' = X_{sp}\, cos\left[\left(1 - \frac{27\epsilon}{8}\right) n_3\, t + \phi_{sp}\right] \tag{4.3}$$

and the initial conditions (3.9) to (3.12) are adapted to:

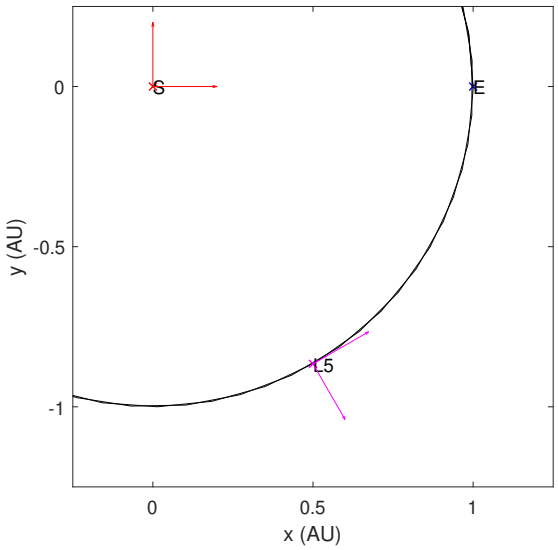

Figure 4.1: New co-rotating frame attached to L5 (magenta) and Earth's rotating frame (red). The black line represents a circle of 1 AU radius centered on the Sun.

$$\delta x' = \frac{X_{sp}}{2}\, sin(\phi_{sp}) \tag{4.4}$$

$$\delta y' = X_{sp}\, cos(\phi_{sp}) \tag{4.5}$$

$$\frac{\delta x'}{\delta t} = \frac{X_{sp}}{2}\left(1 - \frac{27\epsilon}{8}\right) n_3\, cos(\phi_{sp}) \tag{4.6}$$

$$\frac{\delta y'}{\delta t} = -\, X_{sp}\left(1 - \frac{27\epsilon}{8}\right) n_3\, sin(\phi_{sp}) \tag{4.7}$$

As a preamble to future results, we propagate the initial conditions (4.4) to (4.7) set with $X_{sp} = 10^6$ km and $\phi_{sp} = 90°$ from 22 January 2020 to 22 January 2040. The relative and absolute tolerances have both been set to 10^{-12}. Note that the z component of the velocity is arbitrary set to zero since no restriction is imposed by the circular restricted three-body problem (CRTBP) solution. The mass m of the spacecraft is fixed to 1000 kg while the area A facing the Sun is considered constant and equal to 10 m^2. The Lagrange spacecraft being still in development, the purpose is rather to have a faithful order of magnitude for the mass and area of the latter. The radiation pressure coefficient C_r is arbitrary set to 1.5. The results obtained are shown in Figure 4.2 both in the Sun and L5 centered Earth's rotating frames.

Compared to what has been done in the previous chapter, the Earth's orbital eccentricity is easily seen both in the motion of the Earth and L5. Indeed, in the rotating frame, the Earth approaches and moves away from the Sun-Earth barycenter with a period of one year, impacting the definition of all Lagrangian points. The L5 point therefore follows an orbital track directed towards the center of mass of the Sun-Earth system (see the black line in Figure 4.2). Another

remark that can be raised is the very small amplitude of the motion along the Z axis. Except for the periodic perturbations that come from the other planets, the motion is quasi-planar. Note also the synchronous motion of the spacecraft around L5. As the period of the orbit is also 1 year, the satellite follows the triangular point on its linear path. From the stability point of view, we qualitatively achieve the same drift as in earlier computations, this time with a much higher magnitude. However, no conclusion can be immediately drawn on the origin of that drift. Many effects can be responsible of such a drift, namely the SRP, the perturbing planets, the initial state and also the eccentricity of the Earth's orbit.

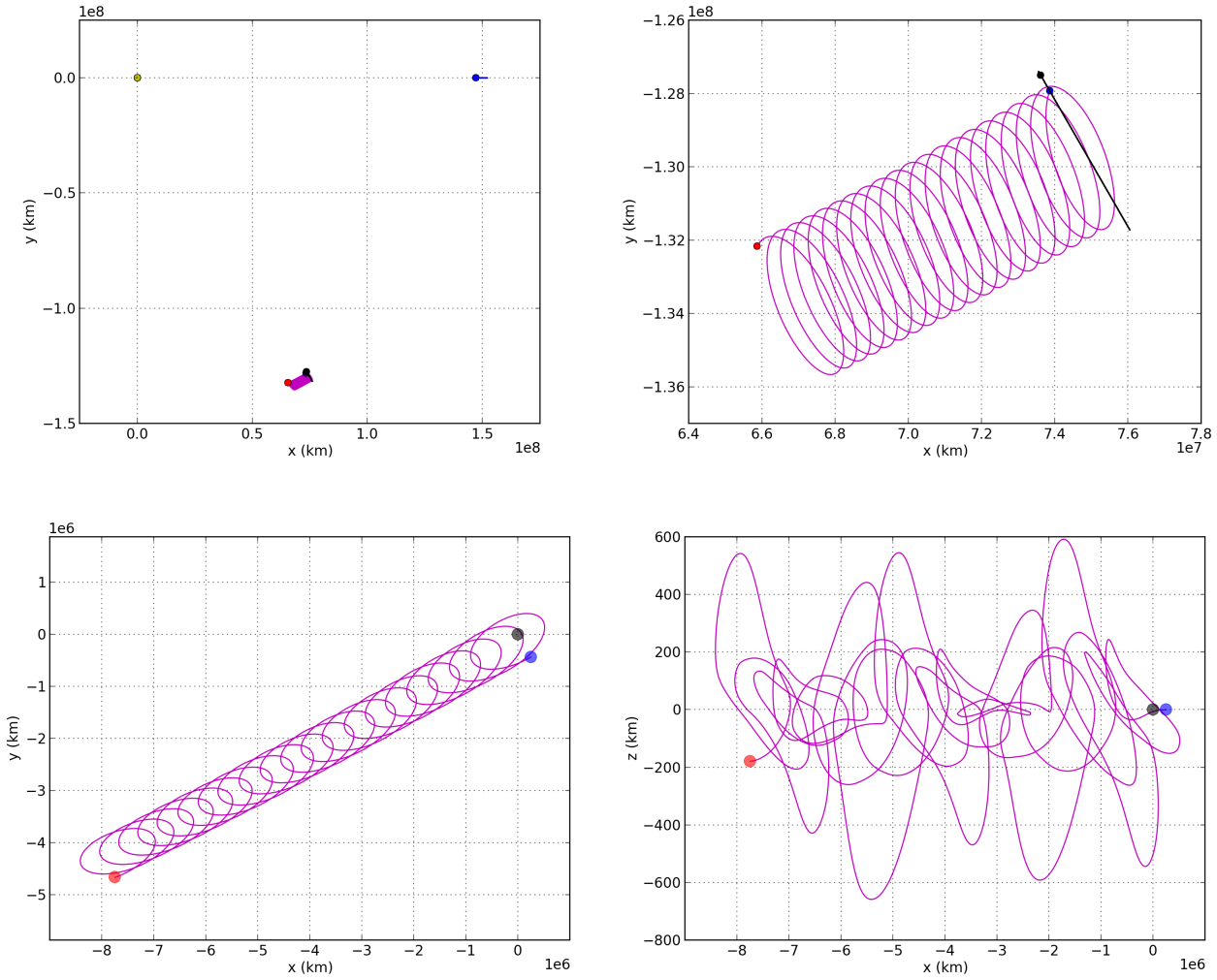

Figure 4.2: Obtained trajectories (magenta) after a propagation with the ESA MASW software. The orbit is shown in the Earth's rotating frame centered either on the Sun (top) or on L5 (bottom). The Sun centered representation is presented both in the global Solar system (top left) and around L5 (top right) and projected in the ecliptic plane. The L5 centered orbits are shown in the ecliptic plane (bottom left) and a x-z view is also proposed (bottom right). The initial amplitude of the orbit is 10^6 km and the orbital phase is set to 90°. The propagation starts on 22 January 2020 and ends on 22 January 2040. The blue (black) dot and the blue (black) path in the upper left panel represent respectively the Earth (L5) initial position and whole path. The red and blue dots near L5 show the final and initial position of the spacecraft.

From the results of Chapter 3, we learn that the effect of the other planets has a much lower impact on the magnitude of the drift. This is confirmed when we turn off Jupiter and Venus since the same behavior is observed. The effect of the SRP is investigated in Figure 4.3. As we can see, the final position is only slightly modified and the SRP is not the major contributor of the drift observed. As regards to the initial state, Figure 4.4 shows the effect of the latter. The orbital phase effectively influences the amplitude of the orbital drift, but also the direction. On the contrary, carrying out a propagation with a different initial amplitude only affects the magnitude of the orbital drift. As already said in the previous chapter, the lower the amplitude, the better is the linear solution and the lower is the drift away from L5. The final effect, and probably the most interesting one, is the consequence of the eccentricity of the Earth's orbit. To assess this effect, we start the propagation at diverse dates throughout the year (see Figure 4.5). The Earth's initial distance to the Sun therefore varies and the solution of the circular restricted three body problem (namely expressions (4.2) and (4.3)) is no more valid. Instead, that result is the mean solution of the elliptic three body problem. When the Earth is exactly at 1 AU from the Sun (which will occur around the beginning of April in 2020 (*Espenak F., 2016*)), the CRTBP solution then holds again and we can find quite stable trajectories around that date. An example of what can be obtained by customizing the starting date is shown in Figure 4.6. The initial state and SRP still play a role in the dynamics and slightly perturb the optimal date.

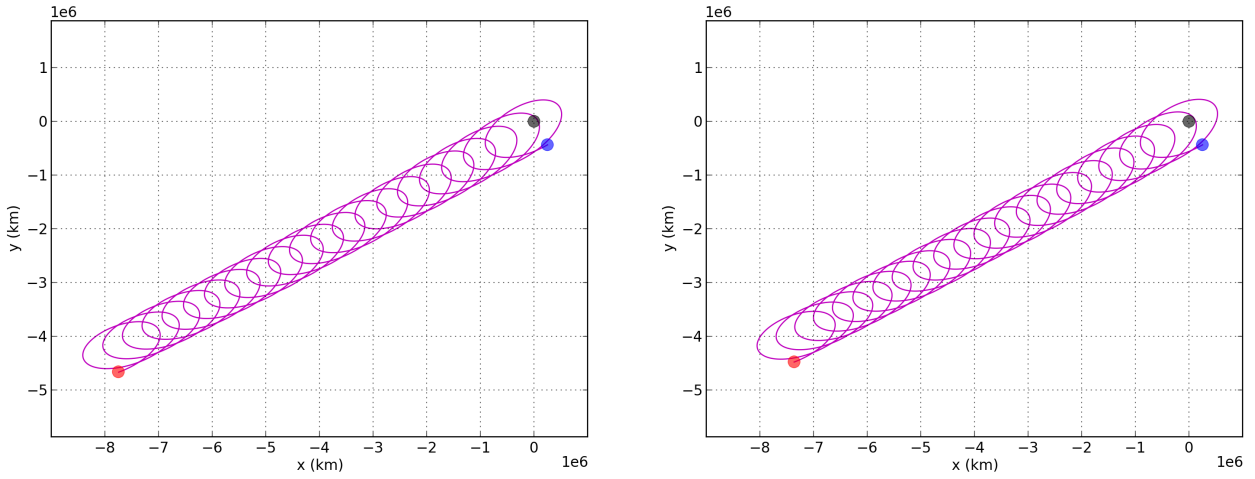

Figure 4.3: Comparison of the trajectories (magenta) acquired with (left) and without (right) solar radiation pressure. The orbit is shown in the Earth's rotating frame centered on L5 and projected in the ecliptic plane. The initial amplitude of the orbit is 10^6 km and the orbital phase is set to 90°. The propagation starts on 22 January 2020 and ends on 22 January 2040. The black dot represents L5 while the blue and red dots stand for the initial and final positions of the spacecraft.

As a result of the numerous perturbations that our spacecraft will encounter, it will not correctly fulfil its observations of the Sun on a drifting orbit. In such cases, some yearly correction

manoeuvres will be needed and both the mass and mission cost will rise. Also, we would like to find low-cost stable orbits for any initial position in the vicinity of L5 and for any dates. It is therefore mandatory to design a tool that will find stable operational orbits around L5, at least for the lifetime of the mission. This is discussed in details in the next section.

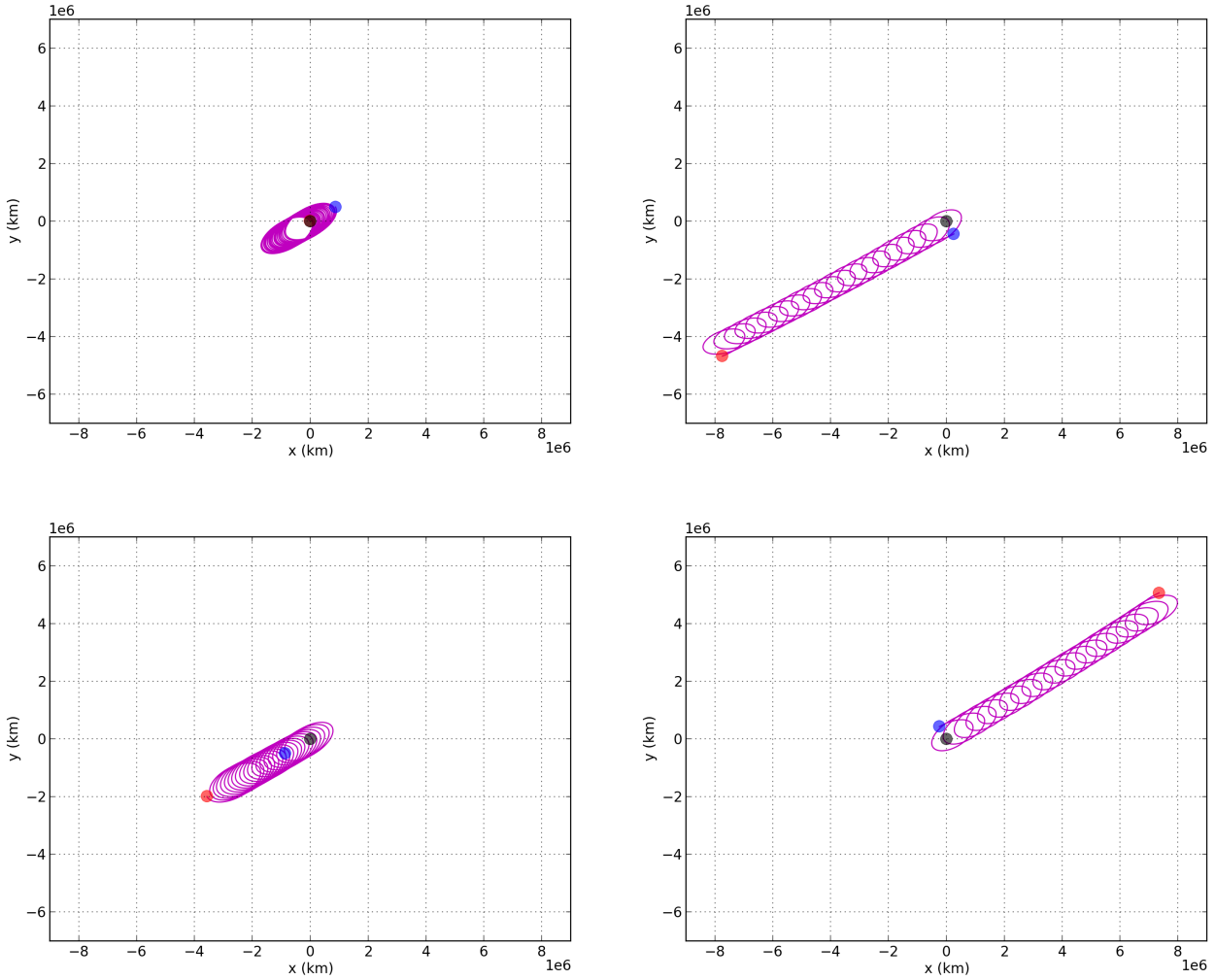

Figure 4.4: Comparison of the trajectories (magenta) obtained with an initial orbital phase of 0° (top left), 90° (top right), 180° (bottom left) and 270° (bottom right). Solar radiation pressure is taken into account with $C_r = 1.5$. The orbit is shown in the Earth's rotating frame centered on L5 and projected onto the ecliptic plane. The initial amplitude of the orbit is 10^6 km. The propagation starts on 22 January 2020 and ends on 22 January 2040. The black dot represents L5 while the blue and red dots stand for the initial and final positions of the spacecraft.

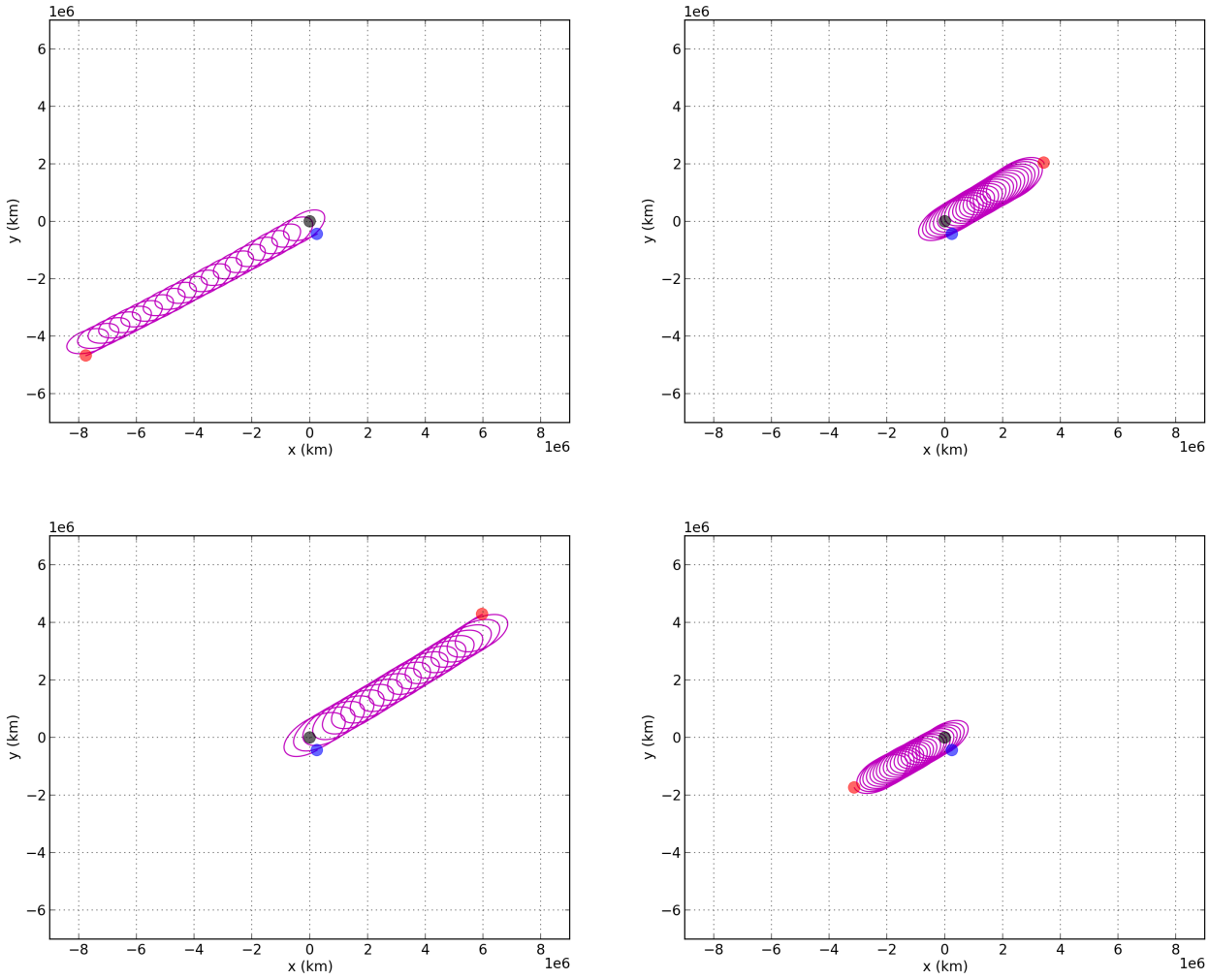

Figure 4.5: Comparison of the trajectories (magenta) collected for four different starting dates through the year 2020. The propagation is initiated on 22 January (top left), 22 April (top right), 22 July (bottom left) and 22 October (bottom right) and ends on 22 January 2040. Solar radiation pressure is taken into account with $C_r = 1.5$. The orbit is shown in the Earth's rotating frame centered on L5 and projected onto the ecliptic plane. The initial amplitude of the orbit is 10^6 km and the orbital phase is set to 90°. The black dot represents L5 while the blue and red dots stand for the initial and final positions of the spacecraft.

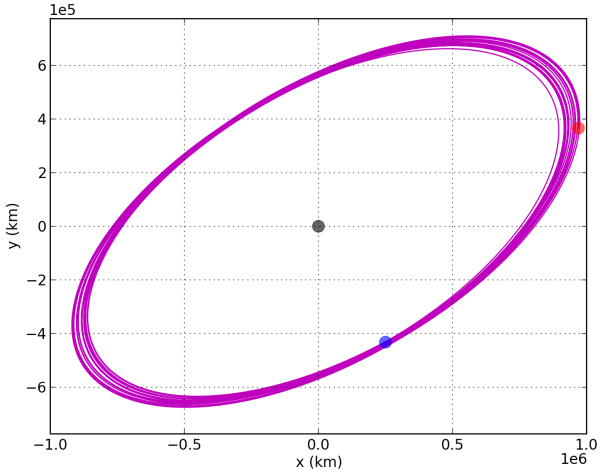

Figure 4.6: Trajectory of the spacecraft (magenta) over a 20 year propagation starting on 31 March 2020 and ending on 22 January 2040. Solar radiation pressure is taken into account with $C_r = 1.5$. The orbit is shown in the Earth's rotating frame centered on L5 and projected in the ecliptic plane. The initial amplitude of the orbit is 10^6 km and the orbital phase is set to 90°. The black dot represents L5 while the blue and red dots stand for the initial and final positions of the spacecraft.

4.2 Closed orbit optimization

As concluded in preceding section, the CRTBP short-period solution allows to find stable orbits around triangular Lagrangian points in very particular conditions in terms of initial state and orbit insertion date. However, mission design requires some flexibility in terms of development, building and launching windows. For this, we have to conceive a tool that will find close periodic orbits around L5 for any epoch of time. This will be addressed in the present section.

4.2.1 Theoretical background

The easiest way to proceed is to adapt the velocity of the spacecraft at some initial position in the vicinity of L5. Thus, we can basically enter a stable orbit from anywhere around L5. To determine the optimal solution related to a particular position, we will make use of optimization methods. Numerical nonlinear optimization constitutes a large area of applied mathematics which finds applications in engineering, economics and finance, computer science, geophysics, etc (*Roberts & Kochenderfer, 2014*). The basic concept of optimization is to find the best element satisfying a problem among a set of available alternatives. In the simplest case, a nonlinear optimization problem consists of minimizing or maximizing a nonlinear function of some variable by iteratively taking input values within an allowed set and evaluating the function until the minimum or maximum is met (*Roberts & Kochenderfer, 2014*). The input value that gives the extremum of the function is then called the optimal solution. The function to be minimized or maximized is often called the cost function and most of the time takes as input more than one parameter to optimize. Some applications often require to find the minimum of several functions of the same variables at the same time. This is often the case when engineers try to get the best performance at the lowest cost. These are known as multi-objective problems. The field of optimization is divided into two big families: constrained or unconstrained problems. Indeed, we can add some conditions that imperatively need to be fulfilled concurrently with minimizing the cost function. These conditions, which depend on the variables to be optimized, drive and constrain the search for the optimal solution. In that case, the problem is said to be constrained. Note that there exist two types of constraints, namely the equality and inequality constraints. The global framework for nonlinear optimization method can be sketched as follows (adapted from *Leyffer & Mahajan, 2010*).

Consider the problem :

$$Minimize\, f(x) \quad subject\, to \quad c(x) < 0 \quad with \quad l_b < x < u_b \tag{4.8}$$

where $c(x)$ is a constraint function, l_b and u_b respectively stand for the lower and upper bound of x. A simplified algorithm for solving it may be:

Given initial estimate $x_0 \in [l_b, u_b]$, set $k = 0$

while x_k is not optimal

do

Approximately solve and refine a local model of (4.8) around x_k

until An improved estimate x_k is found

set $k = k + 1$

end

The iterative search for the minimum/maximum point (i.e. what is inserted inside the **do** loop in the above scheme) is the bottom line of numerical optimization. Many algorithms have been proposed and implemented to solve either more general problems (*Leyffer & Mahajan, 2010*) as well as very specific field-related problems. The architecture of the searching process is most of the time designed according to the kind of problem that is targeted. Indeed, each algorithm has its own way of finding the next estimate and dealing with the constraints and bounds on the free parameters. Therefore, there exists an outstanding variety of algorithms and trying to describe all of them is pointless. Rather, we will explain hereafter which one has been selected to deal with our problem.

4.2.2 First implementation and algorithm selection

First of all, we need to set up the problem that will allow to find close periodic orbits around L5. Defining the problem means finding the right cost function, constraints and bounds in order to get a sufficiently close trajectory for a certain period of time. Moreover, some additional requirements are imposed by the mission design and our problem also needs to account for them. The Lagrange spacecraft will be dedicated to space weather monitoring by continuously observing the Sun from L5. Two angles state the quality of the observations: the Sun-Spacecraft-Earth (SSE) and the Earth-Sun-Spacecraft angles. Both can be seen in Figure 4.7. The SSE angle relates the pointing directions of the telescope (towards the Sun) and of the communication antennas (towards the Earth). Keeping the variation of this angle relatively small is therefore worthwhile to avoid complex pointing mechanisms. Indeed, it has been established that the SSE variation should be less than $\pm 0.3°$ around the nominal $60°$ encountered at L5. On the other hand, the ESS angle describes the position of the spacecraft in the Earth's frame. Small fluctuations of that angle means a constant viewpoint of the Sun, i.e. stable observations over time. It has been stated that the ESS angle cannot depart from more than $\pm 0.5°$ around the theoretical $60°$ met at L5. ESA has recently translated these limits into absolute distances from L5. Their conclusion is that the operational orbit of Lagrange cannot go beyond $1.5\,10^6$ km from the triangular point. That will therefore restrict the allowed amplitude for our search of

stable orbits. These angular constraints will be translated into inequality constraints and added to our problem.

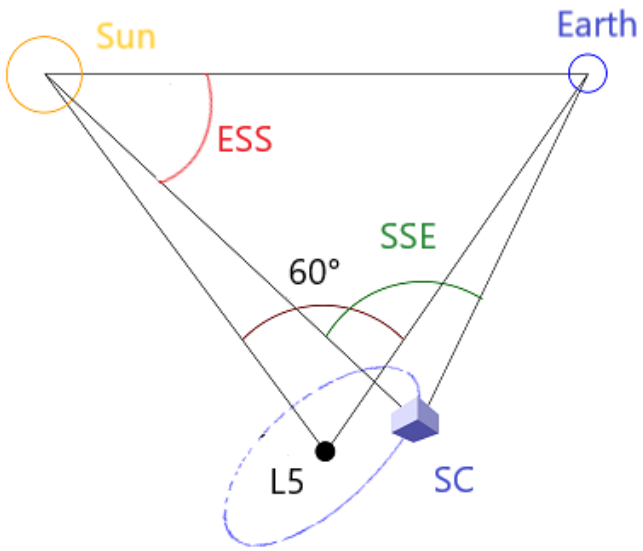

Figure 4.7: Definition of the Sun-Spacecraft-Earth (SSE) and Earth-Sun-Spacecraft (ESS) angles.

The generic problem of optimizing trajectories is that there exist countless ways to write the problem in the form of expression (4.8). In the following, I will not pretend that the solution found is the best way of formulating and solving the problem. Rather, I will present and discuss my own answer to the question.

The targeted orbit is an L5 centered close orbit with a given amplitude. Therefore, some constraints should restrain the center of the orbit in a close vicinity of L5 for a relatively long period of time. From ESA guidelines, the spacecraft should maintain this kind of orbit for at least 10 years, which corresponds to the targeted lifetime of the mission. It is also required that the variations in SSE and ESS angles must not exhibit any long-period drift. Even if the latter is sufficiently small to be compliant to a 10 year variation, it would eventually break the angular requirements at some time soon after the end of the mission. This addendum might allow Lagrange to pursue its observations even past the 10 year goal (as it has been the case for other solar observatories like SOHO). At this point, we have sufficient information to formulate the problem. The first statement of the problem is the following:

- **Cost function** : distance between initial and final positions
- **Constraints** :
  1. $60 - 0.3° \leq \text{SSE} \leq 60 + 0.3°$
  2. $60 - 0.5° \leq \text{ESS} \leq 60 + 0.5°$
  3. $60 - 0.01° \leq \text{mean}(\text{ SSE }) \leq 60 + 0.01°$

- **Variable to optimize** : 3 components of the velocity in the frame attached to L5
- **Init. guess** : Velocity associated to the CRTBP solution (4.6) and (4.7)
- **Bounds** : ± 10 m/s around the initial guess (for each component)
- **Epoch** : 21 June 2024 - 21 June 2034

The range of epoch was chosen to be strictly 10 years because of the period of short-period orbits which is very close to the year (see Section 3.1.1). Using this property, we can be assured that the spacecraft will be at the same position one year later if the orbit is closed. That explains the shape of the cost function. Another remark concerns the third constraint. It states that the mean of the SSE angle through the full propagation should be found in the interval $[60 - 0.01°, 60 + 0.01°]$. This is a way to force the orbit to be centered on L5 and to eliminate the long-period drift. Note that the z component of the initial velocity is set to zero but let as a free parameter for the optimizer. The upper and lower bounds on the velocity have been chosen symmetric with respect to the CRTBP solution and fixed to ± 10 m/s to minimize the total delta-V required. Finally, the initial epoch was arbitrary selected in the middle of the foreseen arrival year. Note that the two-sided inequality constraints have been written in one line in the above statement while, for implementation purposes, they will be transformed into two one-sided inequalities, as in expression (4.8). The reason is essentially due to the structure required by the different algorithms that will be used. They could still have been expressed in a more elegant way using absolute values but this is highly not recommended for the good convergence of the algorithm. All in all, we thus have 6 one-sided inequalities.

Now that we have our first implementation of the problem, we need to properly choose the algorithm that will try to find the optimized solution. As previously said, there are many algorithms and each has its own capabilities. We will thus limit ourselves to the ones that can deal with single-objective constrained problems, i.e. the class of our optimization problem. Another important feature of the selected algorithm will be its search field, referred as local or global. A global optimizer covers the whole range of possible values for your variables while a local optimizer stays in some neighbourhood around the initial guess (*Womersley R., 2008*). Global methods are therefore slower but guarantee to find the global minimum of your cost function for a given range of your variable. This approach is very useful when we have no a priori idea of the optimal solution. In our case, the CRTBP solution will be taken as a quite good initial guess and hence local optimization is adopted for the sake of saving time.

As we are working in Python, we will make use of the available optimization-dedicated library available called PyGMO. The latter is a scientific library designed to handle and solve all kinds of stochastic, deterministic and optimization problems. It contains a lot of algorithms as

well as many well-known mathematical problems and provides an interface to construct and solve user-defined problems. PyGMO is therefore well adapted to our purpose. From PyGMO documentation [30], the algorithms are ranked following the kind of problems they can deal with. We then select the local algorithms that solve single-objective constrained problems. In the following, we will consider some of them and keep the best one regarding two criteria: the quality of the final orbit and the time taken to reach it.

Compass search, COBYLA (Constrained Optimization BY Linear Approximations), MMA (Method of Moving Asymptotes) and CCSA (Conservative Convex Separable Approximation) are the four pre-selected algorithms. At this stage, they will be used as black-boxes and compared to keep the most efficient one. We have fixed the absolute tolerance of the cost function to be 1000 km. This means that when the cost function varies by less than 1000 km between two steps, the optimization is considered to be sufficiently accurate and the solver is stopped. Indeed, even for a relatively small orbit of 100000 km amplitude (compared to past missions in orbit around L1 and L2), this tolerance is still two orders of magnitude lower. Table 4.1 shows the working time and the end value of the cost function, i.e. the distance between the initial and final positions of the spacecraft, for a 10^6 km semi-major axis orbit. The optimized trajectory found by each solver is shown in Figure 4.8. Note that the SRP coefficient is set to 1.0 to average the value obtained from several studies (*Gobinddass & Willis, 2008* and *Zelensky et al., 2011*) that estimate the latter in the range $[0.9, 1.1]$ for satellites with various shapes.

Algorithm	**End value of the cost function (km)**	**Running time (s)**
COBYLA	2886	231
MMA	2986	1231
Compass Search	51261	575
CCSA	42800	1254

Table 4.1: Comparison of the 4 algorithms used to optimize a closed trajectory around L5.

As we can see, three solvers stand out in terms of final orbit generated. However, the discrepancy comes from the time they need to find the optimal solution. COBYLA seems to be the most efficient algorithm for this kind of problem and will be selected for further improvement. The algorithm was invented by Michael J. D. Powell, a British mathematician, while working for *Westland Helicopters*. In opposition to most of the non-linear optimization algorithms, COBYLA is a gradient-free method, i.e. an algorithm that does not rely on the derivatives of the objective function to find the minimum of the latter. The idea is rather to approximate both the constraints and the cost function in a linear way and solve the resulting problem at each step. The whole problem described earlier is far from being linear since the defined angles as well as the cost function are not linear functions of the initial velocity. Such kind of optimization

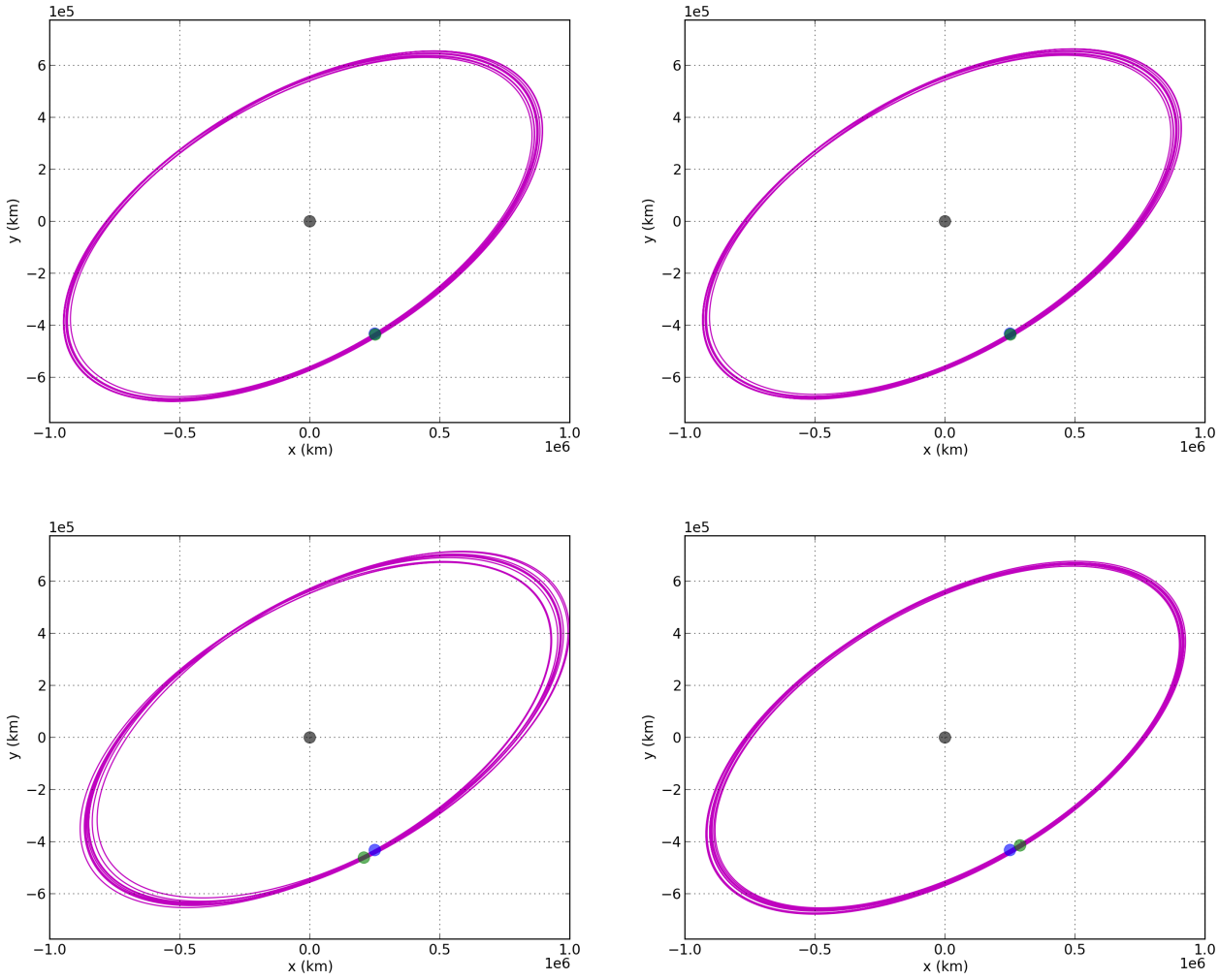

Figure 4.8: Comparison of the trajectories (magenta) optimized with different algorithms in the Earth's rotating frame and centered on L5. The COBYLA (top left), MMA (top right), Compass search (bottom left) and CCSA (bottom right) are used. Solar radiation pressure is taken into account with $C_r = 1.0$. The amplitude of the orbit is 10^6 km and the initial orbital phase is 90°. The propagation starts on 21 June 2024 and ends on 21 June 2034. The black dot represents L5 while the blue and green dots stand for the initial and final positions of the spacecraft.

is more challenging to solve. COBYLA thus transforms the problem into a simpler problem by linearizing it. The goodness of the obtained solution is then evaluated using the initial constraints and cost function and this information is used to refine the quality of the linear approximation for the next iteration of the algorithm (*Powell, M.J., 1994*). The optimization stops when the solution cannot be improved anymore or when a user-defined criteria is met. Compass search is also a derivative-free algorithm but much less efficient than COBYLA as it consists in a direct dichotomic search. In other words, starting from an initial guess and a initial step size, the algorithm progresses by halving the step size until the minimum of the cost function is found (*Burkardt J., 2012*). The MMA algorithm is in essence very similar to COBYLA since an approximated problem is generated and solved at each step. However,

MMA relies on gradient evaluations as well as on information from previous iteration points to create these sub-problems (*Svanberg K., 1998*). This could slow down the whole optimization process. MMA is in fact a particular implementation of CCSA, constructing more complex approximations than the latter (*Svanberg K., 2002*). Even if their behaviors are quite similar for most problems, this could explain why MMA gives slightly better results for our problem.

Solving the problem as it is currently formulated does not yield a non-drifting orbit. In Figure 4.9 the results obtained with COBYLA show that both ESS and SSE angles are slowly drifting and the orbit is not exactly centered on L5. To overcome both problems, we should tighten the constraints on the mean of SSE to a value lower than 0.01° and add the same requirements for the ESS angle. We therefore decided to lower them to 0.001°. Also, it would be useful to choose in advance the inclination of the orbit with respect to the ecliptic plane. This will be particularly interesting to mitigate the delta-V cost of the insertion manoeuvre if the spacecraft arrives with some inclination with respect to the ecliptic plane. As the z component of the orbit is totally decoupled from the x-y motion, we only have to enlarge the bounds of the velocity along that direction while adding a constraint stating some boundaries on the inclination. However, the latter should be comprised between 90 and 270 degrees because the libration orbit is defined as a clockwise motion as seen from the ecliptic north pole. As a reminder, the inclination of an orbit with respect to a particular frame can be obtained via the expression (*Kerschen G., 2018*):

$$i = acos\left(\frac{(\mathbf{r} \otimes \mathbf{v})[3]}{||\mathbf{r} \otimes \mathbf{v}||}\right) \tag{4.9}$$

where $(\mathbf{r} \otimes \mathbf{v})[3]$ is the third component of the vector product between the position $\mathbf{r}$ and the velocity $\mathbf{v}$ of the spacecraft. This expression is valid only if both vectors are written in that frame. The final problem statement is therefore:

- **Cost function** : distance between initial and final positions
- **Constraints** :
  1. $60 - 0.3° \leq \text{SSE} \leq 60 + 0.3°$
  2. $60 - 0.5° \leq \text{ESS} \leq 60 + 0.5°$
  3. $60 - 0.001° \leq \text{mean(SSE)} \leq 60 + 0.001°$
  4. $60 - 0.001° \leq \text{mean(ESS)} \leq 60 + 0.001°$
  5. $X - 1.0° \leq \text{inclination} \leq X + 1.0°$
- **Variable to optimize** : 3 components of the velocity in the frame attached to L5
- **Init. guess** : Velocity associated to the CRTBP solution (4.6) and (4.7)
- **Bounds** : ±10 m/s around x and y velocity component, ±200 m/s for the z component.

- **Epoch** : 21 June 2024 - 21 June 2034

where X stands for the inclination defined by the user. The bounds on the related constraints have been set to $\pm 1.0°$, which is not much restrictive, because we do not want them to drive the optimization. An example of the results obtained for a 10^6 km amplitude orbit inclined by 150° is shown in Figure 4.10. The algorithm converges to a solution after 254 seconds with an end value of the cost function that is equal to 6052 km. The delta-V vector applied is $[-2.0, 4.7, 111.2]$ m/s (in norm 111.3 m/s), and most of the delta-V applied is used to change the inclination. This is because we start with a zero z velocity since we don't know the future initial injection velocity. The orbit is well centered on L5 and both the ESS and SSE angles do not drift anymore. However, we also need to assess the long-term stability of the generated orbit since the mission lifetime could be extended as it was the case for SOHO. This is done in the next subsection.

So far, the optimization was carried out starting at a 90° orbital phase. The cost function being the distance between the initial and last position, we can expect that the initial orbital phase has an impact on the optimization and thus on the end result. As a verification, Figure 4.11 shows the comparison between two optimized orbits starting respectively at a zero and 90° orbital phase. The delta-V vector is this time equal to $[-3.5, -0.5, 53.3]$ m/s (in norm 53.4 m/s). The global delta-V is reduced as well as the in-plane manoeuvre to close the orbit. Even if it takes slightly more time to converge (411 seconds), a zero orbital phase allows to get a more confined orbit. In fact, starting at that peculiar phase forces the orbit to be confined in the vicinity of that point. The latter region being the most sensitive to the long-period shift, this ends in a very closed orbit.

The last effect that could be investigated is the size of the orbit generated. Figure 4.12 reveals that a smaller orbit (10^5 km amplitude) is much more difficult to close properly, at least with this formulation of the problem. Although we have kept the 1000 km tolerance on the cost function, the latter is still 2 orders of magnitude lower than the amplitude of the orbit. A thorough verification has been carried out with a 100 km margin but the obtained orbit is similar to the one on the right of Figure 4.12, except that it takes twice as much time to converge. The width of the trajectory around L5 is certainly not caused by this tolerance. In view of expressions (4.6) and (4.7), the velocity on the orbit is proportional to the amplitude of the latter. Therefore, at a sufficiently small scale, the perturbing accelerations coming from the planets and SRP[1] have enough impact to destabilize the orbit. Before drawing any conclusion on the feasibility of such small orbits for operational purposes, let us study their long-term behaviour.

[1]The effects of the eccentricity and the initial conditions both decrease with a smaller amplitude while SRP and the gravitational force of the other planets are barely independent from the size of the orbit.

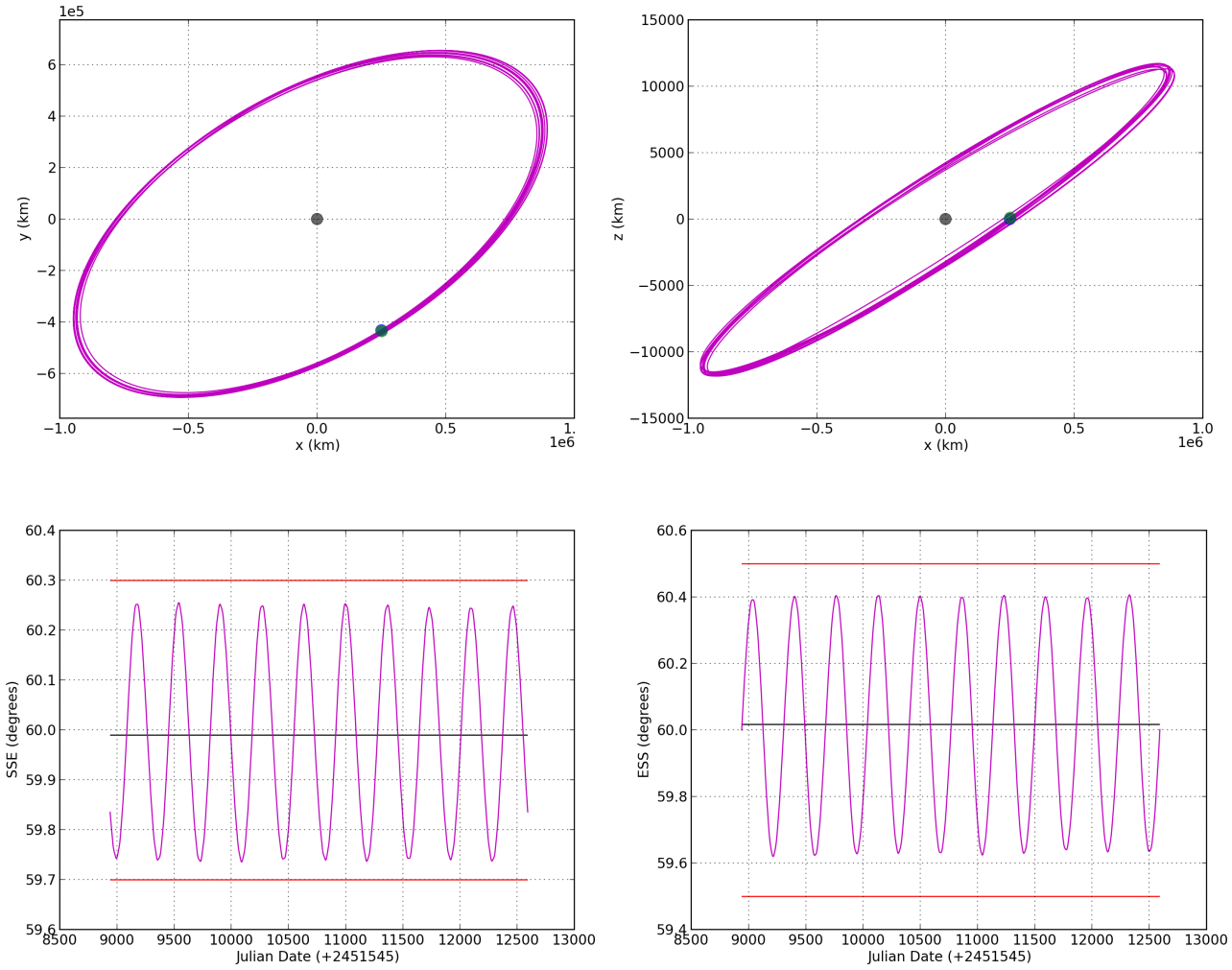

Figure 4.9: Results obtained via the optimization of a 10^6 km amplitude orbit with the COBYLA algorithm. The trajectory is shown in the Earth's rotating frame and centered on L5. Both x-y (top left) and x-z (top right) views are proposed. The evolution of the SSE (bottom left) and ESS (bottom right) angles is also drawn together with their corresponding constraints (red lines) and mean (black line). Solar radiation pressure is taken into account with $C_r = 1.0$. The propagation starts on 21 June 2024 and ends on 21 June 2034. The black dot represents L5 while the blue and green dots stand for the initial and final positions of the spacecraft.

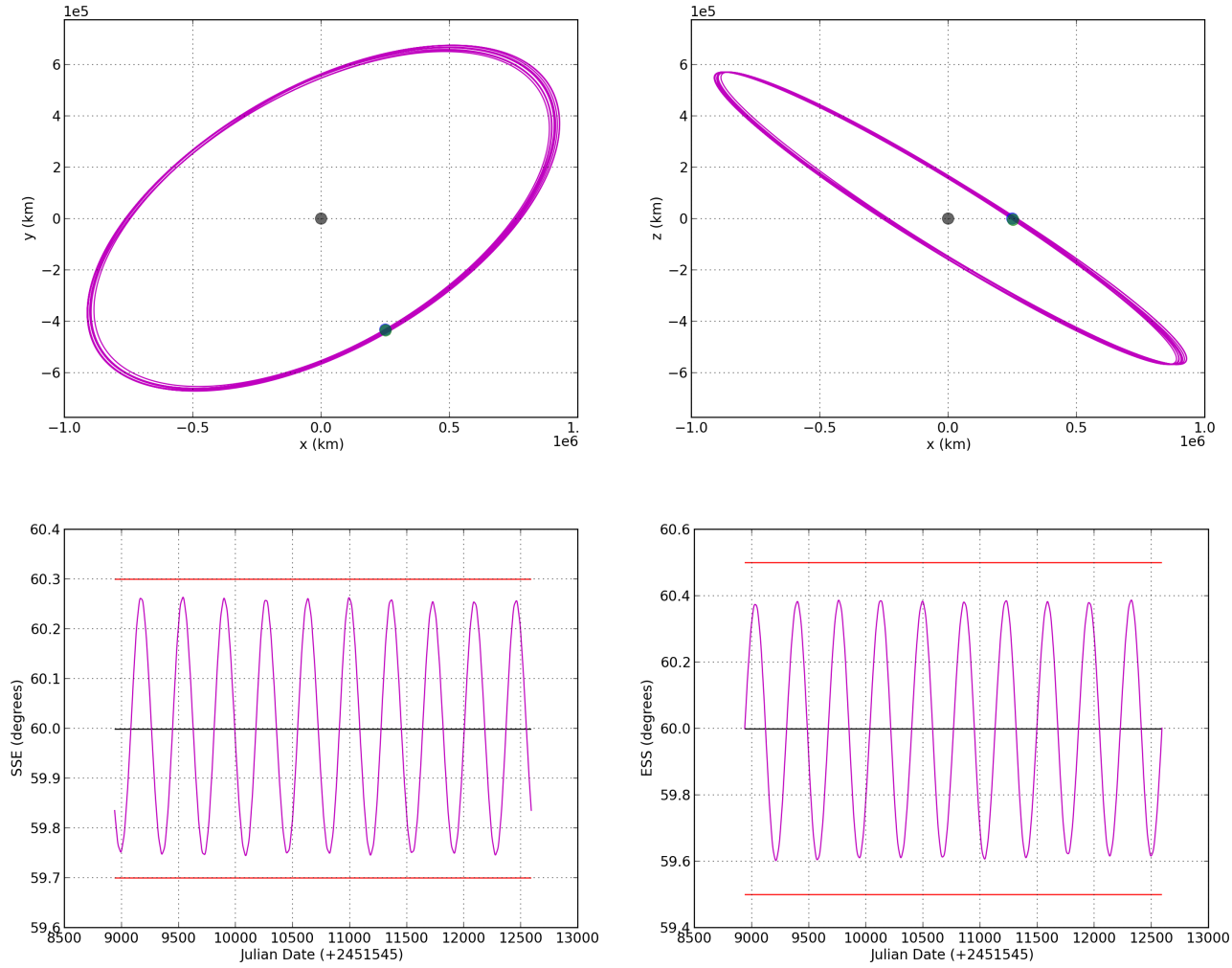

Figure 4.10: Results obtained via the optimization of a 10^6 km amplitude orbit with the COBYLA algorithm. The orbit is inclined by 150° with respect to the ecliptic plane. The trajectory is shown in the Earth's rotating frame and centered on L5. Both x-y (top left) and x-z (top right) views are proposed. The evolution of the SSE (bottom left) and ESS (bottom right) angles is also drawn together with their corresponding constraints (red lines) and mean (black line). Solar radiation pressure is taken into account with $C_r = 1.0$. The propagation starts on 21 June 2024 and ends on 21 June 2034. The black dot represents L5 while the blue and green dots stand for the initial and final positions of the spacecraft.

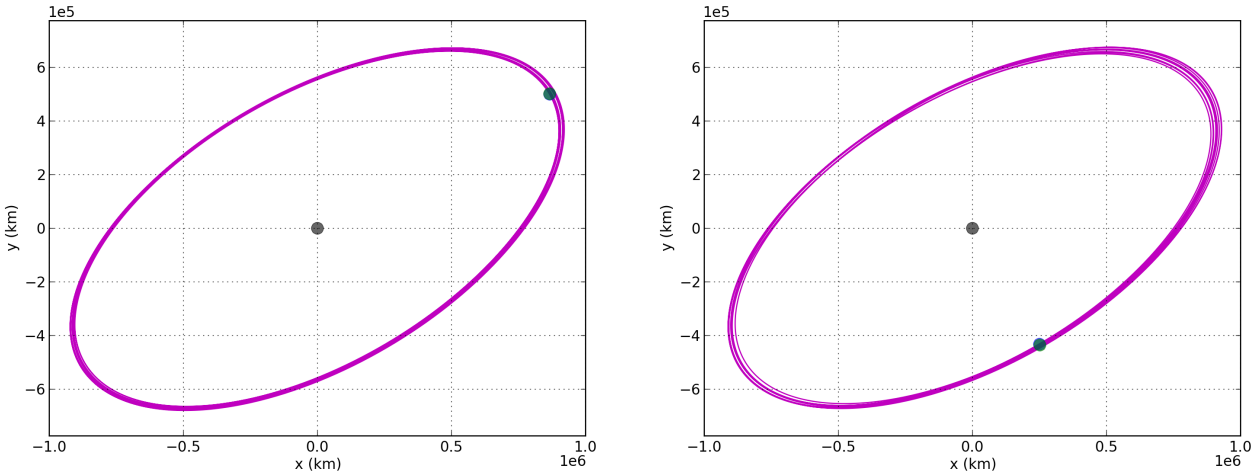

Figure 4.11: Comparison of two orbits obtained via the optimization of a 10^6 km amplitude orbit with the COBYLA algorithm starting at a 0° (left) and 90° (right) orbital phase. The trajectory is shown in the Earth's rotating frame and centered on L5. Solar radiation pressure is taken into account with $C_r = 1.0$. The propagation starts on 21 June 2024 and ends on 21 June 2034. The black dot represents L5 while the blue and green dots stand for the initial and final positions of the spacecraft.

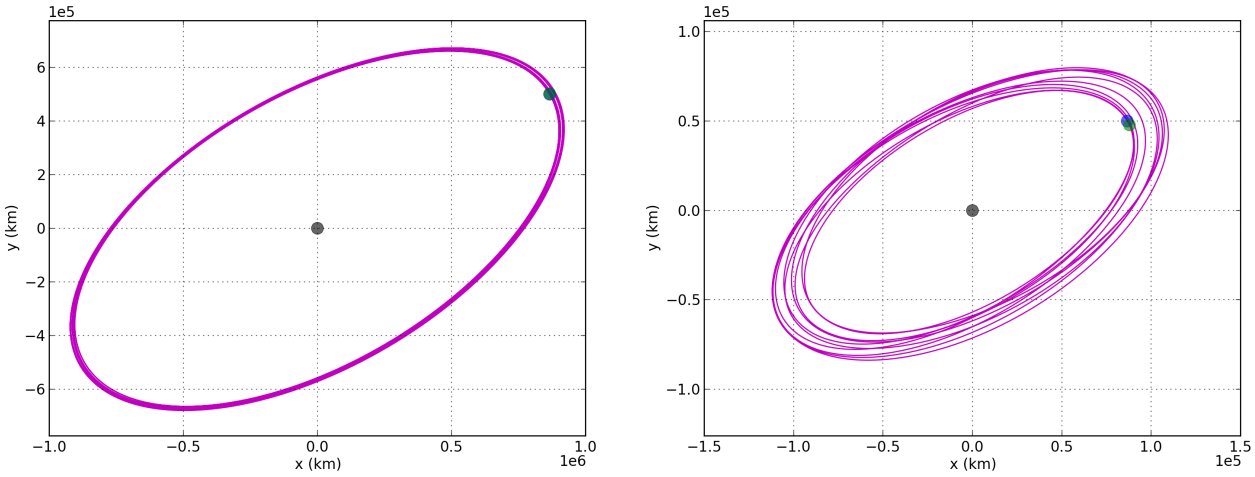

Figure 4.12: Comparison of two orbits obtained via the optimization with the COBYLA algorithm starting at a zero orbital phase. The amplitude is either 10^6 (left) or 10^5 (right) km. The trajectory is shown in the Earth's rotating frame and centered on L5. Solar radiation pressure is taken into account with $C_r = 1.0$. The propagation starts on 21 June 2024 and ends on 21 June 2034. The black dot represents L5 while the blue and green dots stand for the initial and final positions of the spacecraft.

4.2.3 Long-term behaviour

Assessing the long-term stability of the orbits generated with our optimizer is capital if the Lagrange mission would be extended for a couple of years or even some decades. Figures 4.13 and 4.14 show a 50 year and 222 year propagation respectively of a 10^5 and 10^6 km amplitude orbit. The larger orbit is much more stable than the smaller one. This result was expected from previous subsection since the former was more confined than the latter.

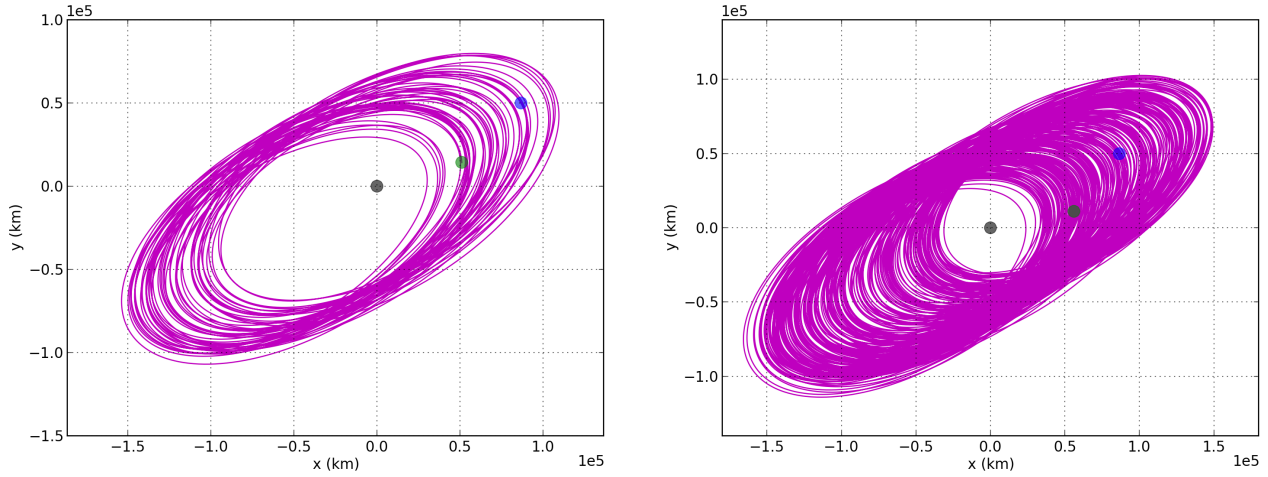

Figure 4.13: 50 year (left) and 222 year (right) propagation of a 10^5 km amplitude orbit obtained via the optimization with the COBYLA algorithm starting at a zero orbital phase. The trajectory is shown in the Earth's rotating frame and centered on L5. Solar radiation pressure is taken into account with $C_r = 1.0$. The propagation starts on 21 June 2024. The black dot represents L5 while the blue and green dots stand for the initial and final positions of the spacecraft.

However, it would be interesting to know whether our implementation is adapted to small orbits or if there is no way to constrain an orbit with such a scale. For this, it is necessary to add some inequalities stating the maximum and minimum extent of the orbit. In Figure 4.12, the small amplitude orbit extends about 25 percents further than the expected width of the orbit. Let us try to lower this quantity to 20 or even 10 percents with the following constraint (in the 10% case):

$$0.95\,\text{amplitude} \leq \text{semi-major axis} \leq 1.05\,\text{amplitude} \tag{4.10}$$

Note that the relative closeness of the orbit is here defined for a 10 year time window. This restriction does not hold anymore for a longer propagation. In both cases, the algorithm does not find any point that satisfies all constraints. Therefore, it seems that the trajectory found in the previous subsection was the best operational orbit achievable at this scale. The amplitude threshold for which it is possible to find a close orbit with less than 20% variation in semi-major axis is found in between $3\,10^5$ and $4\,10^5$ km. In the same way, a 10% departure is obtained for an orbit amplitude of about $6\,10^5$ km. A 50 year propagation of the obtained $4\,10^5$ and $6\,10^5$

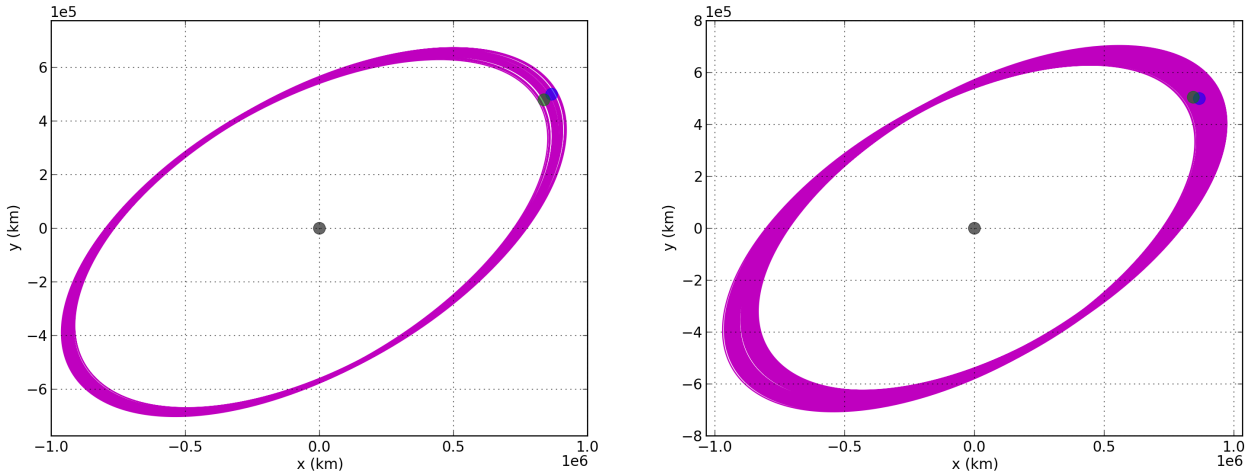

Figure 4.14: 50 year (left) and 222 year (right) propagation of a 10^6 km amplitude orbit obtained via the optimization with the COBYLA algorithm starting at a zero orbital phase. The trajectory is shown in the Earth's rotating frame and centered on L5. Solar radiation pressure is taken into account with $C_r = 1.0$. The propagation starts on 21 June 2024. The black dot represents L5 while the blue and green dots stand for the initial and final positions of the spacecraft.

km amplitude orbits is proposed in Figure 4.15. As it is expected, the lower the variation in a 10 year window, the more adequate is the orbit in the case of an extended mission. That is why a larger orbit is recommended for use as an operational orbit.

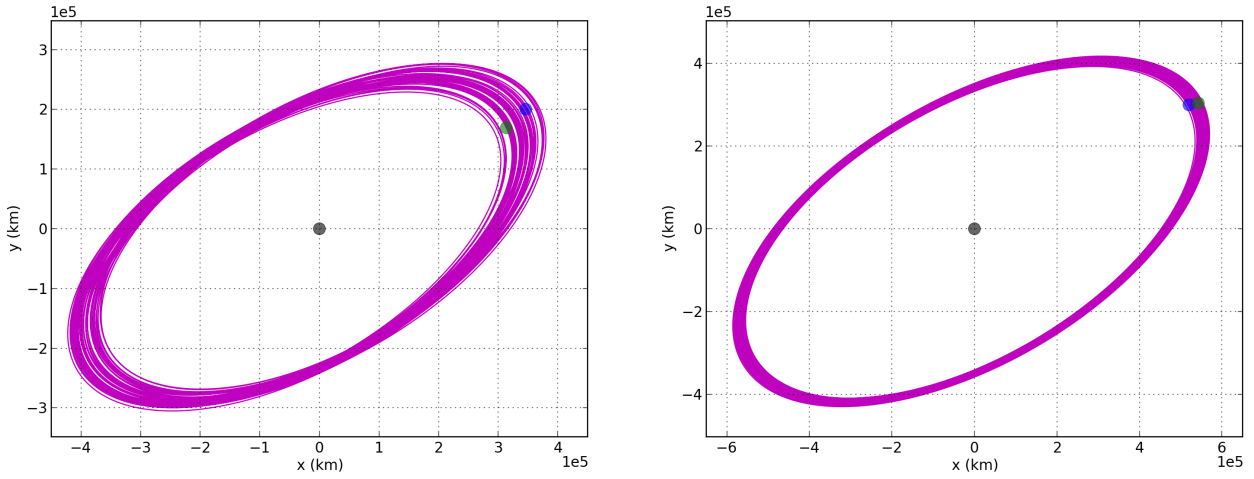

Figure 4.15: 50 year propagation of a $4\,10^5$ (left) and a $6\,10^5$ (right) km amplitude orbit obtained via the optimization with the COBYLA algorithm. The spacecraft starts at a zero orbital phase. The trajectory is shown in the Earth's rotating frame and centered on L5. Solar radiation pressure is taken into account with $C_r = 1.0$. The propagation starts on 21 June 2024 and ends on 21 June 2074. The black dot represents L5 while the blue and green dots stand for the initial and final positions of the spacecraft.

4.2.4 Largest achievable orbit

Following the need of establishing the smallest operational orbit that is achievable with our optimization problem, it is also convenient to set an upper limit. Once again, we will make use of the criteria (4.10) to find the largest orbit exhibiting less than 10% variation in its semi-major axis. For this, we enlarge the admissible bounds on the x and y velocity components to 50 m/s and scale the tolerances on the mean of both angles to $0.001\,(\text{amplitude}/10^6)$. Note that the constraints on the magnitude of the SSE and ESS angles (namely 1 and 2) have to be relaxed since the maximum amplitude could violate them. The amplitude that satisfies all the constraints stated above is found around $1.6\,10^6$ km. The final orbit generated is shown in Figure 4.16 together with a 222 year propagation. After a 10 year propagation the orbit seems very tight, even more than what we have achieved for a 10^6 km orbit in the previous subsection. However, the long-period component has more impact than in the latter case since the linear CRTBP solution is less valid at larger scale. That is also why it becomes more and more difficult to stabilize orbits with an increasing amplitude.

As a conclusion, our optimization process allows to generate stable orbits (showing less than a 10% variation in semi-major axis in a 10 year window) with an amplitude in the range $[6, 16]\,10^5$ km.

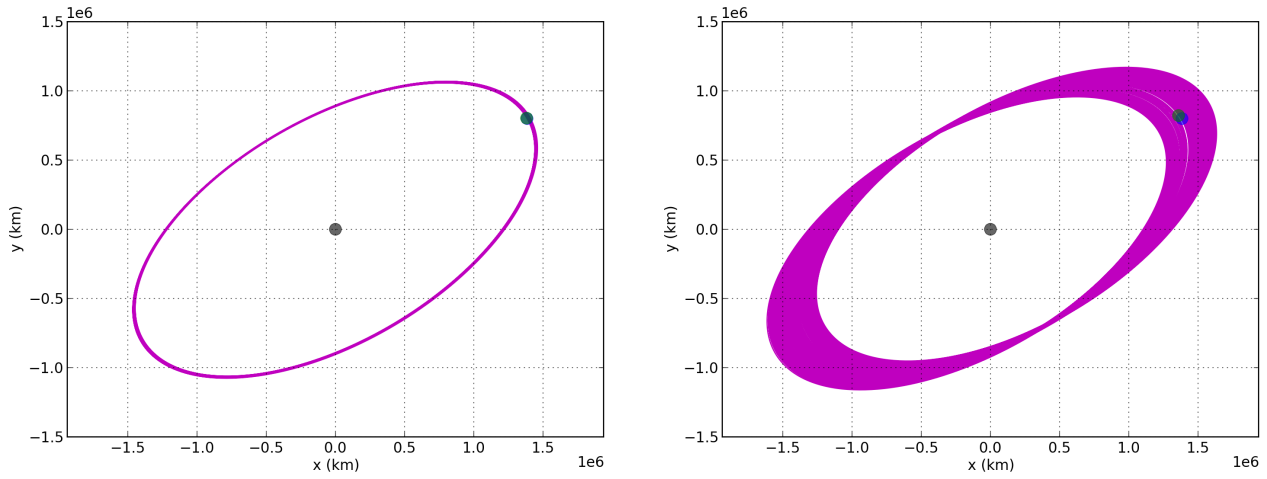

Figure 4.16: 10 year (left) and 222 year (right) propagation of a $1.6\,10^6$ km amplitude orbit obtained via the optimization with the COBYLA algorithm starting at a zero orbital phase. The trajectory is shown in the Earth's rotating frame and centered on L5. Solar radiation pressure is taken into account with $C_r = 1.0$. The propagation starts on 21 June 2024. The black dot represents L5 while the blue and green dots stand for the initial and final positions of the spacecraft.

Chapter 5

Space debris distribution in case of a fragmentation event

Space debris mitigation is a brand new topic in space exploration. The density of objects around the Earth increases so fast that the risk of collisional cascading is becoming a real problem. This effect, sometimes referred as the Kessler syndrome, can at some point congest and even inhibit the access to space for several generations (*Kessler & Cour-Palais, 1978*). The debris issue will again be reinforced with the foreseen launch of several constellations made up of few hundreds of cubesats. Moreover, the rise of private companies specialized in small launchers gives a cheaper and easier access to space, increasing the targeted public. If reducing the number of launches is far from being feasible, developing strategies to remove debris and non-operational satellites is becoming a necessity. Some agencies and universities are currently designing capture systems like a harpoon, a magnetic boom or a deployable net (*Emspak J., 2016*). Another approach consists in developing contactless techniques based either on laser or ion beams (*Gough E., 2018*). Using atmospheric drag as a way to lower the altitude has also been investigated and successfully tested with the InflateSail project in 2017 (*Surrey Space Centre website*). However, all these approaches are limited to the close vicinity of the Earth, namely the LEO range. In the case of interplanetary missions, end-of-life spacecraft are either driven to a safe orbit, called graveyard or disposal orbit, where they will be abandoned (Herschel, Planck, etc.) or they are forced to crash on their survey body (Galileo on Jupiter, Cassini-Huygens on Saturn, etc.). The disposal strategies for satellites in orbit around the Sun-Earth triangular Lagrangian points will be considered in the next chapter. Regarding the linear stability of these points, keeping their environment free of any debris is of fundamental importance for further missions. The present chapter is therefore dedicated to the analysis of the debris distribution in the vicinity of L4 and L5 in case of a fragmentation event. This study aims at providing a prior mapping of debris spreading for different scenarios of explosion as well as highlighting the major drivers in each case.

5.1 The SNAPPshot software and its breakup model

To simulate spacecraft fragmentation events, we will use the ESA planetary protection software, called SNAPPshot (Suite for the Numerical Analysis of Planetary Protection). Developed in Fortran 90, it provides several drivers that can directly be used from a Linux terminal. SNAPPshot is designed to verify the compliance with planetary protection requirements in the event of a failure of the spacecraft propulsion system, when there is some uncertainty on the dispersion of an interplanetary launcher and in case of collision or explosion events. In this part, we are only interested in the explosion branch of the software as there is currently no other spacecraft orbiting around L4 or L5 to cause any collision. Both collision and explosion events implemented into SNAPPshot are based on the EVOLVE NASA breakup model described in *Johnson N. L. et al., 2001*. The latter was built thanks to the data collected since the early 1980's, including ground-based controlled experiments, hypervelocity collisions in low-Earth orbit, the Ariane upper stage sub-scale explosion tests and a compilation of historical orbital data (i.e. two-line element sets). By gathering all these data, the NASA Orbital Debris Program Office derives some laws relating the characteristic length, the area-to-mass ratio, the mass and the delta-V magnitude of the generated debris. The characteristic length (or size) is taken as the independent variable of the model, i.e to a certain characteristic length is associated a fitted law that links the latter to each of the other three parameters. The number of debris generated with a specific length in an explosion is an inverse power law of that length, i.e. more debris are produced for a smaller size. To be consistent with the whole model, when drawing a size distribution among the cloud, we need to generate as many debris of a certain size as required by the power law. Therefore, if there exist 20 different characteristic lengths among the cloud, the total number of debris will be made up of 20 groups of debris, each of them containing the number of items stated by the power law. Then, the other three parameters are built up according to their relations with the debris size. As described above, the NASA breakup model only gives the delta-V magnitude that each debris is subjected to and does not bring any information about the direction of the latter boost. An assumption underlying the implementation in SNAPPshot was to generate spherically distributed velocity vectors (*Letizia F., 2016*) in order not to add any bias in the cloud migration. The relevance of this hypothesis will be emphasized in the following parts.

The model takes as inputs the mass and the kind of object (satellite or rocket body) as well as the event it is subjected to (explosion or collision). Finally, we are free to set the limits of the characteristic length distribution for the generated debris. However, to prevent identical size distributions to be created from the same limits, a pseudo-random uniform distribution is added on top of the first one. Once the cloud is properly created, SNAPPshot then propagates each debris for a given period of time. Note that the SRP model implemented in the SNAPPshot propagator is the same as the one in MASW. In the end, SNAPPshot produces the trajectory file of each debris, containing the epoch and the position and velocity vectors in the requested

frame, and a cloud file including the whole information on each debris (size, mass, area-to-mass ratio and initial delta-V magnitude and vector). As SNAPPshot has currently no graphical interface, all the results are drawn with Python via the Visual Studio Code editor.

5.2 Software settings and explosion scenarios

SNAPPshot contains a Solar system propagator based on the planetary ephemeris taken from the NASA NAIF website. The file used is *de435.bsp* whose ephemeris are available from 31 December 1549 to 25 January 2650. The gravitational parameters of the planets and the ephemeris of L4 (*L4_de431.bsp*) and L5 (*L5_de431.bsp*) are also available on that website. However, the positions of the two Lagrangian points are computed from 1st January 1900 to 1st January 2151.

Regarding the generation of the debris cloud, the pieces are created with a characteristic length between 10 cm and 1 m. We first select 9 logarithmic spaced values within these two limits and then generate the number of debris related to each size thanks to a power law relation. Logarithmic spaced values allow producing a higher number of small debris, yielding a much more consistent explosion cloud. The number of levels selected in the range $[0.1, 1]$ metres, i.e 9 different lengths, has been established so that an acceptable number of debris are created. Indeed, if we take additional logarithmic levels, there will be more and more small size debris, resulting in a higher number of objects to propagate. This therefore appears to be a good compromise between the computing time and the need of a consistent explosion model. For the same purpose, we have set the minimal size of the debris to 10 cm while a correct implementation of the NASA breakup model includes the distribution of fragments from 1 mm to 1 m with an additional two to eight large fragments beyond 1 m (*Krisko P., 2011*). Limiting ourselves to these bounds has a big consequence in terms of mass conservation. In fact, the whole NASA model is fitted to conserve the initial mass of the exploding body and split it into a bunch of fragments. The current model will therefore not satisfy mass conservation. However, this is not a major concern as our interest is mainly to study the distribution of debris in the vicinity of L4 and L5.

The NASA breakup model is designed to generate high fidelity explosions and collisions based on both in-orbit and ground experiments. From the latter data, the delta-V increment acquired after an explosion is never higher than 1.3 kilometres per second (*Letizia F., 2016*). As we have seen in Chapter 3, this is sufficient to reach the Earth if the boost is properly oriented. It could be valuable to scale down this velocity limit to 10 or 100 metres per second and study the debris dispersion in each case. This is comparable to examine different severity levels for on-board explosions. In the following, we will consider low, middle and high severity events, respectively with a maximum delta-V boost of 10, 100 and 1000 metres per second.

5.3 Debris dispersion study

5.3.1 Break-up at L4 or L5

As a first step in the debris distribution study, let us place the satellite exactly at L4 or L5. In this way, we do not account for the orbital velocity of the spacecraft on its operational orbit. We will consider a propagation time of 250 years, keeping in mind the long-period oscillation motion that governs the dynamics in the vicinity of the triangular Lagrangian points. Because of the computational cost inherent to the propagation of many debris, we keep only the major perturbing planets in SNAPPshot, i.e. Venus, the Earth (with the Moon), Mars, Jupiter and Saturn. In the example below, the propagation starts on 1st January 1900 because SNAPPshot internally reads the position of either L4 or L5 from the NASA ephemeris. As it can be seen in the following, the starting epoch does not affect the general behaviour sketched in the figures hereafter. Moreover, the ephemeris files cover an epoch range which is larger than the period of the long-period motion, allowing one full oscillation around L5.

Figures 5.1, 5.2 and 5.3 show the evolution of the resulting debris distribution at time intervals of 50 years in the Earth's rotating frame respectively for a 10, 100 and 1000 m/s explosion event. To compare the three scenarios, we have generated a debris cloud with the same features (i.e mass, area-to-mass ratio, characteristic length and delta-V direction), but with a scaled delta-V magnitude. The total number of debris amounts to 229 in those cases. Note that the solar radiation pressure has been taken into account with a reflection coefficient arbitrary set to $C_r = 1.5$.

The first conclusion is that a fragment needs a velocity boost somewhere in between 10 and 100 m/s to leave the tadpole region, which is in accordance with the results from Chapter 3. Figure 5.1 also shows that the debris are subjected to a pendulum motion when they stay in the vicinity of L5. This is again the manifestation of the long-period component that governs the dynamics around the triangular points. On the other hand, some debris accumulate near the Earth for a 1000 m/s explosion (5 exactly). These points correspond to fragments that collide either with the Earth or the Moon. Indeed, they have been frozen at their last positions before they encounter any celestial body. This behaviour was expected since the velocity threshold to reach the Earth has been estimated to $160 - 200$ m/s in Chapter 3. Globally, for the major explosion, we found 173 debris staying on a tadpole orbit (75.8%), 51 that enter into a horseshoe orbit (22%) and 5 that collide with the Earth-Moon system (2.2%). Another remark can be raised regarding Figure 5.1. In fact, all the debris seem to start in the direction opposite to the Earth while the explosion cloud is expected to be symmetric. A reverse conclusion can be drawn for L4 in Figure 5.4, where the fragments start in the Earth's direction. Two effects can be responsible for this initial drift: the planetary configuration at the time of the explosion or the solar radiation pressure. Let us therefore determine which one is in cause.

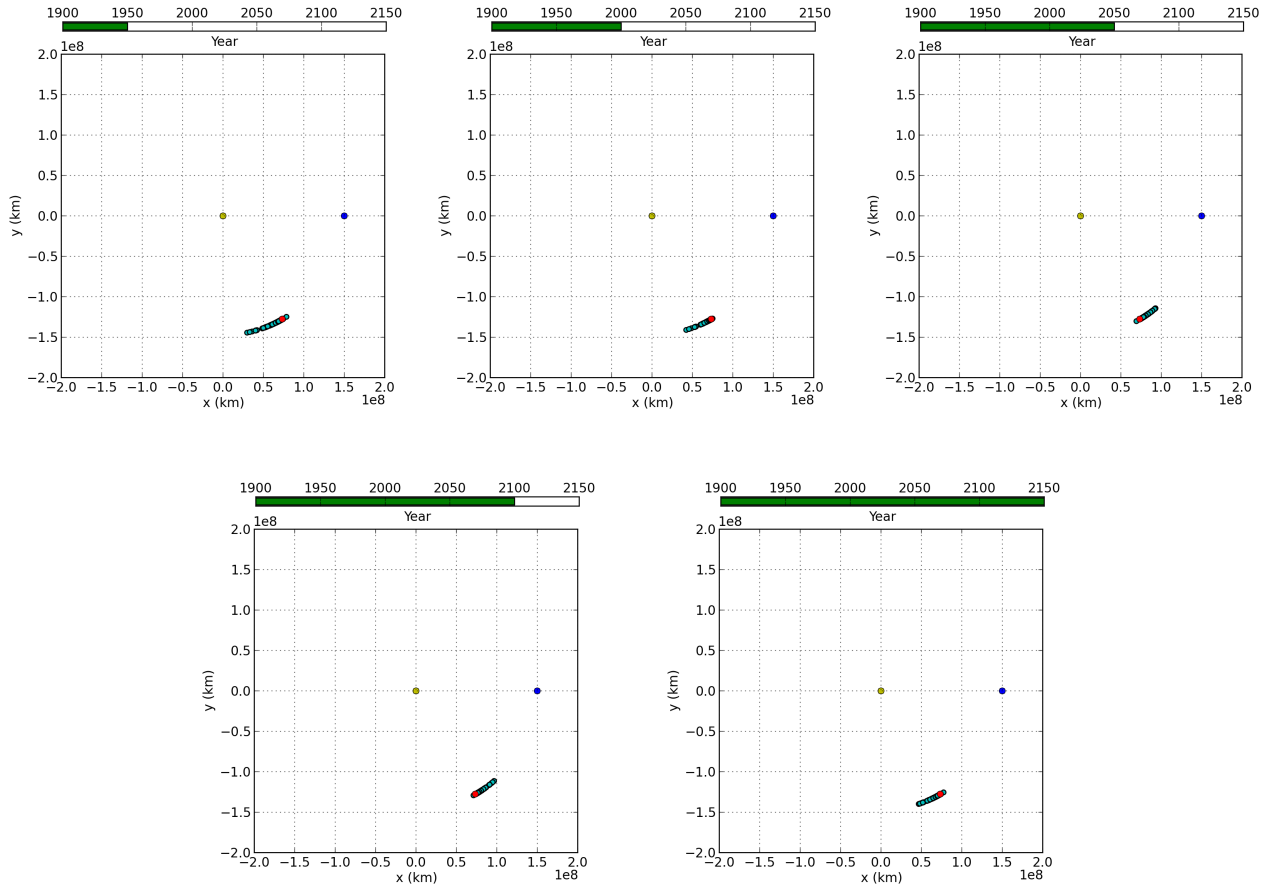

Figure 5.1: Debris distribution after a spacecraft explosion occurring exactly at L5. The debris positions (cyan) are shown in the Earth's rotating frame. The maximum velocity increment after the explosion has been set to 10 m/s. The yellow, blue and red dots respectively stand for the initial position of the Sun, the Earth and L5.

We can carry out the propagation of the debris starting at some different dates through the year 1900. In this way, the spacecraft will encounter different planetary configurations and this should reveal the impact of the other planets on the debris migration. This has been done in Figure 5.5 for 4 different dates separated by 90 days. Unfortunately, the result is identical as in Figure 5.1 and the planets are not responsible for the drift observed. Rather, let us deactivate the SRP effect by setting $C_r = 0$. The cloud dispersion with time is seen in Figure 5.6. At any time, the shape of the cloud is symmetric with respect to L5, exhibiting an accordion behaviour. Let us examine in details the effect of the SRP on the debris distribution.

As we have seen, the solar radiation pressure drives the extent of the debris cloud. For both L4 and L5, the initial flickering lies in the clockwise direction whatever the planetary configuration. In fact, the solar pressure acts as a gravitational shield as it pushes the spacecraft away from the Sun. The debris having a relatively high area-to-mass ratio thus feel a lower gravitational

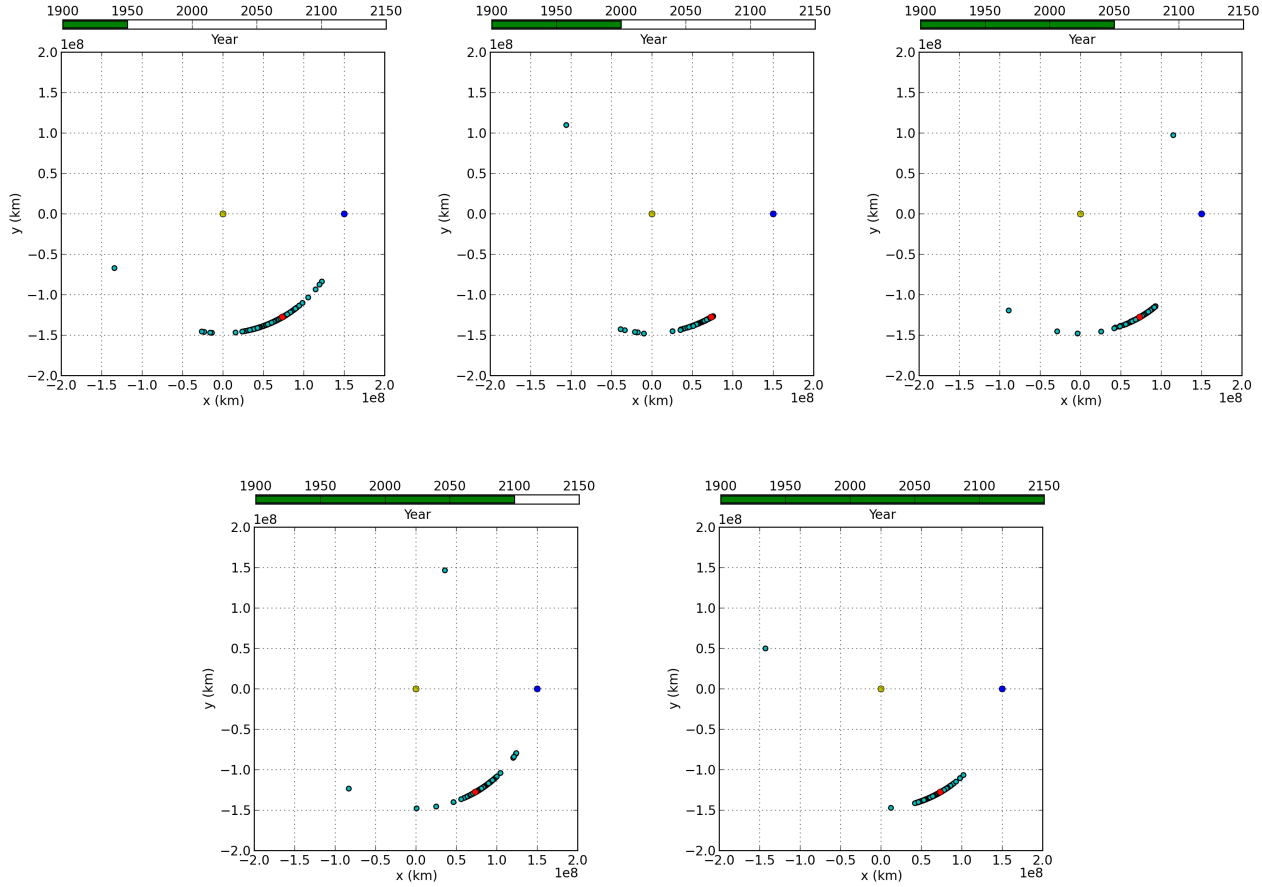

Figure 5.2: Debris distribution after a spacecraft explosion occurring exactly at L5. The debris positions (cyan) are shown in the Earth's rotating frame. The maximum velocity increment after the explosion has been set to 100 m/s. The yellow, blue and red dots respectively stand for the initial position of the Sun, the Earth and L5.

attraction which is equivalent to reducing the gravitational parameter (GM) of the Sun. The velocity on a circular orbit being equal to $\sqrt{\frac{GM}{R}}$, the debris are therefore slowed down and move in the clockwise direction in the Earth's rotating frame. Moreover, as there exists a certain distribution in area-to-mass ratio among the debris, they do not all feel the same braking effect. This can be seen in Figure 5.7 where the amplitude of the oscillation motion seems proportional to the A/M ratio of the debris. However, the ejection velocity acquired from the explosion plays also a role in the dispersion of the cloud, as it can be seen in Figure 5.8 for the extreme explosion case. For that reason, there must exist some threshold velocity above which the debris motion is no more driven by the SRP. To evaluate this limit, let us draw the maximum angular distance of the debris as a function of both the area-to-mass ratio and the delta-V (in magnitude) received after the explosion for different scenarios. The angular distance is defined as the maximum L5-Sun-Spacecraft angle and quantifies the spatial extent of the debris orbit along the Earth's orbital path. Figure 5.9 shows the results obtained for a 10, 30, 70 and 200 m/s explosion. A linear fit is also proposed for the A/M scatter plot and has been carried out thanks to the

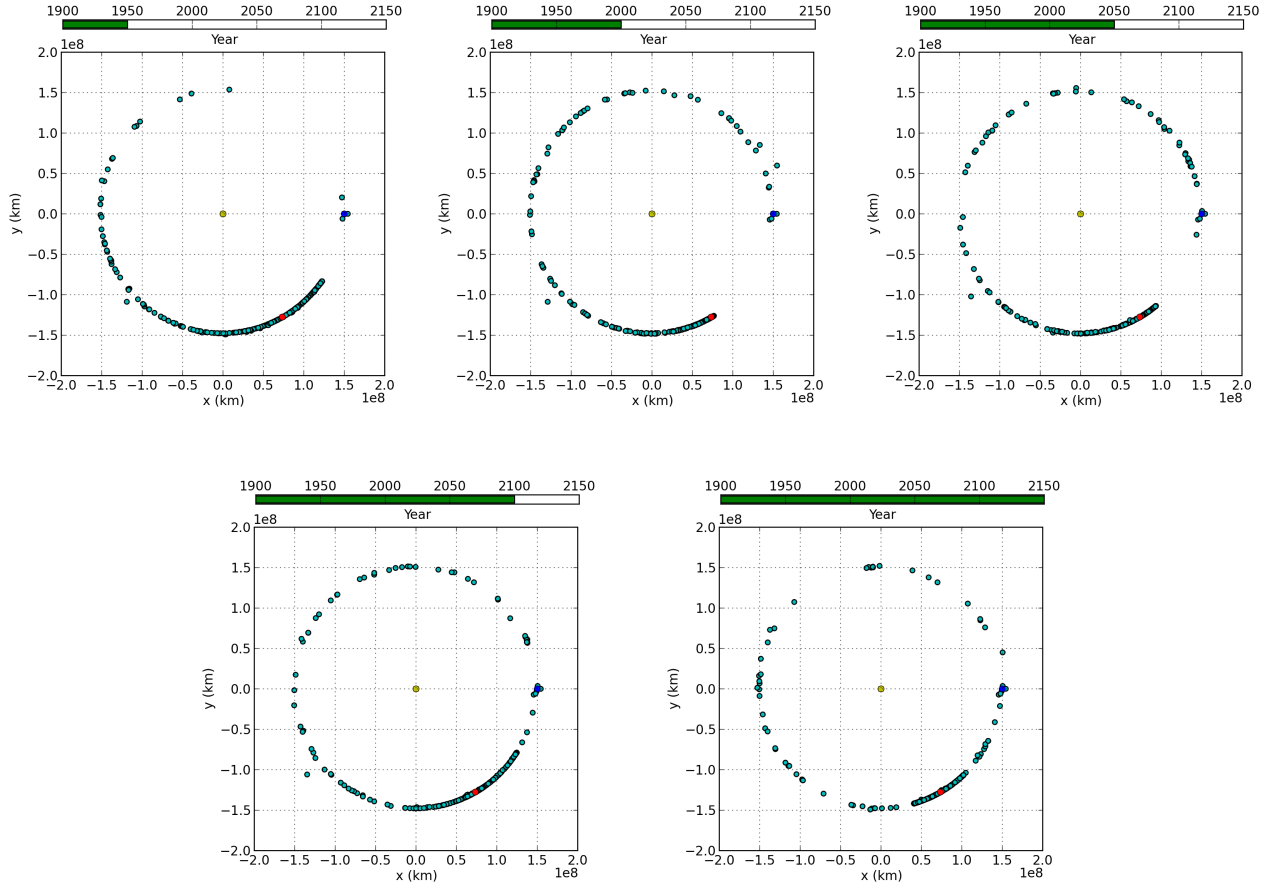

Figure 5.3: Debris distribution after a spacecraft explosion occurring exactly at L5. The debris positions (cyan) are shown in the Earth's rotating frame. The maximum velocity increment after the explosion has been set to 1000 m/s. The yellow, blue and red dots respectively stand for the initial position of the Sun, the Earth and L5.

Numpy's *polyfit* built-in function which uses a least-square method. The fitting coefficients are collected in Table 5.1.

Explosion scenario (m/s)	**Slope**	**Intercept**
10	34.63	-0.53
30	35.37	-0.12
70	35.75	1.59
200	42.88	12.38

Table 5.1: Slope and intercept coefficients obtained through a linear fit of the scatter plot showing the debris maximum orbital phase as a function of their A/M ratio. Note that the SRP coefficient has been set to 1.5.

As we can see, a linear relation exists between the maximum L5-Sun-Spacecraft angle and the

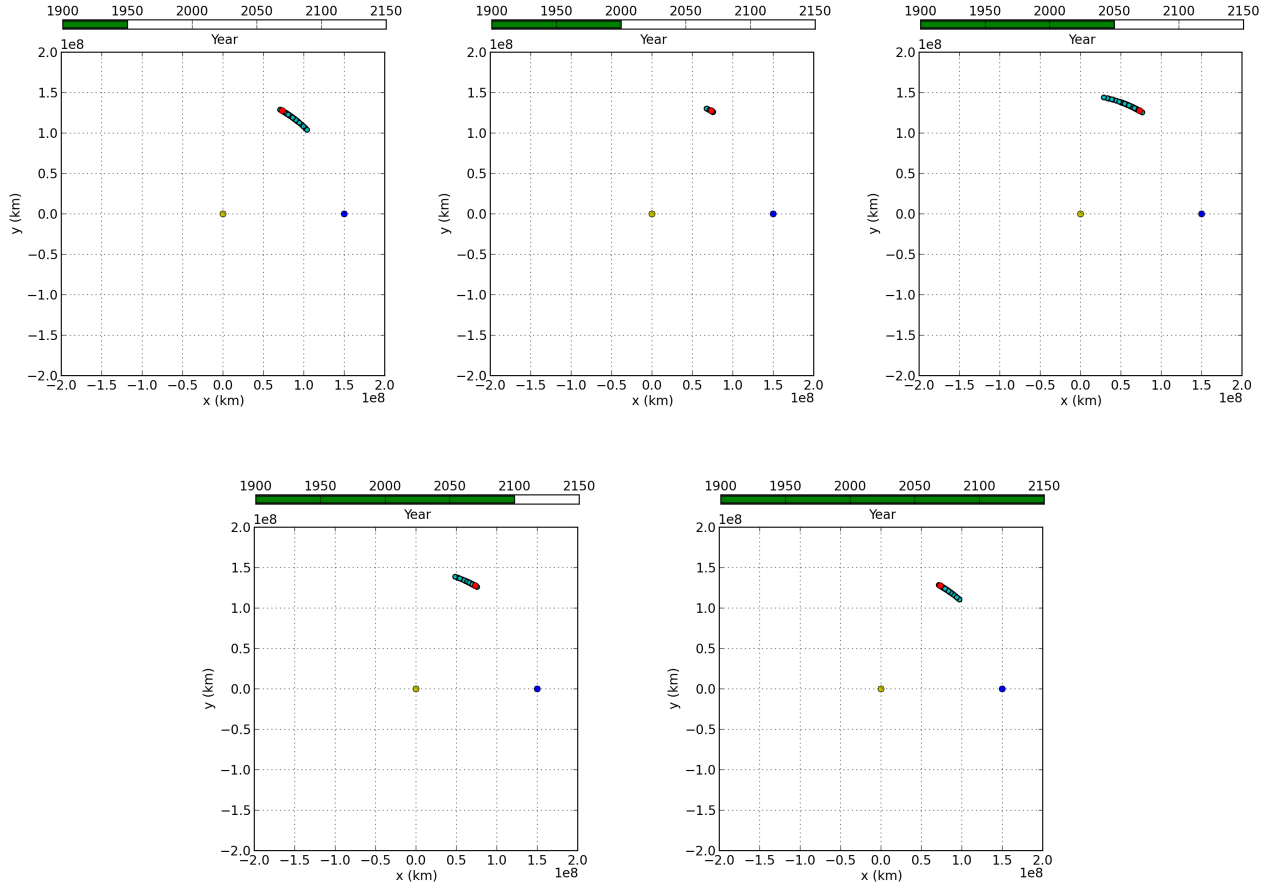

Figure 5.4: Debris distribution after a spacecraft explosion occurring exactly at L4. The debris positions (cyan) are shown in the Earth's rotating frame. The maximum velocity increment after the explosion has been set to 10 m/s. The yellow, blue and red dots respectively stand for the initial position of the Sun, the Earth and L5.

area-to-mass ratio of the debris for low ejection velocity events. Some outliers are found in those graphs but they correspond to fragments that receive a relatively high delta-V boost which was properly oriented[1]. As the delta velocity becomes higher, the number of outliers increases and the A/M relation flattens. At the same time, the delta-V relation starts to tighten and a positive slope slowly appears. Beyond that limit, the solar radiation pressure still drive the spatial extent of the cloud as it plays a role in the migration of the slower debris, which are more numerous[2]. In the last row of Figure 5.9, there exists a velocity threshold below which no debris are found more than 120 degrees away from L5, corresponding to the L3 position and the entrance of the horseshoe region. This velocity limit is about 40 m/s which is in perfect agreement with Chapter 3, where the ideal disposal manoeuvre to reach this region was found to be directed along the Earth's orbital path. Once the debris acquire a higher boost, they are free to move from L3 to the Earth via L4 and their maximum orbital phase is then bounded by 300

[1]To leave easily the L5 region, the velocity boost needs to be somewhat directed along the Y axis defined in Chapter 4.

[2]According to the NASA's EVOLVE breakup model.

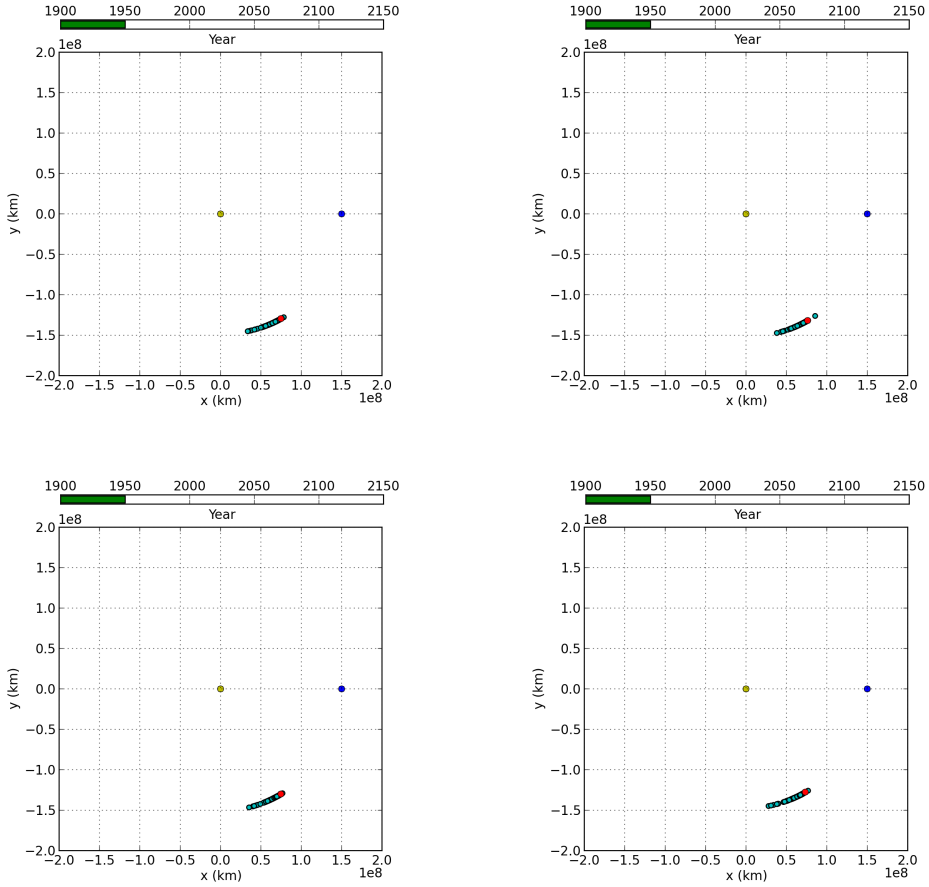

Figure 5.5: Debris distribution 50 years after a spacecraft explosion occurring exactly at L5. The explosion either takes place 90 (top left), 180 (top right), 270 (bottom left) or 360 (bottom right) days after the 1st January 1900. The debris positions (cyan) are shown in the Earth's rotating frame. The maximum velocity increment after the explosion has been set to 10 m/s. The yellow, blue and red dots respectively stand for the initial position of the Sun, the Earth and L5.

degrees. We need to be careful with the results presented so far since they were carried out with an SRP coefficient equal to 1.5. There is no doubt that the linear relation with the A/M ratio exist for other SRP coefficients but the fitted coefficients will be different from our nominal case. As a comparison, we have considered the cases $C_r = 0.5$, $C_r = 1.0$ and $C_r = 2.0$. The linear coefficients for each case are shown in Table 5.2. Excepting the 200 m/s event which is not meaningful because of the presence of a relatively high number of outliers, the slope of the linear fit appears proportional to the SRP coefficient. In Figure 5.10, we draw the relation between the slope of the fit (obtained from the 10 m/s event to minimize the effect of the ejection velocity) and the C_r coefficient for the four values acquired so far. A linear and a quadratic fit are added on top of the scatter plot. The quadratic polynomial appears barely better than the linear fit in catching accurately the 4 points. Also, note that we expect the slope to be zero when SRP is deactivated, i.e when $C_r = 0$. This is not exactly the case in Figure 5.10 because of the presence of some outliers that influence the quality of the fit. The obtained linear law is the following:

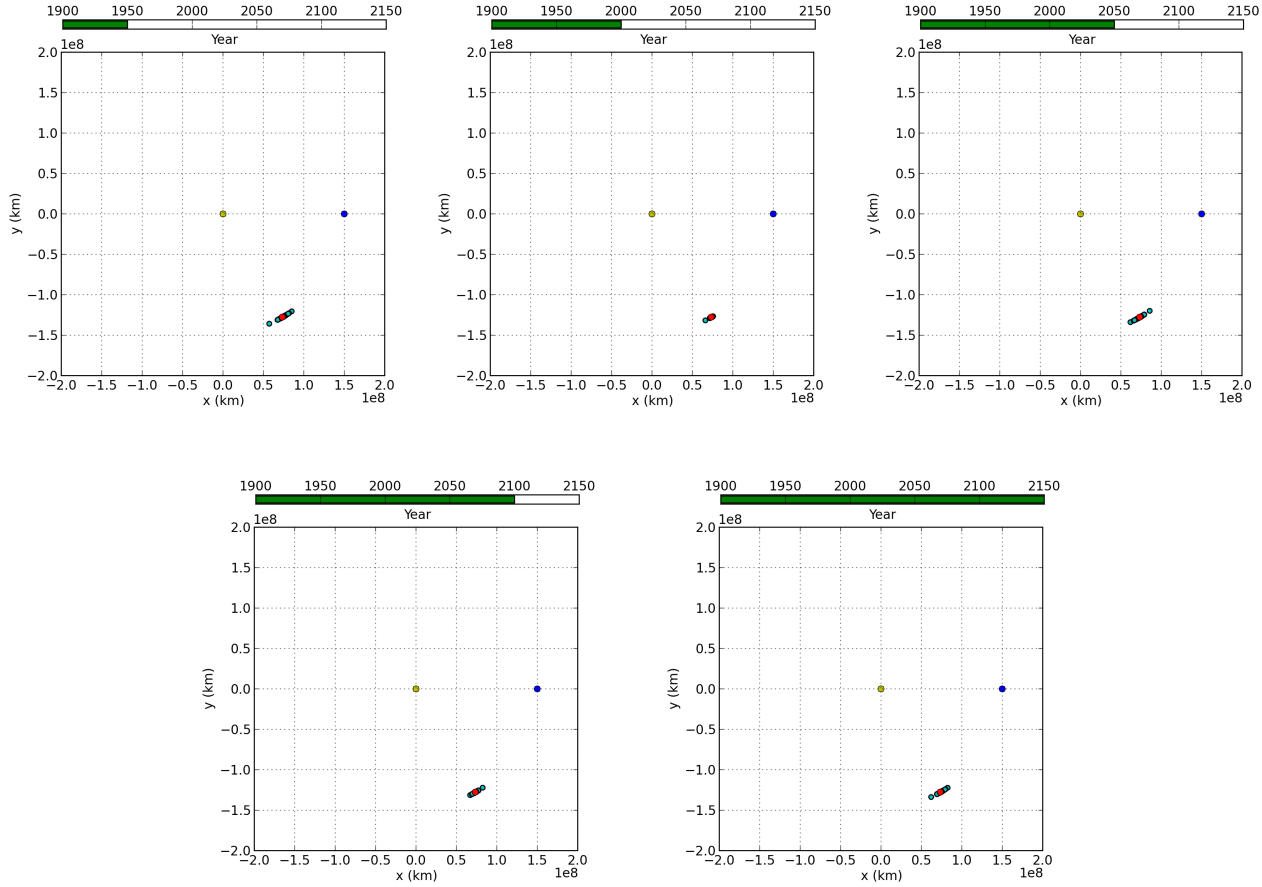

Figure 5.6: Debris distribution after a spacecraft explosion occurring exactly at L5. Note that the propagation does not take the SRP into account. The debris positions (cyan) are shown in the Earth's rotating frame. The maximum velocity increment after the explosion has been set to 10 m/s. The yellow, blue and red dots respectively stand for the initial position of the Sun, the Earth and L5.

$$Slope = 23.86\, C_r - 0.8 \tag{5.1}$$

The linear behaviour that links the slope of the fit and the C_r coefficient is expected from the SRP acceleration in equation (4.1). Indeed, the area-to-mass ratio impacts the debris motion in the same way as the SRP coefficient since the latter is nothing else than a multiplying factor. A way to rub out the effect of that coefficient would be to divide the maximum L5-Sun-Spacecraft angle by the current C_r. This will then always give the same slope whatever the magnitude of C_r, i.e about 23.86 as in the above relation.

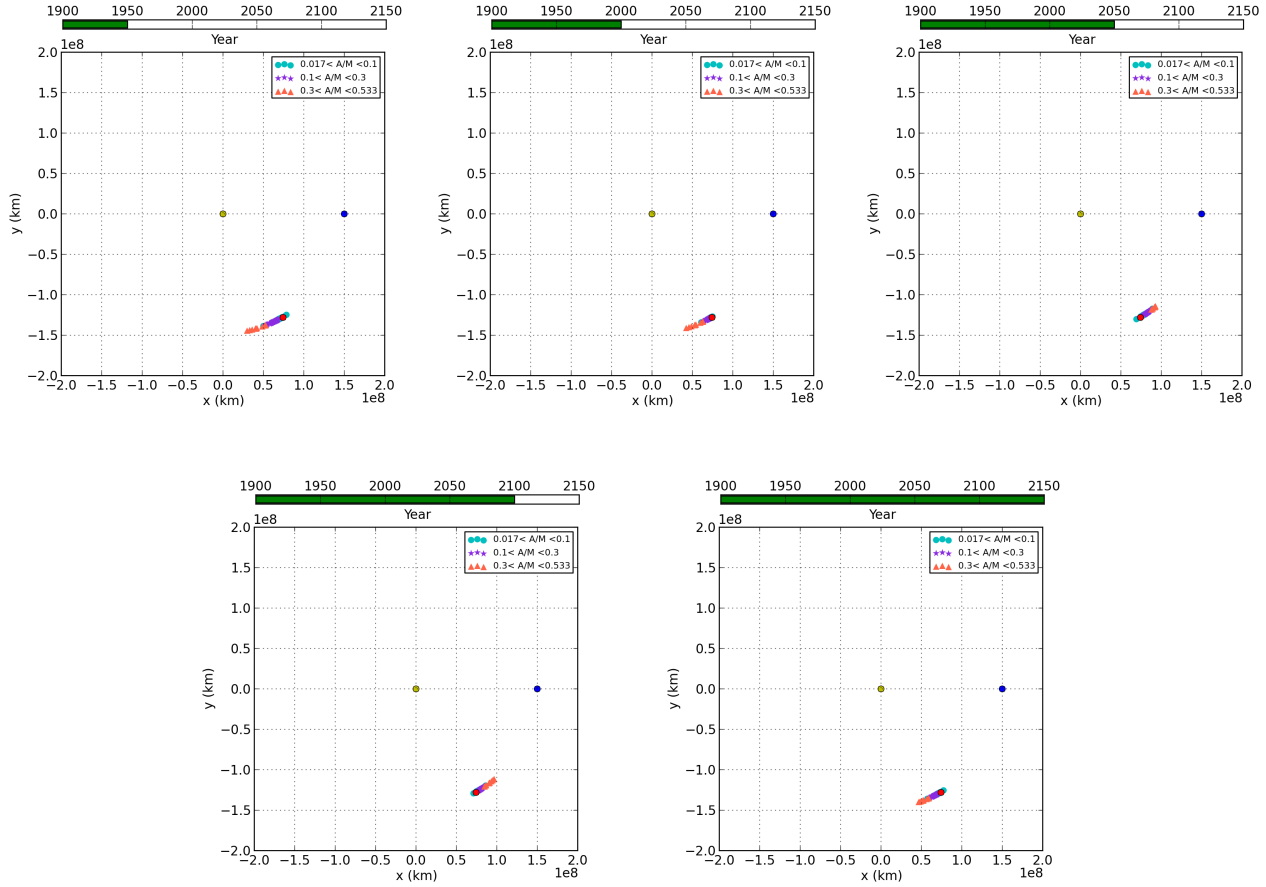

Figure 5.7: Debris spatial extent as a function of the A/M ratio (in m^2/kg). The debris positions are shown in the Earth's rotating frame. The maximum velocity increment after the explosion has been set to 10 m/s. The yellow, blue and red dots respectively stand for the initial position of the Sun, the Earth and L5.

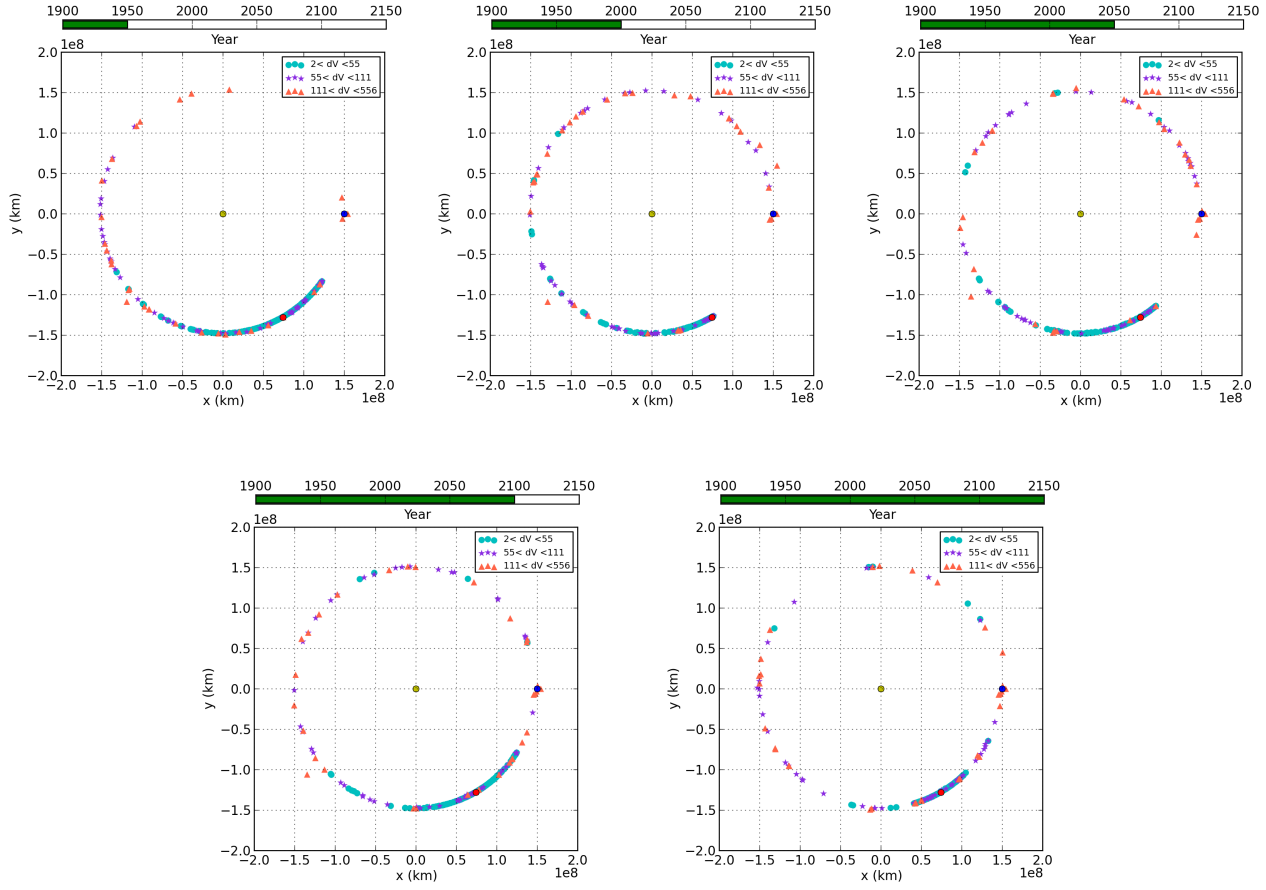

Figure 5.8: Debris spatial extent as a function of the delta-V boost (in m/s) received after the explosion. The debris positions are shown in the Earth's rotating frame. The maximum velocity increment after the explosion has been set to 1000 m/s. The yellow, blue and red dots respectively stand for the initial position of the Sun, the Earth and L5.

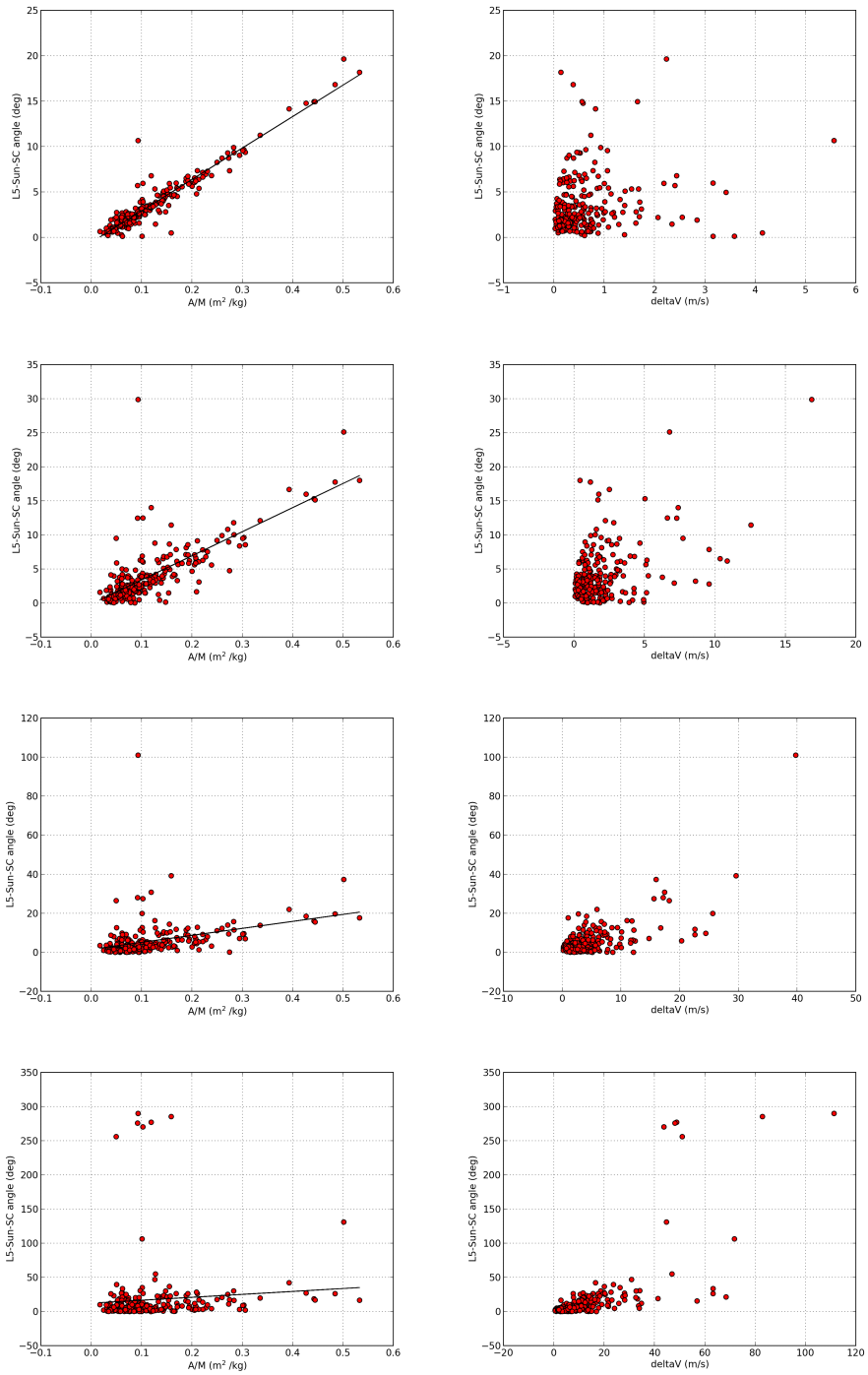

Figure 5.9: Maximum orbital phase as a function of the A/M ratio (left) and the delta-V boost obtained after the explosion (right) for different explosion magnitudes. The maximum velocity increment after the explosion has been set to 10 (top), 30 (second row), 70 (third row) and 200 (bottom) m/s.

C_r	**Explosion scenario (m/s)**	**Slope**	**Intercept**
0.5	10	10.63	-0.13
	30	10.54	0.72
	70	11.09	2.78
	200	9.083	14.81
1.0	10	22.41	-0.35
	30	22.61	0.24
	70	22.91	2.16
	200	22.03	13.97
2.0	10	47.65	-0.73
	30	48.81	-0.44
	70	49.73	1.06
	200	85.72	8.70

Table 5.2: Slope and intercept coefficients obtained through a linear fit of the scatter plot showing the debris maximum orbital phase as a function of their A/M ratio. The SRP coefficient is either set to 0.5, 1.0 or 2.0.

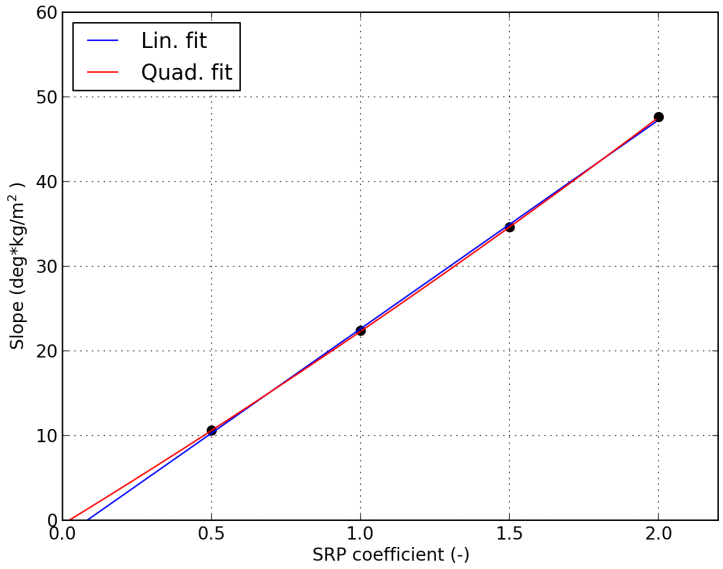

Figure 5.10: Slope of the linear fit as a function of the SRP coefficient for an explosion with a maximum ejection velocity of 10 m/s.

5.3.2 Break-up on the operational orbit

Now that the global behaviour of the debris has been drawn, we should investigate the effect of an on-orbit breakup. The aim of this subsection is to describe the impact of an initial velocity on the way the fragments are drifting. However, the energy added to the debris will be proportional to the size of the operational orbit. A complete quantitative study will require considering several orbits and assessing the corresponding effect for each of them. The present objective is rather to give a qualitative insight and we will only consider a 10^6 km amplitude orbit, inclined by 150° with respect to the ecliptic. As a reminder, the orbital velocity components in the plane of the ecliptic in the frame attached to L5 is given by:

$$\frac{\delta x'}{\delta t} = \frac{X_{sp}}{2}\left(1 - \frac{27\epsilon}{8}\right) n_3 \, cos\Big((1 - \frac{27\epsilon}{8})\, t + \phi_{sp}\Big) \tag{5.2}$$

$$\frac{\delta y'}{\delta t} = -\, X_{sp}\left(1 - \frac{27\epsilon}{8}\right) n_3 \, sin\Big((1 - \frac{27\epsilon}{8})\, t + \phi_{sp}\Big) \tag{5.3}$$

where $n_3 = 1.9909\,10^{-7}$ and $\epsilon = 3.0045\,10^{-6}$.

According to these expressions, the minimum and maximum velocity on a 10^6 km amplitude orbit are approximately equal to 100 and 200 m/s. The debris cloud will therefore be released with a velocity in between these two limits and with a particular direction. In this part we focus on the 4 extreme cases, namely the orbital phases where the velocity is minimum and those where it is maximum. The spacecraft explosion will therefore occur either on the semi-minor axis or on the semi-major axes of the elliptic operational orbit. This requires modifying the SNAPPshot Fortran code so that it takes the initial state of the breakup as an input rather than reading the state of L5 (or L4) from the relevant ephemeris file. Once again, we will consider three different maximum ejection velocities for the debris: 10, 100 or 1000 m/s. After the optimization of the operational orbit with MASW (from 21 June 2024 to 21 June 2034), we save the 10 year trajectory in a *.txt* file from which we can pick up any state. An important remark that has to be stressed concerns the planets that we include into the SNAPPshot propagator. In fact, SNAPPshot is able to read a state as an input but the latter has to be given in the International Celestial Reference System (ICRS[3]) which is centered on the Solar system barycenter (SSB). However, there does not exist any ephemeris file for the SSB and its position is directly computed from the planets included into SNAPPshot. We therefore need to include all planets to ensure that the SSB has the same definition as in MASW. We arbitrarily choose to place the explosion in the course of the sixth year, at an epoch that corresponds to one of the 4 extreme orbital phases (0°, 90°, 180° and 270°). Once the cloud has been generated, all debris are propagated for 250 years.

[3]The ICRS is the standard celestial reference system adopted by the International Astronomical Union. The axes of that system have been defined thanks the position of hundreds of distant extra-galactic radio sources, which makes them stationary with respect to our Solar system.

Figure 5.11 shows the cloud extent 50 years after the explosion at the 4 different orbital phases in the case of the 10 m/s event. In the same way, Figures 5.12 and 5.13 present the corresponding results respectively for a maximum delta-V boost of 100 and 1000 m/s. For these two cases, barely no changes in the debris distribution is seen after 50 years. Obviously, some debris can travel further away than what they were able to at L5 but the number of debris that enter into a horseshoe orbit is approximately constant for the 100 (0-1) and 1000 m/s (50-58) cases. On the other hand, the cloud extent for the 10 m/s explosion is more affected with a L5-Sun-Spacecraft angle that varies from 10.1 to 13.3 degrees. Table 5.3 gathers the angular extent of the cloud as a function of the orbital phase where the breakup takes place. It also shows the equivalent extent when the explosion occurs exactly at L5 at the dates corresponding to the four orbital phases. For such small ejection velocities, the variation in the debris spreading at L5 is induced by both the planetary configuration and the true anomaly of the Earth on its orbit, sometimes causing a slightly larger dispersion. The small differences (less than 1°) with an on-orbit breakup allows to conclude that the debris distribution would be barely the same whatever the initial position and velocity of the spacecraft around L5. Indeed, even if we take the larger orbit achievable ($1.6\,10^6$ km amplitude), the maximum velocity is only 1.6 times greater than for the above case; which will not change that much the results acquired in Table 5.3. In the same way, if we consider a more severe explosion case, the orbital velocity will have less influence in the debris spreading. All in all, the effect of an orbital breakup is noticeable only for low velocity explosions occurring on large operational orbits. This is again a confirmation that the major driver of the cloud dispersion is the solar radiation pressure.

Orbital phase of the boost (°)	**On-orbit breakup**	**L5 breakup**
0	10.1	10.1
90	10.6	11.6
180	13.3	12.8
270	11.8	12.3

Table 5.3: Comparison of the positive angular extent of the debris cloud for on-orbit and L5 breakups with a maximum velocity increment of 10 m/s. The explosion occurs either at a 0°, 90°, 180° or 270° or at the corresponding dates for L5.

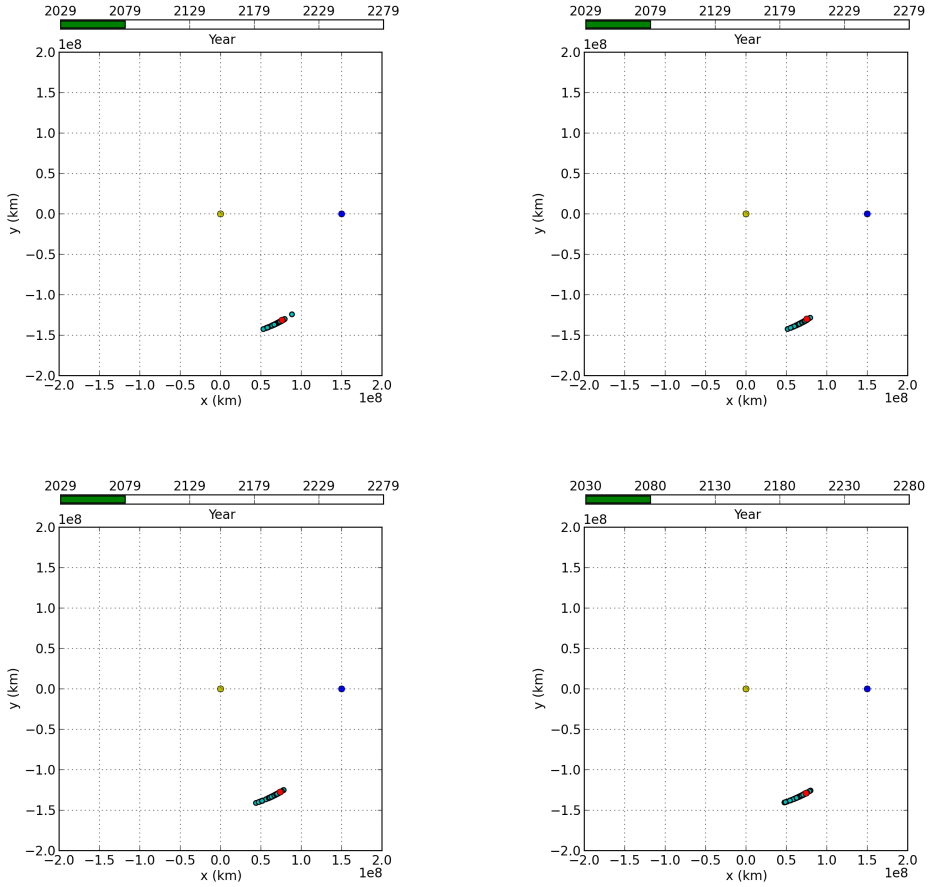

Figure 5.11: Debris distribution 50 years after a spacecraft explosion occurring exactly on a 10^6 km amplitude orbit. The explosion takes place either at a 0° (top left), 90° (top right), 180° (bottom left) or 270° (bottom right) orbital phase. The debris positions (cyan) are shown in the Earth's rotating frame. The maximum velocity increment after the explosion has been set to 10 m/s. The yellow, blue and red dots respectively stand for the initial position of the Sun, the Earth and L5.

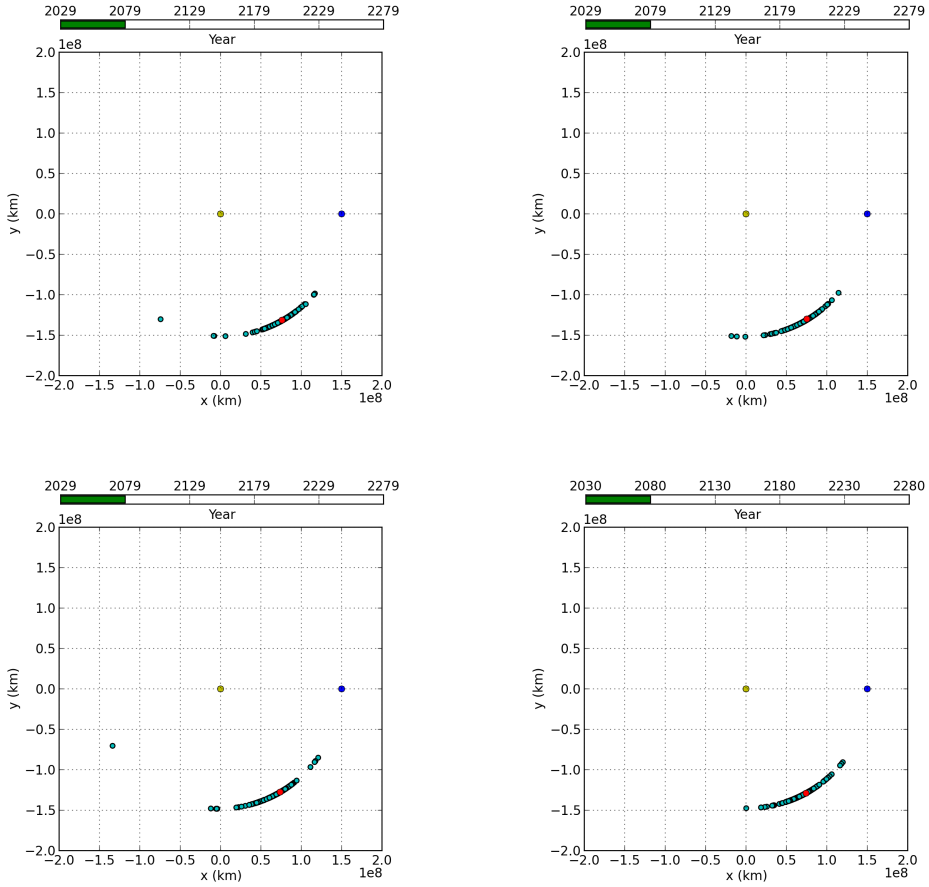

Figure 5.12: Debris distribution 50 years after a spacecraft explosion occurring exactly on a 10^6 km amplitude orbit. The explosion takes place either at a 0° (top left), 90° (top right), 180° (bottom left) or 270° (bottom right) orbital phase. The debris positions (cyan) are shown in the Earth's rotating frame. The maximum velocity increment after the explosion has been set to 100 m/s. The yellow, blue and red dots respectively stand for the initial position of the Sun, the Earth and L5.

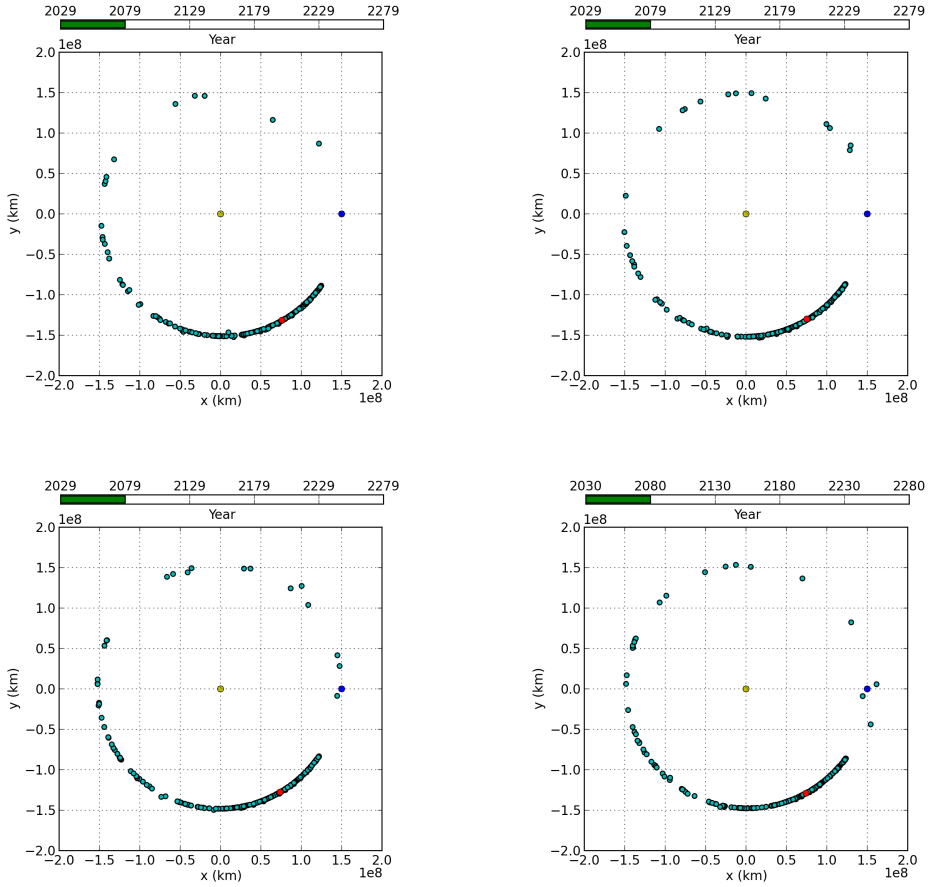

Figure 5.13: Debris distribution 50 years after a spacecraft explosion occurring exactly on a 10^6 km amplitude orbit. The explosion takes place either at a 0° (top left), 90° (top right), 180° (bottom left) or 270° (bottom right) orbital phase. The debris positions (cyan) are shown in the Earth's rotating frame. The maximum velocity increment after the explosion has been set to 1000 m/s. The yellow, blue and red dots respectively stand for the initial position of the Sun, the Earth and L5.

Chapter 6

Disposal orbit opportunities

Planetary protection is currently a hot topic in space exploration. Active efforts are made to develop capture and mitigation strategies as well as reusable launchers. However, in the case of interplanetary missions, graveyard orbits seem to be the best compromise to avoid polluting the other celestial bodies. In the same way, if another mission is designed to orbit around L5, we need to ensure a safe environment at least during its operational lifetime. This chapter is therefore devoted to the study of the different kinds of disposal orbits that we can achieve from L5 and the delta-V cost associated to them. We will also make use of the results from the previous chapter to figure out how we can use the solar radiation pressure to de-orbit a spacecraft from the triangular Lagrangian points.

The content of this chapter was produced with the previously mentioned ORBSW and MASW software. The disposal orbits are then drawn thanks to the results of Chapter 4, which established stable close operational orbits. Note that only positive tangential delta-V boosts, i.e. in the direction of the orbital velocity of the spacecraft, are considered.

6.1 Applying a delta-V manoeuvre

6.1.1 Verification of earlier results

In Chapter 3, we obtained an order of magnitude for the delta-V cost needed to reach a horseshoe orbit (about $40 - 50$ m/s) and to approach the Earth ($160 - 200$ m/s). We also found that there exist two orbital phases (90° and 270°) where the delta-V manoeuvre will be optimally used. The objective of this section is therefore to verify these conclusions and to bring some precision on the values acquired so far. In the same way as we did for the debris cloud in the previous chapter, we will measure the extent of the disposal orbit with the maximum L5-Sun-Spacecraft angles that is reached for a sufficiently long period of time. Note that the total extent of the orbit will not be symmetric with respect to L5 since tadpole orbits extend from the Earth to L3.

Considering only tangential delta-V boosts, Table 6.1 gathers the angular extent of some graveyard orbits achieved after applying a 20 m/s manoeuvre at different orbital phases. The propagation time has been set to 500 years to capture one full oscillation around L5. Once again, the *de435.bsp* ephemeris file is used. The disposal manoeuvre takes place in the course of the eleventh year once the operational phase has been completed (i.e after 21 June 2034). The two orbital phases related to the edges of the semi-minor axis still appear the best places to apply the de-orbiting manoeuvre. Even if we shift the operational phase by 3, 6 or 9 months, the values in Table 6.1 change by less than 2° in magnitude and the above conclusion still holds.

Orbital phase of the boost (°)	**Max. L5-Sun-Spacecraft angle (°)**
0	0.6
30	7.9
60	19.2
90	32.5
120	20.8
150	8.4
180	0.7
210	7.8
240	19.8
270	33.2
300	20.7
330	8.7

Table 6.1: Maximum L5-Sun-Spacecraft angle encountered over one full disposal orbit oscillation around L5. The magnitude of the delta-V manoeuvre has been set to 20 m/s.

Now, we will evaluate the delta-V cost to reach a horseshoe orbit and to come close to the Earth, applying the boost at a 270° orbital phase. Let us recall that the spacecraft enters into a horseshoe trajectory when it goes further than L3 and approaches the Earth from L4. We also consider the spacecraft to be close to the Earth when it crosses the Earth's motion as seen from the rotating frame (as a result of the eccentricity of the Earth's orbit). This happens when the two edges of the horseshoe orbits meet each other. After some investigations, we found that a tangential 43 m/s delta-V is enough to enter the horseshoe region. Figure 6.1 shows the resulting disposal orbit when a 42 m/s or a 43 m/s boost is applied. The propagation time has been set to 1000 years in order to catch at least one full oscillation around L5. In view of the time limitations encountered with the ephemeris file *de435.bsp*, we decided to use the longer *de431.bsp* available on the NASA's NAIF website. The latter allows to carry out very long propagation, from 2000 up to the year 17000 A.D.
On the other hand, the spacecraft crosses the Earth's motion for a velocity boost of 155 m/s,

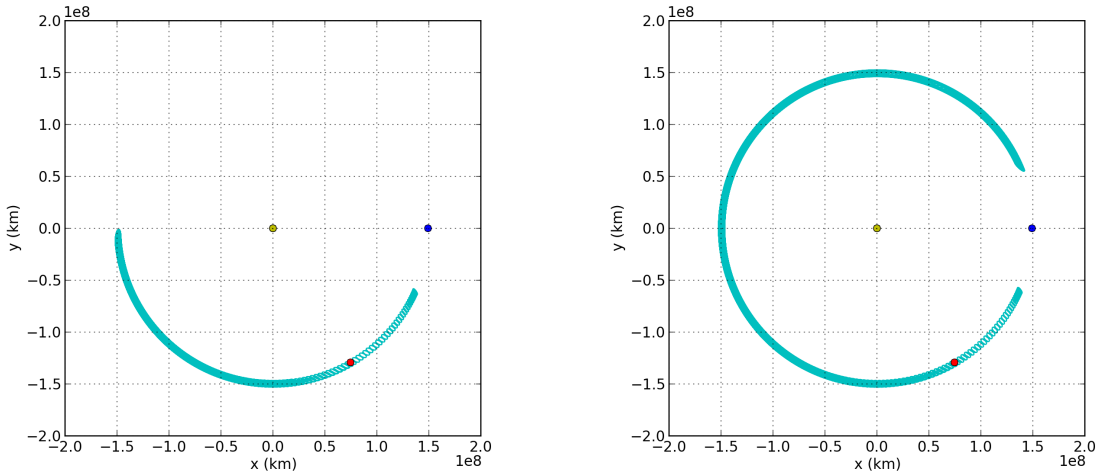

Figure 6.1: Disposal orbits acquired after a 42 m/s (left) or a 43 m/s (right) delta-V boost taking place at a 270° orbital phase. The propagation starts on 21 March 2035 and ends on 21 June 3034. The trajectories are shown in the Earth's rotating frame centred on the Sun. The yellow, blue and red dots respectively stand for the position of the Sun, the Earth and L5 at the epoch the manoeuvre is applied.

which is slightly less than what has been found in Chapter 3. The reasons could be the effect of the SRP as well as the eccentricity of the Earth's orbit (that were not included in the previous propagator) which act as destabilizing factors. Figure 6.2 displays the disposal orbits obtained with either a 154 or a 155 m/s boost. Beyond the latter limit, the spacecraft is no more on a horseshoe orbit but rather enters into an independent heliocentric orbit and can explore the whole Earth's path.

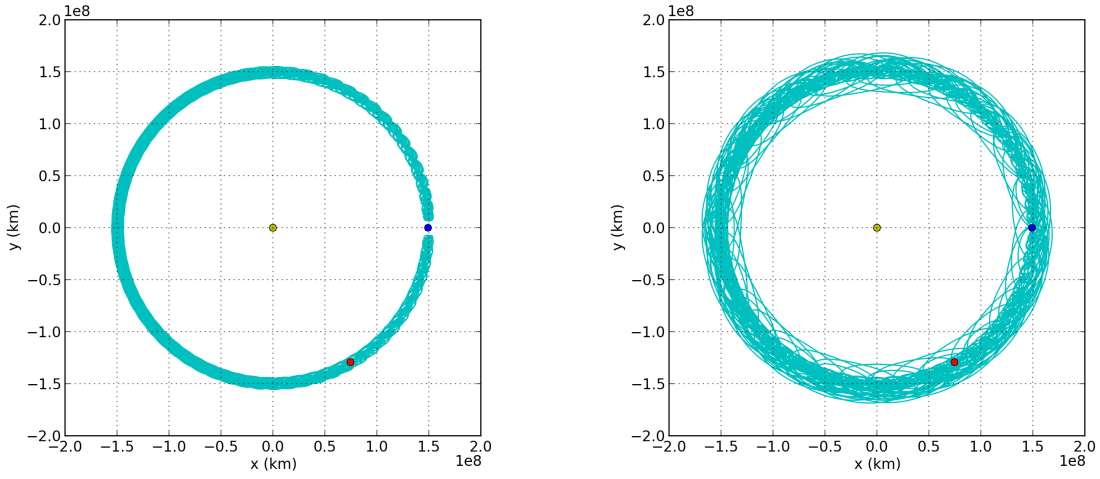

Figure 6.2: Disposal orbits acquired after a 154 m/s (left) or a 155 m/s (right) delta-V boost taking place at a 270° orbital phase. The propagation starts on 21 March 2035 and ends on 21 June 3034. The trajectories are shown in the Earth's rotating frame centred on the Sun. The yellow, blue and red dots respectively stand for the position of the Sun, the Earth and L5 at the epoch the manoeuvre is applied.

6.1.2 Characterization of tadpole and horseshoe orbits

As we have shown in the previous part, tadpole orbits are reachable with a delta-V manoeuvre up to 42 m/s. On the other hand, we can achieve a horseshoe orbit with a velocity boost ranging from 43 m/s to 155 m/s. The purpose of this section is to draw a relation between the delta-V burned and the angular extent (measured clockwise from L5) of these disposal orbits. This will be useful when evaluating the total delta-V requirements for a mission towards the triangular points. Let us thus take equally spaced values in the tadpole velocity range and retrieve the L5-Sun-Spacecraft angles that correspond to the maximum and minimum extent of the achieved graveyard orbit. Note that the manoeuvre still takes place at a 270° orbital phase and the initial state is then propagated for 1000 years to complete at least one full oscillation around L5.

Figure 6.3 shows the raw data obtained as well as both a quadratic and a cubic fit. None of the curves looks better than the other one in terms of catching the growth rate of the positive angular extent while both correctly reproduce the behavior of the negative side. For the positive edges, the relation seems linear for low delta-V boosts and then quickly grows towards 120° which refers to the position of L3. The angular extent, i.e. the allowed region, being related to the energy of the spacecraft, we expect a quadratic relation with its initial velocity. However, the expected relation seems to be slightly blurred since the satellite has already an orbital velocity. Note that whatever the date of the delta-V burn, the fundamental results still hold since the effect of the Earth's orbital eccentricity as well as the planetary configuration only cause a slight variation of the extent of the orbit. As a consequence, the delta-V limit to pass from tadpole to horseshoe orbits varies by less than 1 m/s while the boost needed to leave the horseshoe region lies in between 146 and 160 m/s.

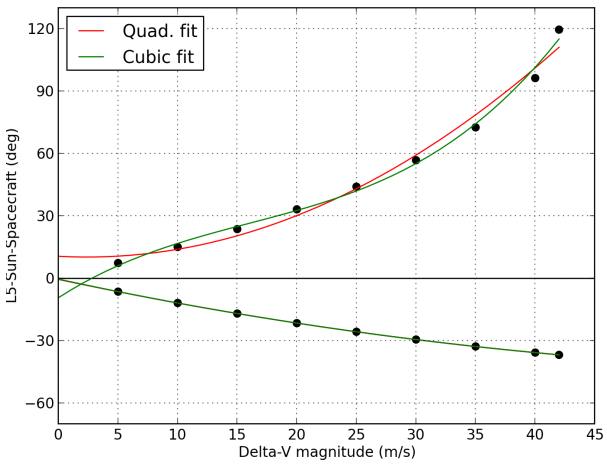

Figure 6.3: Extreme positive and negative angular extents of tadpole orbits (measured from L5) as a function of the delta-V magnitude needed to reach them.

The same relation can be drawn for horseshoe orbits. This is done in Figure 6.4. As expected, the allowed angular range is much more constrained than for tadpoles orbits and symmetric with respect to L3 (horizontal magenta line). Quadratic and cubic polynomials reproduce well both sides of the horseshoe orbit and the latter two seem to meet each other[1] when the delta-V is sufficiently high. At this point, the two edges merge and the spacecraft is free to move on an independent heliocentric orbit. Another remark concerns the negative side which seems to continuously decrease towards −60 degrees (the position of the Earth) when combining the results for delta-V manoeuvres for tadpole and horseshoe orbits. This behaviour is in contrast with that of the positive side which jumps from 120 to about 275 degrees. In fact, the spacecraft acquires sufficient energy to travel beyond L3 before it has explored the whole 60° region from L5 to the Earth.

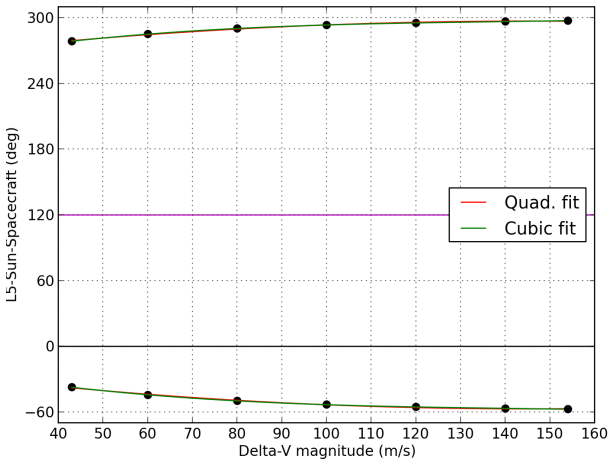

Figure 6.4: Extreme positive and negative angular extents of horseshoe orbits (measured from L5) as a function of the delta-V magnitude needed to reach them. The horizontal magenta line shows the angular position of L3 as seen from L5.

We can also show the evolution of the total extent of these orbits with respect to the delta-V manoeuvre applied. Figure 6.5 displays two very different behaviors. For tadpole orbits, the extent starts growing linearly before quickly increasing to finally reach L3 from the positive side. On the other hand, for horseshoe orbits the angular extent asymptotically approaches 360 degrees, i.e. a full circle.

6.1.3 Interference with future missions

It would be useful to determine the amount of time the spacecraft will spend in the operational region around L5 when the latter is on its final disposal orbit. We defined the operational region as a sphere of 2 million kilometre radius around L5. In view of the results obtained in Chapter 4, this covers the whole area where a satellite can be stabilized without the need

[1] Because the positive and negative angles are separated by 360 degrees

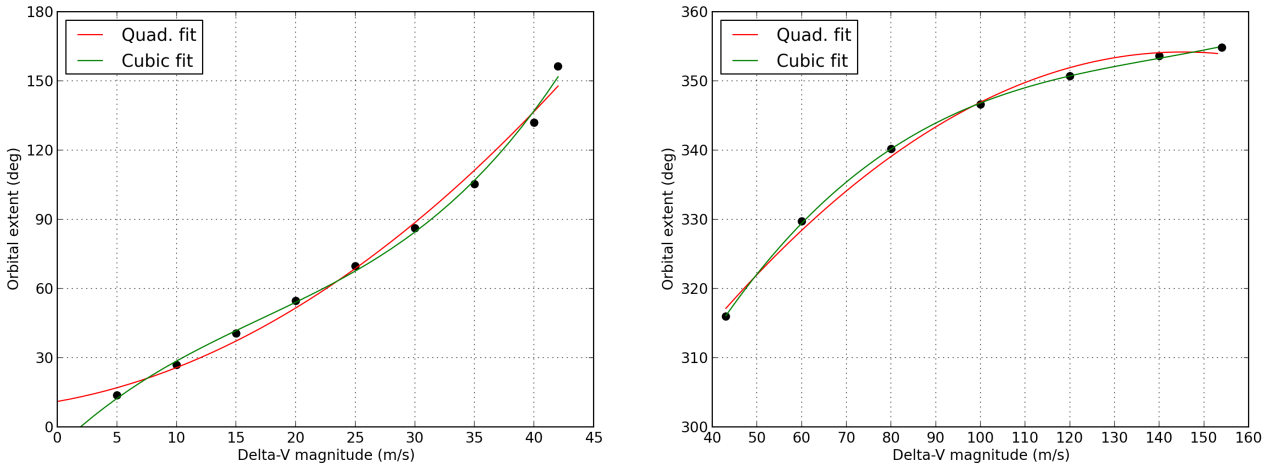

Figure 6.5: Total angular extent of tadpole (left) and horseshoe (right) orbits as a function of the delta-V magnitude needed to reach them.

for correction manoeuvres. This therefore represents an acceptable proximity indicator for the defunct spacecraft. The fraction of time spent in the operation sphere (OS), is then computed for each point in Figure 6.3 for tadpole orbits and in Figure 6.4 for horseshoe trajectories. However, we should assess this ratio for one complete oscillation around L5 in order to speak about a fraction of the orbital period, which would be more convenient. Because all tadpole and horseshoe orbits do not have the same oscillation period, we decide to evaluate the time spent in the operation zone for 5000 years. This should give a very good guess of the value for one period, mostly for tadpole trajectories. To speed up the computation time, we consider only Jupiter and Venus (in addition to the Sun and the Earth) in that long-term propagator. This is consistent with the results of chapters 2 and 3 since these are the main perturbing bodies at the triangular Lagrangian points. Figure 6.6 shows the obtained results for tadpole (left) and horseshoe (right) orbits.

There is no real trend in the data for the horseshoe class. This is certainly due to the 5000 year limit that has been fixed for the collision assessment. Indeed, for some horseshoe orbits, the spacecraft is susceptible to spend more time on one of the two sides, which causes a bias in the evaluation of the time spent in the operational region. However, that fraction is in any case less than 0.3%. For tadpole orbits, a sharp decreasing relation exists between the extent of the disposal orbit and the amount of time spent near L5. That was expected since the oscillation period is shorter for tadpole trajectories and the risk of a bias in the data is reduced. None of the fitted curves matches the exact behavior of the above graph but an exponentially decreasing trend is a good approximation. All in all, the fraction of time spent in the operational sphere is always lower than 8% for a disposal orbit with a total extent larger than 20 degrees.

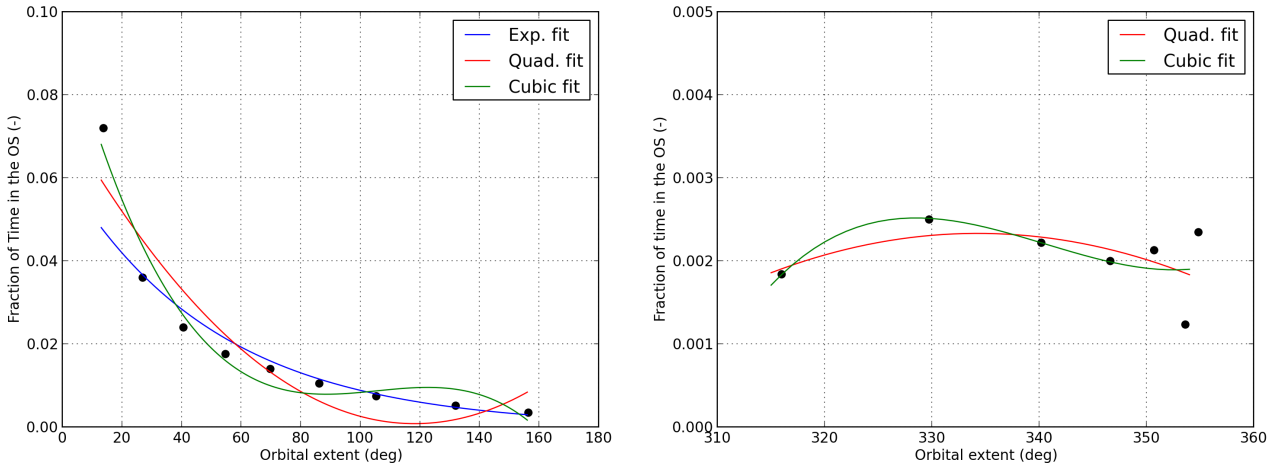

Figure 6.6: Fraction of the time spent in the operational region around L5 for different tadpole (left) and horseshoe (right) orbits. The propagation time has been set to 5000 years.

6.2 Using the solar radiation pressure

Another way to put the spacecraft on a graveyard orbit can be found thanks to the results of Chapter 5. Indeed, we have seen that the extent of the debris cloud is mainly driven by the solar radiation pressure. The fragments that get the higher area-to-mass ratio after the explosion show the larger oscillation motion around L5. The same behavior is therefore expected if the area of the spacecraft is suddenly increased at the end of the operational phase. A solar sail can thus be used as a fuelless way to de-orbit the satellite. The purpose of this section is to evaluate the angular extent of such disposal orbits for various sail surfaces and compare it to the amount of delta-V needed to achieve comparable results.

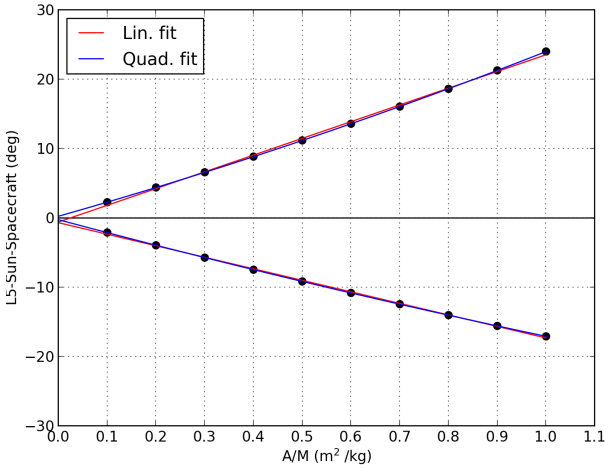

Figure 6.7: Extreme positive and negative angular extents of horseshoe orbits (measured from L5) as a function of the area-to-mass ratio.

Considering a 1000 kg spacecraft, a solar sail of 1000 m^2 gives a 40° extended tadpole orbit.

Alternatively, such disposal paths can be reached with a velocity boost of less than 15 m/s, which is rather low compared to the usual needs for disposal (see Table 3.3). The largest solar sail that has been designed so far was the NASA's *Sunjammer* sail with an area of more than 1200 m^2 (square sail with a 38 metres side). Unfortunately, the mission was cancelled few months before its launch due to a lack of confidence in contractor's ability to deliver the spacecraft in time (*Koebler J., 2014*). The 200 m^2 sail of IKAROS, a Japanese space mission, is therefore the largest sail that has been successfully deployed in space so far (*JAXA website*). With such a solar sail on board of a 1 ton satellite, we only achieve a 10° wide tadpole orbit, which is far from being suitable. Even if a solar sail is very lightweight (less than 2 kg for IKAROS), both the development costs and the small amplitude tadpole orbits that are achievable are major drawbacks in the use of such technology at the triangular Lagrangian points. Also, the deployment system needs to be designed in such a way that it will reliably operate after at least 10 years of spacecraft operations (to which is added the time of a transfer to L5). All in all, the use of thrusters seems more convenient since a very strong experience has been acquired with these devices for several decades of space exploration.

Chapter 7

Conclusion

In Chapter 2, preliminary analytic and numerical computations allowed us to assess the effect of the Solar system planets on the triangular Lagrangian points. We concluded that the gravitational environment around these points is mainly perturbed by Venus and Jupiter. Finally, the long-term impact of the other planets sets aside the possibility of finding new stable points apart from L5. Chapter 3 gave a qualitative understanding of the dynamics in the vicinity of the triangular points in a circular Sun-Earth system. A short and a long-period component combine to give an oscillating motion which is either called a horseshoe or a tadpole orbit depending whether the spacecraft goes beyond L3 or not. We have seen that some peculiar initial conditions, both in time and space, allow to find stable orbits around L5 for a limited amount of time. We overcome these constraints in Chapter 4 by designing and solving an optimization problem. Through this approach, we achieved orbits showing less than a 10% variation in semi-major axis (in a 10 year window) with an amplitude in the range $[6, 16]\,10^5$ km. Even though it is my own formulation of the problem, these limits appear more as the consequence of the complex dynamics that rules any motion in the vicinity of the triangular points. A more complete mission analysis should account for the transfer trajectory from the Earth to L5 as well as the insertion phase. However, given the state at the end of the transfer phase and sufficiently large bounds on the velocity change, there is no doubt that our optimization method can be used to find stable orbits in the previously defined range. Chapter 5 investigated the debris spreading in case of a fragmentation event occurring either at L5 or on-orbit around the latter. Minor differences have been found regarding the extent of the debris cloud, which is mainly driven by the solar radiation pressure. Indeed, even when the maximum ejection velocity approaches 1000 m/s, most of the debris (about 78%) stay in a tadpole orbit with a pendulum motion that is related to their area-to-mass ratio. However, as explained in section 5.2, we have fixed the number of size intervals to 9 in order not to generate and propagate too much debris. Even though a different proportion of fragments entering the horseshoe region would have been found with an increased number of debris constituting the cloud, the behaviour sketched in Chapter 5 will still hold. In Chapter 6, we finally studied the disposal opportunities for a decommissioned spacecraft that had been in orbit around L5.

Using a classical delta-V manoeuvre with a magnitude below 43 m/s allows to access the whole range of tadpole orbits while a velocity increment between 43 and $146 - 160$ m/s opens the horseshoe region. However, this holds for positive tangential delta-V manoeuvres. A future analysis could investigate whether there exists some non-tangential and/or negative boosts that would be cheaper in terms of delta-V costs. We have also evaluated the fraction of the time spent in a relative vicinity to L5 when the spacecraft is on its final disposal path. This fraction rapidly decreases for large tadpole orbits while staying lower than 0.3% for horseshoe orbits. We finally considered the deployment of a solar sail as a fuelless way to drive the spacecraft towards its final disposal orbit. Unfortunately, both the reliability requirements and the small amplitude tadpole orbits achievable are obstacles to the use of this technology in the vicinity of the triangular Lagrangian points. A further study could investigate and quantify the effect of using other disposal strategies like electric and magnetic sails that make use of the electrically charged particles of the solar wind (i.e. protons and electrons).

Bibliography

[1] POINCARE, H. (1890) *Sur le problème des trois corps et les équations de la dynamique*. Acta Mathematica, Vol. 13, p.1-270.

[2] LAGRANGE J.-L. (1772) *Essai sur le Problème des Trois Corps*. Prix de l'Académie Royale des Sciences de Paris, tome IX; reprinted in (1873) Oeuvres de Lagrange, Tome sixième (J.-A. Serret, ed.), pp. 229–331. Gauthiers-Villars, Paris.

[3] CONNORS, M. et al. (2011) *Earth's Trojan asteroid*. Nature. **475**, p.481-483.

[4] SLIZ-BALOGH, J. et al. (2018) *Celestial mechanics and polarization optics of the Kordylewski dust cloud in the Earth–Moon Lagrange point L5 – I. Three-dimensional celestial mechanical modelling of dust cloud formation*. Monthly Notices of the Royal Astronomical Society. **480**, p.5550-5559.

[5] ESA website. *Lagrange mission*. http://www.esa.int/Our_Activities/Space_Safety/Lagrange_mission2. Lastly consulted on 5 May 2019.

[6] THOLEN, D.J., Tejfel, V.G., & Cox, A.N. (2000) *Allen's astrophysical quantities*, 4th ed. Ed. A.N. Cox, p.293-313.

[7] FITZPATRICK, R. (2012) *An Introduction to Celestial Mechanics*. Cambridge University Press.

[8] VILLEMIN, G. *Points de Lagrange*. http://villemin.gerard.free.fr/Cosmogra/Lagrange.htm#point. Lastly consulted on 27 May 2019.

[9] DEPRIT, A. (1965) *Routh's Critical Mass Ratio at the Triangular Libration Centers*. AIAA Paper 65-681.

[10] RAUW, G. *Celestial Mechanics*. Faculty of Science. University of Liege. Academic year 2018-2019.

[11] RAND, R. H. (2012) *Lectures Notes on Nonlinear Vibrations*. Dept. Theoretical & Applied Mechanics. Cornell University.

[12] GOMEZ, G. et al. (2001) *Dynamics and Mission Design Near Libration Points Vol. IV Advanced Methods for Triangular Points* in World Scientific Monograph Series Mathematics - Vol. 5. World Scientific Publishing.

[13] BOBROV, O. A. (2014) *Modelling of Motion of Bodies Near Triangular Lagrangian Points*. Odessa Astronomical Publications, vol. 27/1.

[14] MIRIADE Ephemeris Generator. Portail Système Solaire, Observatoire Virtuel de L'IMCCE. Observatoire de Paris / CNRS. Available on http://vo.imcce.fr/webservices/miriade/?forms. Lastly consulted on 29 April 2019.

[15] MARZARI, F. et al. (2002) *Origin and Evolution of Trojan Asteroids*. Asteroids III, W. F. Bottke Jr., A. Cellino, P. Paolicchi, and R. P. Binzel (eds), University of Arizona Press, Tucson, p.725-738.

[16] MURRAY, C. D. and DERMOTT, Stanley F. (1999) *Solar System Dynamics*. Cambridge University Press, p.95-96.

[17] JANOVSKY, R. et al. (2002) *End-of-Life De-orbiting Strategies for Satellites*. Deutscher Luft- und Raumfahrtkongress. DGLR-JT2002-028.

[18] COLOMBO, C. et al. (2013) *End-of-Life Disposal Concepts for Libration Point and Highly Elliptical Orbit Missions*. In: 64th International Astronautical Congress. Strathprints.

[19] ESA, Herschel documentation. *Routine Operations and Post-Operations mission phases* http://herschel.esac.esa.int/Docs/Herschel/html/ch01s02.html. Lastly consulted on 24 April 2019.

[20] ARMELLIN, R. et al. (2014) *Disposal Strategies for Spacecraft in Lagrangian Point Orbits*. In 24th AAS/AIAA Space Flight Mechanics Meeting.

[21] BALINT, S. (2014) *Communicating with a deep space probe using Software Defined Radio: The ISEE-3 Reboot Project*. Ettus Research.

[22] NASA, *ISEE-3 Reboot Project*. Solar System Exploration Research, Virtual Institute. https://sservi.nasa.gov/articles/isee-3-reboot-project/. Lastly consulted on 4 Mai 2019.

[23] NAIF, Jet Propulsion Laboratory. California Institute of Technology. https://naif.jpl.nasa.gov/pub/naif/generic_kernels/. Lastly consulted on 29 April 2019.

[24] MONTENBRUCK, O. and GILL, E. (2000) *Satellite Orbits: Models, Methods, and Applications*. Physics and Astronomy Online Library. Springer Verlag. p.77-83.

[25] DELGADO, M. R. (2008) *Radiation Pressure: Modelling the Space Environment*. European Masters in Aeronautics and Space. E.T.S.I Aeronáuticos, Universidad Politécnica de Madrid.

[26] ESPENAK, F. (2016) *Earth at Perihelion and Aphelion: 2001 to 2100*. AstroPixels.com. http://www.astropixels.com/ephemeris/perap2001.html. Lastly consulted on 30 April 2019.

[27] ROBERTS, J. and KOCHENDERFER, M. (2014) *Introduction to Mathematical Optimization*. Standford University. Mathematical Optimization course.

[28] LEYFFER, S. and MAHAJAN, A. (2010) *Nonlinear Constrained Optimization: Methods and Software*. Argonne National Laboratory, Mathematics and Computer Science Division. Preprint ANL/MCS-P1729-0310.

[29] WOMERSLEY, R. (2008) *Local and Global Optimization: Formulation, Methods and Applications*. School of Mathematics & Statistics, University of New South Wales.

[30] PAGMO & PYGMO documentation, *List of algorithms (UDAs) available in pagmo/pygmo*. https://esa.github.io/pagmo2/docs/algorithm_list.html. Lastly consulted on 3 Mai 2019.

[31] ZELENSKY, N. et al. (2011) *Improvements To Solar Radiation Pressure Modelling for Jason-2*. American Geophysical Union Fall 2011 Meeting, San Francisco.

[32] GOBINDDASS, M.-L. and WILLIS, P. (2008) *Estimating daily Solar Radiation Pressure coefficients*. IDS meeting, Paris.

[33] POWELL, M.J. (1994) *A Direct Search Optimization Method That Models the Objective and Constraint Functions by Linear Interpolation*. In: Gomez, S. and Hennart, J.-P., Eds., Advances in Optimization and Numerical Analysis: Mathematics and Its Applications, Springer Netherlands, p.51-67.

[34] BURKARDT, J. (2012) *The Compass Search Optimization Algorithm*. Department of Scientific Computing, Florida State University. https://people.sc.fsu.edu/~jburkardt/c_src/compass_search/compass_search.html. Lastly consulted on 18 May 2019.

[35] SVANBERG, K. (1998) *The Method of Moving Asymptotes - Modelling aspects and solution schemes*. Lectures notes for the course: Advanced Topics in Structural Optimization, Danish Center for Applied Mathematics and Mechanics.

[36] SVANBERG, K. (2002) *A class of globally convergent optimization methods based on conservative convex separable approximations*. SIAM J. Optim. 12 (2), p.555-573.

[37] KERSCHEN, G. *Astrodynamics*, Space Structures & Systems Lab (S3L), University of Liege, Academic year 2018-2019.

[38] KESSLER, D. J. and COUR-PALAIS, B. G. (1978) *Collision Frequency of Artificial Satellites: The Creation of a Debris Belt*. Journal of Geophysical Research, Vol. 81, No. A6, p.2637-2646.

[39] EMSPAK, J. (2016) *How can humans clean up our space junk?*. The Verge, https://www.theverge.com/2016/12/30/14116918/space-junk-debris-cleanup-missions-esa-astroscale-removedebris. Lastly consulted on 8 May 2019.

[40] GOUGH, E. (2018) *A New Solution to the Space Junk Problem. Spacecraft with Plasma Beams to Force Space Junk to Burn Up*. Universe Today, Space and astronomy news. https://www.universetoday.com/140120/a-new-solution-to-the-space-junk-problem-spacecraft-with-plasma-beams-to-force-space-junk-to-burn-up. Lastly consulted on 9 May 2019.

[41] SURREY SPACE CENTRE. *CubeSail*. University of Surrey, United Kingdom (2017). https://www.surrey.ac.uk/surrey-space-centre/missions/cubesail. Lastly consulted on 8 May 2019.

[42] JOHNSON, N. L. et al. (2001) *NASA's New Breakup model of EVOLVE 4.0*. Elsevier Science Ltd on behalf of COSPAR. Advances in Space Research Vol. 28, No. 9, p.1377-1384.

[43] LETIZIA, F. (2016) *Space Debris cloud evolution in Low Earth Orbit*. University of Southampton, Faculty of Engineering and the Environment, PhD Thesis, p.210-211.

[44] KRISKO, P. (2011) *Proper Implementation of the 1998 NASA Breakup Model*. National Aeronautics and Space Administration. Orbital Debris Quarterly News, Vol. 15, Issue 4, p.4-5.

[45] KOEBLER, J. (2014) *A Brief, Depressing History of Solar Sails*. Motherboard, Tech by Vice. https://www.vice.com/en_us/article/wnjp4q/a-brief-depressing-history-of-solar-sails. Lastly consulted on 23 May 2019.

[46] JAXA, *IKAROS mission overview*. Japan Aerospace Exploration Agency. https://global.jaxa.jp/countdown/f17/overview/ikaros_e.html. Lastly consulted on 23 May 2019.